High-Quality Lead-Free Double Perovskite Single Crystals and their Optical Properties

Dissertation zur Erlangung des
naturwissenschaftlichen Doktorgrades
der Julius-Maximilians-Universität Würzburg

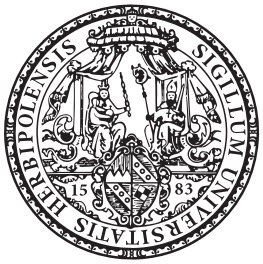

vorgelegt von
Melina Brigitte Melanie Armer
aus Würzburg

Würzburg, 2022

This document is licensed under the Creative Commons Attribution 4.0 International License (CC BY 4.0):
http://creativecommons.org/licenses/by/4.0 This CC license does not apply to third party material (attributed to another source) in this publication.

Eingereicht am
bei der Fakultät für Physik und Astronomie

1. Gutachter: Prof. Dr. Vladimir Dyakonov
2. Gutachter: Prof. Dr. Thomas Bein
3. Gutachter:
der Dissertation

Vorsitzende(r):
1. Prüfer: Prof. Dr. Vladimir Dyakonov
2. Prüfer: Prof. Dr. Thomas Bein
3. Prüfer:
im Promotionskolloquium.

Tag des Promotionskolloquiums:

Doktorurkunde ausgehändigt am:

Contents

1 Introduction

> Ein beschleunigter "Ausbau der eneuerbaren Energien und Reduktion des Energieverbrauchs [ist entscheidend] für unsere Unabhängigkeit. Klimaschutz bedeutet Freiheit und das ist heute in dieser schwierigen Lage wichtiger denn je." - Dr. Robert Habeck, Federal Minister for Economic Affairs and Climate Action of Germany

During the past decades the cost of electricity has increased tremendously in Germany as shown in Figure 1.1. In 2022, the situation worsened due to the war in Ukraine and the following shortage of fossil fuels worldwide.[1] Additionally, fossil fuels are a limited resource. Nevertheless, 59 % percent of Germany's energy consumption is produced by fossil fuels.[2] The combination of climate change and the dependence on only a few countries, which are able to deliver oil and gas, makes renewable energies an important tool to increase sustainability, battle climate change and to become more independent of other countries. Solar energy deserves special attention, as the energy, which the sun supplies us with every day, cannot only be used for electricity but for heating as well. However, photovoltaics still only produced 20.1 % of Germany's electricity and 4.2 % of heat in 2021.[3] Furthermore, the German government has increased funding for research on photovoltaics from roughly 68 million € to 86 million € in 2019, emphasizing the increasing importance of solar energy conversion.[4] Although silicon photovoltaics are rather efficient and can nowadays be seen on many houses, the intrinsic properties of silicon still leave room for improvement.[5] As an example, silicon is an indirect semiconductor, which generally is disadvantageous for the application in solar cells.[6] Furthermore, silicon possesses rather low absorption coefficients, which makes it necessary to fabricate solar cells with thick active layers, hence increasing the material consumption significantly.[8], [9] Consequently, photovoltaic research also focusses on finding new cheap and efficient absorber materials, such as lead-halide perovskites, which can compete with silicon.[10]–[12] Lead-halide perovskites have already reached high efficiencies of 25.7 % in single junction devices and 31.3 % in silicon-perovskites tandem devices.[13], [14] Hence, perovskite solar cells are already reaching similar efficiencies as commercial silicon devices.[13], [14]
However, due to the lead contained in lead-halide perovskite solar cells, research is try-

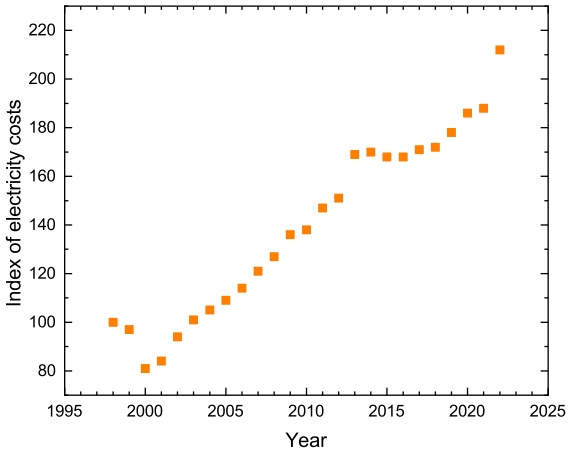

Figure 1.1: Evolution of the Electricity Index in Germany showing the strong increase in prices of electricity. Adapted from [7]

ing to simultaneously find non-toxic, stable and lead-free materials for the application in photovoltaic devices.[12], [13], [15]–[17] In order to do this, new materials are often synthesized as crystals at first, in order to study their crystal structure and their physical properties.[17]–[21]

In fact, crystal growth has been widely used throughout history. The crystallization of sea salt can be considered one of the oldest techniques of crystal growth, dating back even to prehistoric times.[22] Even processes such as recrystallization, sublimation and distillation date back to the 12th or 13th century.[22] However, Homer first used the word "crystallos" in order to describe ice crystals and later the word crystallization was used in the 17th century for the first time.[22] In 1611, Kepler proposed the principle of the crystallographic form and structure in his article "Six-cornered Snowflake".[23] Later on, in 1666, Boyle observed that crystals grown from solution strongly depend on impurities and growth rates, although the physics behind the crystal growth still remained mystified.[22] Lowitz later confirmed that the requirement for crystal growth from solution is supersaturation and found that supersaturation can either be reached by evaporation or supercooling.[22] In the late 19th and early 20th century significant contributions to the understanding of crystal structures were made by Bravais, Gibbs and Laue. [22] Their findings of the 14 lattice types, the derivation of the equilibrium form of a crystal as well as the possibility to determine crystal structures enabled progress in the understanding of crystal growth.[22] Further development of crystal growth techniques occurred in the 20th century, starting with the first growth from solution in a rotating vessel in 1895, the development of hydrothermal growth by Spezia, as well as growth techniques from melts, developed by Czochralski in 1916 and Bridgman in 1923.[22], [24], [25] During the second world war, the development of crystal growth technology was boosted due to the high demand for crystals for electronics

and optical applications. Especially the Czochralski method, zone melting developed by Pfann as well as the floating zone technique, used for pure silicon crystals, were established in order to grow high-quality and pure single crystals.[22] Additionally, the breakthrough in the crystallization of diamond, published in 1955, was a milestone in the field of crystal growth.[22] In summary, crystal growth has a long history and, over time, contributed significantly to our understanding of material properties. It also is still significant to the technologies we are using in our everyday life.

This thesis will contribute to the topic of crystal growth as well as emergent photovoltaic materials by the fabrication of lead-free double perovskite single crystals. Additionally, the impact of crystallization and stoichiometry on the optical and physical properties of lead-free double perovskite materials will be investigated. The **second chapter** of this thesis will give an introduction into the field of perovskites including the challenges of commercialization of lead-halide perovskites and the promising characteristics of lead-free double perovskites.

As high-quality crystals are subject of the studies in this thesis, the **third chapter** will introduce the theory of crystal growth as well as the different crystal growth techniques and characterization methods to analyze crystal quality.

The optical characterization of crystals can be used in order to investigate changes in crystal quality and studying the optical properties of a material. Hence, the **fourth chapter** will describe the tools of photoluminescence spectroscopy. Additionally, the concept of absorption, absorption coefficient and its measurement by transmission as well as PLE are introduced in order to characterize tailstates in a perovskite.

Having set the fundamental theory and experimental methods the chapters five and six will introduce the main experimental results. In **chapter five**, the impact of crystallization and precursor stoichiometry on the physical properties of $Cs_2AgBiBr_6$ is presented, while **chapter six** will introduce $Cs_2NaFeCl_6$ as a new lead-free double perovskite. $Cs_2NaFeCl_6$ is more earth abundant than $Cs_2AgBiBr_6$ and shows promising physical properties for the application in magnetic and low temperature devices or space applications.

2 Chances and challenges of perovskite materials

Organo lead-trihalide perovskite solar cells have first been reported in 2009 with a power conversion efficiency (PCE) of about 3.8 %.[26] Meanwhile, they have reached efficiencies of more than 25 % [14] and are regarded as a potential alternative to silicon solar cells. Therefore, the following chapter will introduce the material class of lead-halide perovskites and discuss its commercialization potential. Since the toxicity of lead is widely discussed in the community, lead-free perovskites are introduced as alternative materials for lead-halide based systems. As the focus of the presented thesis are double perovskites, cesium silver bismuth bromide ($Cs_2AgBiBr_6$) is introduced first as one of the most promising double perovskite materials to date.

2.1 Commercialization of lead-halide perovskite solar cells

The ABX_3 perovskite structure dates back to the discovery of calcium titanate $CaTiO_3$ in 1839 by Gustav Rose, who named this material after the russian mineralogist Lev Perovski.[10], [27] Since then, all materials with an identical crystal structure are referred to as perovskites.[10]
Lead-halide perovskites adapt this crystal structure by combining large A-cations like methylammonium (MA^+), formamidinium (FA^+) or cesium (Cs^+) with a lead ion (Pb^{2+}) as B-cation and an halogen anion such as chloride (Cl^-), bromide (Br^-) or iodide (I^-) at the X position.[10] An exemplary perovskite crystal structure is shown in Figure 2.1.

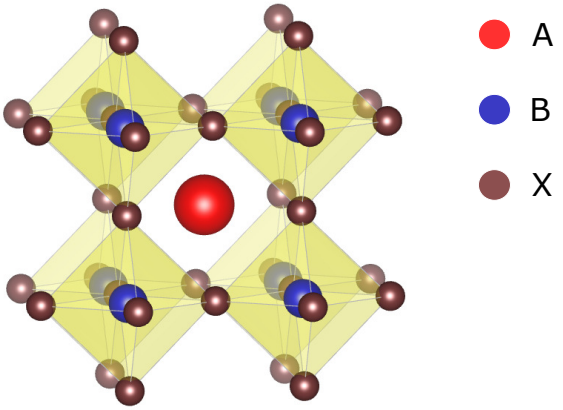

Figure 2.1: Typical ABX_3 crystal structure. The A site is usually occupied by large cations like MA^+, FA^+ or Cs^+ while Pb^{2+} is used as the B-site cation followed by the most common anions Cl^-, Br^- or I^- at the X position.

By combining A, B, and X ions, lead-halide perovskites have shown great tuneability in their optoelectronic properties.[28]–[30] Moreover, by varying the halogen ions from Cl^- or Br^- to I^-, it is possible to adjust the bandgap E_g of lead-halide perovskites. Using only Cl^- as anion, a bandgap of 3.11 eV could be realized, while in contrary employing only the Br^- anion the bandgap decreases to 2.35 eV.[28], [29] However, for Methylammoniumleadtriiodide ($MAPbI_3$), an even lower bandgap of 1.6 eV was obtained.[28], [29]

In addition to the controllable bandgap, lead-halide perovskites have shown exceptional optoelectronic properties, such as small direct bandgaps[6], small exciton binding energies[31], long charge-carrier diffusion lengths [32]–[34], low nonradiative charge carrier recombination rates [35] as well as high charge carrier mobilities [36]–[38]. Although those materials are low cost[6], [39], easily processable [39], [40] and reach efficiencies as high as 25.7 % [41], lead-halide perovskites still suffer from poor stability to this day.[42], [43] Furthermore, the employment of lead iodide as a precursor for lead-based perovskites has raised concerns due to the toxicity of lead, especially when thinking about making lead-halide perovskites commercially available.[6], [44] The toxicity of lead and the good solubility of lead iodide (PbI_2) in water poses potential health risks which have to be evaluated.[45], [46] Not only is PbI_2 used as a precursor salt, but it is also a byproduct of the decomposition process observed in perovskite solar cells. Therefore, lead poses a threat to human health if the decomposition products are not contained properly within the solar module.[26] Flora et al. showed that up to now no safe level of lead exposure could be found.[47] This makes the risks of lead exposure to humans a factor which is often discussed in the perovskite community. The exposure to lead can have serious effects on the human health as it impacts not only

the nervous system but also the hematopoietic, renal as well as the reproductive system.[47]
However, lead and especially the water soluble PbI_2 poses risks for humans as well as for the environment. An investigation studying the biological impact of lead found that lead from halide perovskites is significantly more bioavailable than the already existing lead contamination in the ground.[48] In their study, Li et al. used chili, mint and cabbage plants in order to investigate the accumulation of lead in the plants. During the study, exceptionally high amounts of lead were found in all plants up to the point where lead intoxication was visible.
Due to the above mentioned risks of lead on human health and the environment the European Union has safety values in place which restrict the use of lead. In electronic devices the lead content is limited to 0.1 wt%.[49] However, lots of exceptions were made for the lead use in devices including photovoltaics.[49] Nevertheless, the need for stable and less toxic or even lead-free alternatives for perovskite photovoltaics has increased efforts to find new perovskite materials.

2.2 Lead-free perovskites

In order to find new perovskites and therefore offer one solution to the toxicity issue of their lead halide counterparts, several possible material combinations have been investigated in literature. However, when thinking about lead-free crystal structures, possibilities are greater and not limited to the typical ABX_3 perovskite crystal structure. Furthermore, it was described in literature that the promising properties of lead-halide perovskites can be assigned to the $6s^2$ lone pair electron of lead.[6], [50] This lone pair configuration in lead-halide based perovskites is responsible for the large dielectric constant, small effective masses as well as their promising defect tolerance.[51] Interestingly, the high defect tolerance is also assigned to the orbitals contributing to the valence and conduction bands. For $MAPbI_3$, the conduction band minimum (CBM) is mostly made up of bonding orbitals, whereas the valence band maximum (VBM) emerges from antibonding orbitals.[50], [51] This is different to more conventional semiconductors, where the conduction band is usually composed of antibonding orbitals and only the valence band emerges from bonding states.[51] Interestingly, such lone pair configurations can also be found in other compounds containing tin (Sn^{2+}), germanium (Ge^{2+}), antimony (Sb^{2+}) as well as bismuth (Bi^{2+}).[6] Those materials are all less toxic than lead and therefore attractive for the application in perovskite photovoltaics.[6].
In the following sections, the requirements for the physical properties of lead-free per-

ovskites, to be successfully used in solar cells, will be discussed. Furthermore, the tolerance factor as a tool to screen for suitable material compositions is introduced. Finally, more focus will be put on Bi-based materials and $Cs_2AgBiBr_6$ as a promising double perovskite in particular.

2.2.1 Material requirements for lead-free absorber materials

Before going into more detail about different possible perovskite compositions, the required physical properties of a solar absorber are discussed. Firstly, when designing solar cell absorber materials, carefully choosing the bandgap of the material is necessary. For this, the Shockley-Queisser limit is a parameter, which defines the best bandgap for working devices.[52] Shockley and Queisser assumed that radiative electron-hole recombination is the only efficiency-limiting factor of a device.[52] As a consequence, Shockley calculated the maximum possible efficiency of a device and found that the highest efficiencies can be reached if an absorber material with a bandgap close to 1.3 eV is used.[6]

The bandgap is not the only decisive parameter. One also has to take the absorption properties of a semiconductor into account. In order to create a large number of free charge carriers, the absorber material of a solar cell should exhibit large absorption coefficients and a steep absorption edge.[6] In consequence, direct bandgap semiconductors are preferable for the development of thin absorber layers in photovoltaic devices.[6]

To effectively create current in a solar cell, the charge carriers in the device must be able to reach the extraction layers. Therefore, a sufficiently high mobility μ of the electrons and holes is required. However, the charge carrier mobility is a parameter which is determined by the curvature of the bands, as the effective mass m^*, which is described by the band dispersion, is proportional to $\frac{1}{\mu}$. Thus, small effective masses of the charge carriers are needed in order to guarantee high charge carrier mobilities in a semiconductor.[6]

In addition to the mobility, charge carrier recombination is also essential in the characterization of photovoltaic devices. The diffusion length of charge carriers L_D, given by

$$L_D = \sqrt{\frac{k_b T}{e} \cdot \mu\tau} \tag{2.1}$$

is not only limited by the mobility but also by the charge carrier lifetime. As a consequence, limited nonradiative recombination losses combined with high minority carrier lifetimes have shown to be advantageous for perovskite solar cells.[6], [36]

Moreover, lead-halide perovskites have shown that high defect tolerance is another

crucial parameter for their application in devices. Having a high defect tolerance means that although a perovskite shows a large number of grain boundaries and point defects in a thin film, they are still very well performing in solar cell devices. The so called defect tolerance stems from the antibonding interactions in the valence band, and therefore mostly shallow traps are present in perovskite materials.[53]
At last, whenever a perovskite is used as absorber layer, additional thought has to be put into the correct alignment of the perovskite film with the transport layer on top and beneath the perovskite. A good energetic alignment ensures that no further voltage losses will be caused in the device. Furthermore, to be able to use standard transport layers, it is advantageous for the energy levels of the chosen perovskite to match well with the conventionally used transport materials such as TiO_2, P3HT as well as Spiro-OMeTAD.[6]

2.2.2 The tolerance factor

When designing new perovskite materials, the physical properties are not easily tuneable as it is not possible to just combine atoms from the periodic table which should in theory lead to the desired properties. This is due to the fact, that the size of the ions which will later define the crystal structure of the materials, have to match in order to be incorporated into a crystal lattice. One parameter which can predict whether a combination of ions will form a stable perovskite structure and also give information about whether a cubic, orthorhombic or tetragonal crystal structure will be formed, is the tolerance factor t, which will be introduced in this section.
The tolerance factor was initially proposed by Goldschmidt in 1926 with the motivation to establish a general rule for correlating the shape of a crystal and its chemical composition.[54] Consequently, when looking for new lead-free perovskites, calculating the tolerance factor can help to predict whether the desired compound will form a stable crystal structure or not, depending on the mismatch of the ionic radii r_A, r_B and r_X of the atoms.[55] For calculating the tolerance factor given by

$$t = \frac{r_A + r_X}{\sqrt{2}\,(r_B + r_X)} \tag{2.2}$$

one needs to know the ionic radii of the desired atoms at the A, B, and X position of the perovskite structure.[54] If the resulting tolerance factor of the desired perovskite composition yields a value of $t = 0.9 - 1$, a cubic perovskite crystal structure can be predicted. However, if the tolerance factor lies between 0.7 and 0.9, the chosen A cation is slightly too small. Hence, the crystal structure will either be orthorhombic, rhombohedral or tetragonal when the perovskite is formed.[56] For large A cations, toler-

ance factors $t > 1$ can be found. This means that no 3D perovskite structure will be stable. Instead, layered perovskite crystal structures might be formed ending up with stoichiometries like Ruddlesden-Popper or Dion-Jacobson compositions.[56]
Although the tolerance factor alone is surely not the best method to predict new perovskite compositions, as it ignores effects of different electronegativity and therefore the character of the bonds between the ions[56], it is an easy way to hint towards stable or nonstable perovskite structures in a first step.

2.2.3 Lead-free perovskites with ABX_3 crystal structure

After presenting the tolerance factor as a parameter, which can be used to asses the potential of different perovskite compositions, this section will introduce several lead-free perovskites which are crystallizing in the typical ABX_3 crystal structure. Moreover, the advantages and disadvantages of those compositions with respect to their B cations, will be discussed.
One interesting material to substitute Pb with is Sn. Sn-based perovskites have attracted interest as they are non-toxic, cheap and exhibit very similar electronic properties as their lead counterparts. Additionally, they have already reached certified solar cell efficiencies of up to 14.03 % in 2021 by using $FASnI_3$ and passivating it with a $FPEA^+$ 2D capping layer.[57] However, as the Sn^{2+} ion is prone to oxidize to Sn^{4+}, suppressing the fast oxidation of Sn still remains a major challenge in order to fabricate stable devices.[6], [58]
Other lead-free absorber materials are based on Ge which can also crystallize in the ABX_3 crystal structure. However, Ge readily oxidizes to Ge^{4+}, which is caused by the low binding energy of the $4s^2$ electrons and therefore presents the major issue of Ge-based solar cells.[6] Additionally, the efficiencies of pure Ge based devices are still low compared to Sn-based devices as they have only reached efficiencies below 5 % up to 2020.[59]
As the search for lead-free perovskites is ongoing, Sb-based perovskites have shown to be of interest for device applications. As Sb is a material also used in therapeutics, the application in perovskite photovoltaics does not carry risks related to the toxicity of the material.[6] Furthermore, Sb is known for a strong lone pair effect which predicts good optoelectronic properties for the material.[6] However, Sb-based lead-free perovskites usually do not crystallize in the typical ABX_3 crystal structure but rather form a $A_3B_2X_9$ stoichiometry, also referred to as layered perovskite.[60], [61]. Accordingly, those defect perovskites usually form either a 0D or 2D structure depending on the orientation of the octahedras in the crystal lattice. In turn, such materials usually exhibit bandgaps larger than 2 eV.[62]

In addition to Sb, Bi can also crystallize in the defect perovskite crystal structure and can therefore be used as the B cation in such perovskites. Yet, Bi-based defect perovskites suffer from similar issues as their Sb-based counterparts, such as relatively wide bandgaps, high exciton binding energies which limit the generation of free charge carriers as well as low mobilities and overall poor charge transport.[63]
As a result of limited lead-free perovskites crystallizing in the typical perovskite structure, lead-free double perovskites have attracted great interest over the past years.[6], [17], [64], [65] The following section will introduce the double perovskite crystal structure as well as the yet most promising lead-free double perovskite $Cs_2AgBiBr_6$.

2.3 $Cs_2AgBiBr_6$, a promising lead-free double perovskite

While searching for different lead-free perovskites, the double perovskite structure, also known as elpasolite, has become of interest.[66] The double perovskite crystal structure is using two B cations leading to a $A_2BB'X_6$ stoichiometry.[6] For that, monovalent and trivalent B cations are located at alternate positions in the unit cell, while being surrounded by corner-sharing metal halide octahedrons as shown in Figure 2.2.

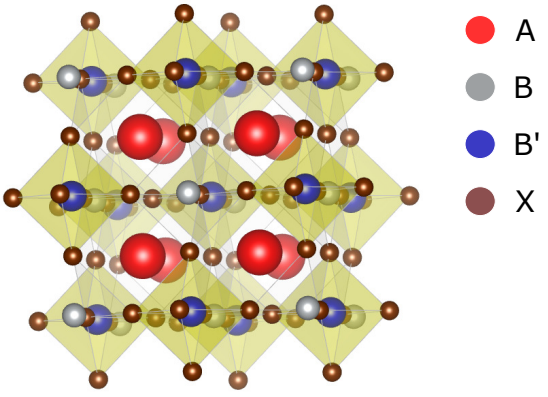

Figure 2.2: Typical $A_2BB'X_6$ crystal structure. The A site is usually occupied by large cations like Cs^+, Cu^+, MA^+ while a monovalent cation (Ag^+, Na^+, Au^+, Cu^+) and a trivalent cation (Bi^{3+}, Fe^{3+}, Sb^{3+}, In^{3+}) are used at the B and B' positions. This is surrounded by halogen anions Cl^-, Br^- or I^- at the X position.

As double perovskites have an additional B cation, the earlier introduced tolerance factor as an easy tool to screen for stable materials is no longer valid. In consequence,

another way to calculate the tolerance factor for additional ions in the crystal structure has been proposed by Bartel et al. in 2019.[67]

$$\tau = \frac{r_X}{r_{B^*}} - n_A \left(n_A - \frac{\frac{r_A}{r_{B^*}}}{\ln\left(\frac{r_A}{r_{B^*}}\right)} \right) \tag{2.3}$$

Here, r_A is the ionic radius of the A atom, whereas r_{B^*} accounts for both B cations using the arithmetic mean of the ionic radii of B and B'. Additionally, n_A represents the oxidation state of the A cation.[67] Using this tolerance factor, a stable double perovskite structure can be reached for $\tau < 4.18$.[67] However, no prediction of the crystal structure is possible when the new alternative tolerance factor is used.

One double perovskite, showing a tolerance factor of 3.96, is $Cs_2AgBiBr_6$, where Cs^+ is used as the A cation and Ag^+ as well as Bi^{3+} are the alternating B cations which are surrounded by Br^- at the X position of the crystal structure. Due to the promising optoelectronic properties, $Cs_2AgBiBr_6$ is one of the most widely used candidates for double perovskite solar cells yet.

In 2016, Slavney et al. first proposed $Cs_2AgBiBr_6$ as a potential candidate for perovskite photovoltaics due to its long photoluminescence lifetime of nearly 660 ns.[17] Further testing revealed an indirect bandgap of $Cs_2AgBiBr_6$ of roughly 2.1 eV.[68] However, even after investigations had shown that nonradiative recombination is one of the dominating processes in this material, the excellent stability in air and moisture shown by Slavney et al. still suggested that $Cs_2AgBiBr_6$ is a promising material for further investigation.[17]

While lots of research groups have investigated $Cs_2AgBiBr_6$, the properties of this material are still not completely understood.[18], [69] It was shown that exciton binding energies lie in the range of 268 meV and that generated charge carriers are strongly localized in the crystal lattice and therefore initially self-trapped after excitation.[65], [70] Hence, after the initial localization of charge carriers has taken place, the charge carriers diffuse to color centers and afterwards can contribute to radiative recombination.[65] Although the material shows multiple challenges for the application as a solar cell absorber, solar cells with efficiencies of up to 4.23 % were fabricated when combined with organic dyes.[71] Furthermore, a phase transition from cubic at room temperature to a tetragonal structure at around 122 K was observed by Schade et al. which makes investigating low temperature effects in this material intriguing.[18] The now stagnating efficiencies of $Cs_2AgBiBr_6$ solar cells make a better understanding of the material properties absolutely necessary in order to be able to make lead-free double perovskites applicable in perovskite photovoltaics.

In the next chapters, this thesis will provide insights into the influence of crystallization processes, crystal quality and stoichiometry on the physical and optoelectronic properties of $Cs_2AgBiBr_6$. In order to minimize the effects of stoichiometric variations and reproducibility of thin films with similar quality, a major part of this work is dedicated to the growth of high-quality single crystals. Using single crystals enables us to study the characteristic material properties without having to account for probable sample to sample variations or alterations of stoichiometry and crystallinity in thin films. The next chapter will therefore introduce the crystal growth and characterization techniques used to investigate the crystal quality and stoichiometry of the grown samples.

3 Crystal growth and verification of the crystal quality

Crystal growth has been a fascinating discipline which dates back as far as 1500 BC when people used the growth of crystals for retrieving sugar and salt.[72] However, only during World War II crystal growth became of technological importance.[72] Even today, high-quality crystals are of great importance as especially in the semiconductor industry high-quality silicon (Si) wafers are needed for a large variety of applications ranging from wafers for photovoltaics and transistors to high-power applications or detectors. In research, crystals are used for various purposes, one being the understanding of fundamental material properties disentangled from the synthesis conditions. In the field of perovskite research, much focus has been put on the synthesis of thin films. However, it has been shown in numerous publications in the past that the properties of a perovskite can depend strongly on the synthesis conditions. [19]–[21], [73]–[75] Therefore, the growth of perovskite single crystals can assist in growing high-quality perovskites under controlled conditions and hence being able to better investigate the fundamental physical properties of the perovskites. This approach has also been applied for the double perovskites presented and investigated in this thesis. The following chapter will therefore introduce the thermodynamics which drive crystal growth as well as different growth methods and characterization techniques to study the quality of the obtained crystals. In order to describe the basic theory of crystal growth, the next chapter will mostly rely on the work of Govindhan Dhanaraj et al. who summarized thermodynamic effects and details on crystals growth in "The Handbook of Crystal Growth".[72]

3.1 Theoretical basics of crystal growth

Generally, the growth of single crystals is strongly connected to a transition from a liquid or vapor phase (depending on the used precursor) to the solid phase of the crystal. Crystal growth, however, can only start if the equilibrium phase of the precursor, being solution or vapor, is slightly disturbed so that the free energy is no longer at a minimum.[72] In order to achieve this, one can use different methods such as increasing or decreasing temperature, pH value, pressure or other parameters. As a result, crystal growth in general can be divided into three steps. The first is the achievement of supersaturation. This is followed by nucleation of the crystallites which in a third step grow into larger single crystals. [72]
The next section will first take a closer look at the thermodynamic principles of crystal growth, followed by the kinetics of nucleation based on the work of Bohm et al. in 1989.[76]

3.1.1 Thermodynamic principles of crystal growth

As crystallization is described by a phase transition from the liquid, solid or gaseous phase to the solid phase a closer look will be taken at phase transitions.[76] Generally, a phase transition occurs when the free enthalpy G described by

$$G = U + pV - TS \tag{3.1}$$

is decreased. U hereby is the internal energy of the system, V the volume, S the entropy of the system, p the pressure and T the given temperature. When a phase transition from a liquid to a solid phase shall take place, the region of coexistence of the two phases has to be identified. This equilibrium can be described by the Clausius-Clapeyron equation:

$$\frac{dp}{dT} = \frac{\Delta S}{\Delta V} = \frac{\Delta H}{T \cdot \Delta V} \tag{3.2}$$

with ΔS, ΔH and ΔV being the changes in entropy, enthalpy and volume at the phase transition.

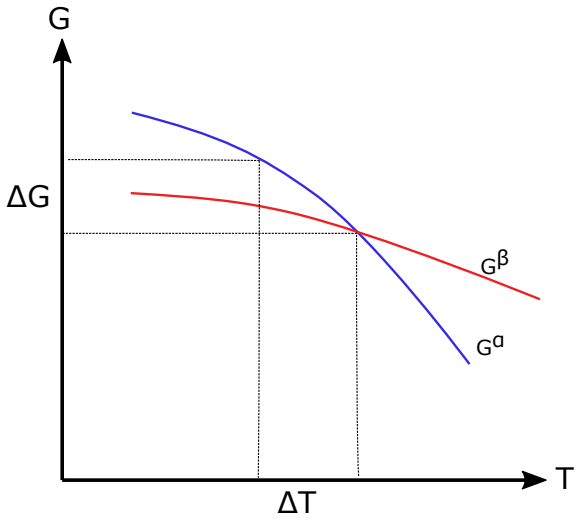

Figure 3.1: Change of the free enthalpy of two phases for varying temperature. G^{α} and G^{β} are the free enthalpies for the phases α and β. Adapted from [76]

Figure 3.1 shows the change of the enthalpies G for two phases, α being the liquid phase before crystallization and β being the solid phase after successful crystallization, depending on the chosen temperature. Here, α is the phase which is stable at higher temperatures. In the following, the change of thermodynamic potential, which is given by

$$\Delta\mu = \frac{\Delta G}{n} \tag{3.3}$$

with ΔG being the change of the free enthalpy and n being the amount of substance, is described more closely. In order to achieve the phase transition from liquid to solid phase, the change in the thermodynamic potential $\Delta\mu = 0$ has to be overcome. The thermodynamic potential for two phases is given approximately by

$$\Delta\mu = \mu^{\beta} - \mu^{\alpha} = \left(\frac{\partial\mu^{\beta}}{\partial T} - \frac{\partial\mu^{\alpha}}{\partial T}\right)\Delta T + \left(\frac{\partial^2\mu^{\beta}}{\partial^2 T^2} - \frac{\partial^2\mu^{\alpha}}{\partial^2 T^2}\right)\frac{(\Delta T)^2}{2} + \ldots \tag{3.4}$$

Additionally using

$$\left(\frac{\partial\mu}{\partial T}\right)_{p,x_i} = -S \tag{3.5}$$

$$\left(\frac{\partial S}{\partial T}\right)_{p,x_i} = \frac{C_p}{T} \tag{3.6}$$

and

$$\Delta S = \frac{\Delta H}{T} \tag{3.7}$$

Equation 3.4 can be rewritten to

$$\Delta\mu = -\frac{\Delta H_0}{T_0}\Delta T - \frac{\Delta C_p^0}{2T_0}(\Delta T)^2 ... \tag{3.8}$$

with ΔH_0 being the heat that occurs during the phase transition from α to β and C_p being the specific heat at constant pressure p. It can usually be assumed that $\Delta\mu$ is proportional to ΔT as otherwise the latent heat during phase transition had to be small, so that the second term of the above equation would be relevant. However, ΔH is negative as the latent heat is released by the system during crystallization. Additionally, ΔT is negative according to Figure 3.1. This means that $\Delta\mu$ will also be negative and therefore crystal growth can begin.
After minimizing the thermodynamic potential and therefore securing the basis for the possibility of crystal growth, crystal nuclei still have to be formed in order to start the growth process. For that, a closer look at the growth kinetics of a crystal is necessary. As soon as crystal a nucleus is forming in the solution, one can write the change of the free enthalpy as

$$\Delta G_n = \Delta\mu n_K \tag{3.9}$$

with n_K being the amount of substance of the nucleus. However, with the formation of a nucleus there also is a new boundary forming. Its enthalpy ΔG_F is then contributing positively to the free enthalpy. Moreover, the energy ΔG_E, caused by additional forces during nuclei formation, has to be considered when the nuclei are forming in glass vials. Therefore, the total free enthalpy is given by

$$\Delta G_K = \Delta G_n + \Delta G_F + \Delta G_E \tag{3.10}$$

and is visualized in Figure 3.2.

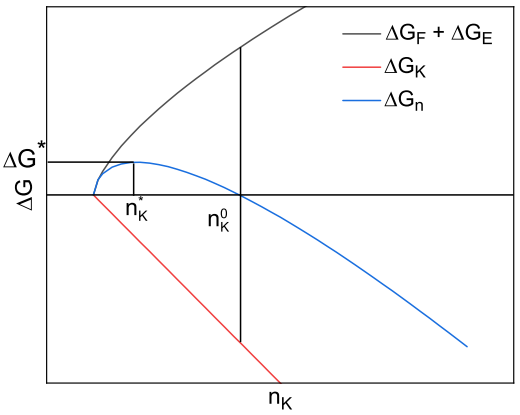

Figure 3.2: Schematics of the change of enthalpies during nuclei formation in dependence on the size of the forming nuclei. The critical size of the nuclei is labelled n_K. Adapted from [76]

Figure 3.2 shows that ΔG_K is only negative for nuclei sizes $n_K > n_K^0$. This in turn means that for values $n_K < n_K^0$ the free enthalpy is still positive. Therefore, work has to be put into the system in order to let the nuclei crystallize. Here, n_K^* is the critical size of a nucleus at which point the free enthalpy of the system is reduced and therefore the nucleus is stable and continues to grow. In consequence, nuclei which are smaller than n_K^* will dissolve again in the solution while only the nuclei larger than the critical size will continue to grow into crystals.[76]
This can also be put into a mathematical equation describing the critical radius r^* of the nuclei as well as the resulting critical enthalpy ΔG^*, shown in Equation 3.11 and Equation 3.12.

$$r^* = -\frac{2\sigma V}{\Delta\mu} = \frac{2\sigma V T_0}{\Delta H_0 \Delta T} \tag{3.11}$$

$$\Delta G^* = \frac{16\pi\sigma^3 V^2}{3(\Delta\mu)^2} = \frac{16\pi\sigma^3 V^2 T_0^2}{3\Delta H_0^2 (\Delta T)^2} \tag{3.12}$$

In addition to the critical parameters of nucleation, the nucleation velocity has to be controlled during crystal growth. When a crystal is grown from solution, one can assume that the different crystal nuclei are following the Boltzmann statistics in Equation 3.13. Hence, the number of forming and dissolving crystallites is a statistical process depending on the work which is done by the system in order to reach nucleation.

$$K^* = K_0 \exp\left(\frac{-\Delta G^*}{kT}\right) \tag{3.13}$$

However, the crystal nuclei will at some point leave the described equilibrium condition and will instead be stable and able to grow into crystals. This process can be

interpreted as a simple reaction which is described by an Arrhenius equation shown in Equation 3.14.

$$J = J_0 \frac{kT}{h} \exp\left(-\frac{G_A}{kT}\right) \exp\left(-\frac{\Delta G^*}{kT}\right) \tag{3.14}$$

Here, ΔG_A is an activation energy for the growth of crystal nuclei. Note that depending on the growth conditions, ΔG^* can be described proportional to ΔT or $\Delta \mu$. In conclusion, the rate of the nucleation is depending strongly on the experimental conditions such as temperature variations as well as variations in the thermodynamic potential for constant temperatures.
However, when crystals are pulled from solution in laboratory conditions, a few challenges have to be overcome. Firstly, the liquid phase equilibrium has to be overcome by small distortions to the system. The triggered nucleation is then often too fast and consequently too many nuclei are forming in the solution. One practical solution to these problems is the use of small seed crystals in the solution. By this means, the forming crystal is growing on top of the seed crystal without new nuclei having to be formed.[76] As the formation of crystal nuclei is no longer needed when seed crystals are used, the kinetics of crystal growth are different to the kinetics of crystal nucleation. Since no seed crystals have been used during this thesis, the growth kinetics of crystals using seed crystals will not be further described here.

3.1.2 Crystal growth and crystal habit

In the previous chapter, the thermodynamics and the conditions for nuclei formation have been explained. When a stable nucleus has formed, crystal growth is initiated. As crystals exist in various shapes, the question about the predictability of the equilibrium shape has to be considered. Especially the determining factors for the resulting equilibrium shape need to be taken into account. The shape of the crystal, including form and size of the crystal facets, is called crystal habit. Usually, the crystal habit is determined by different growth velocities of the crystal's facets, which will be discussed further in this section.[76]
Before elaborating about the crystal habit, the formation of single crystals is further explained. Walther Kossel developed a model to explain the formation of crystals from nuclei in 1989, which will be further explained in the following.[72]

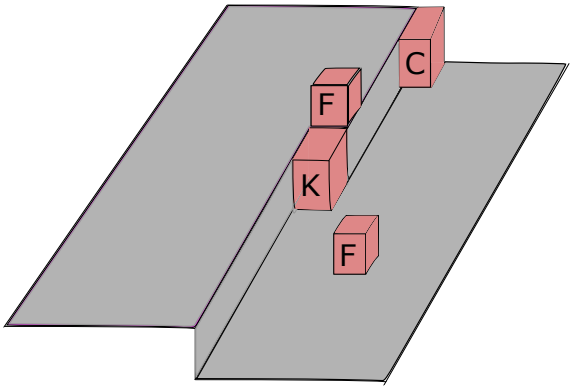

Figure 3.3: Schematics of nuclei adsorption onto a crystal surface. Adsorption onto a free space on the crystal surface is labeled as F, whereas C describes the start of a new chain on the crystal surface. However, the finishing of an already existing row by adsorption on kink sites K is possible as well. Adapted from [72]

Figure 3.3 depicts the sites of a flat crystal surface, on which crystal building blocks can be adsorbed. One of the most relevant sites where crystal unit adsorption occurs, is the kink site, shown as K in Figure 3.3. Kossel further discussed the adsorption sites for the growth of a NaCl crystal.[77] He found that in order to understand the growth process, one can use the molecular lattice energy as a quantification method for the adsorption of atoms at different locations of a plain crystal surface.[77] When adsorption of crystal building blocks takes place, the crystal units have three possibilities to attach to the surface. The first is the adsorption of a crystal unit freely on the crystal surface, labelled as F in Figure 3.3. The second possibility is the start of a new row on the crystal surface labelled as C in Figure 3.3. Thirdly, the finishing of an already existing chain, shown as K in Figure 3.3, is also possible for the crystal building blocks.
Kossel found that the finishing of a chain of the crystal is always energetically favored and therefore adsorption of crystal building blocks at kink sites is preferred.[77] As the crystal units continue to accumulate on the surface, they thereby finish the existing chains by diffusing to kink sites. Ultimately, the crystal units also start new rows and form the visible surfaces of the macroscopic crystal over time.
While forming the crystal surface, not all lattice planes will be visible as crystal facet but instead single planes (e.g. the (111) plane) are often the dominating facets of the crystal surface. In order to explain this effect, the growth velocity of the different crystallographic planes has to be taken into account.
The varying growth velocities are the main reason for the dominance of single lattice planes, visible as the surface facets of a crystal. Figure 3.4 shows the evolution of different crystal facets over time.

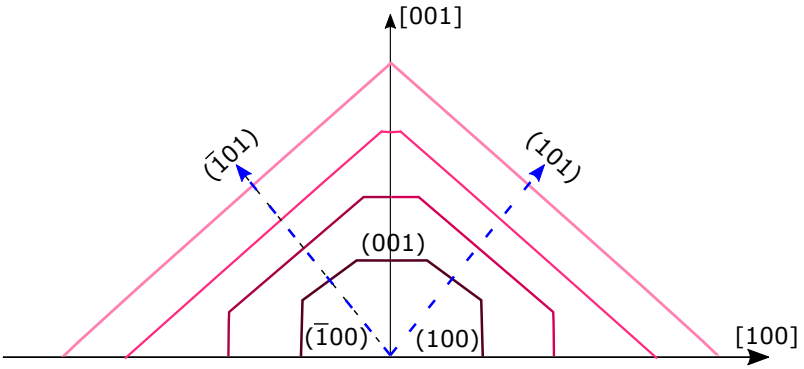

Figure 3.4: Schematics of the crystal facet growth at different times after nucleation. The different growth velocities $v_{(100)} > v_{(001)} > v_{(101)}$ result in the (101) facet of the crystal surface. Adapted from [76], [78], [79]

Kossel explained that the visible facets at the crystal surface are related to the growth velocity of each facet perpendicular to its corresponding lattice plane. The slower the growth velocity perpendicular to the lattice plane, the larger a facet width will become due to the increased growth velocities of the neighboring facets. This is also shown in Figure 3.4. Here, the growth velocity of the (101) plane is the slowest while the fastest growth can be seen for the (100) direction. Hence, while the (100) plane is quickly growing perpendicular to the [100] axis and therefore pushing for larger crystal dimensions, the (101) facet is growing more slowly perpendicular to the lattice plane and instead increasing its surface area over time while being dragged along by the (100) plane. As a consequence, for long enough growth times, only the (101) crystal facet will be visible as the crystal surface.[77]

3.2 Methods to grow crystals

After elucidating how the crystal habit is determined by varying growth velocities of crystal facets, this section will give insights into various methods to grow high-quality perovskite crystals. Although crystallization from melt is highly advantageous, especially for industrial applications like the growth of high-quality Si single crystals, this thesis focusses on the growth of crystals from solution.[79] Therefore, this section will deal with the various solution-based growth techniques.
Growth from solution has been a popular way to grow high-quality crystals since the 1930s.[79] The application of growth from solution is highly dependent on the solubility of the precursor materials. Hence, a good knowledge about the temperature dependence of the solubility is necessary and will be explained in more detail as a first step. Figure 3.5 shows the solubility for different materials on a logarithmic scale for temperatures between 20 °C and 80 °C.

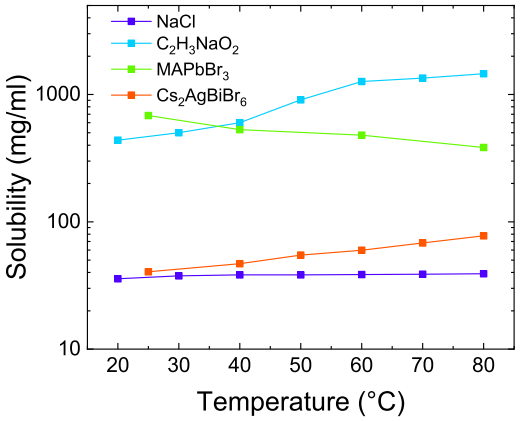

Figure 3.5: Solubility curves of sodium chloride (NaCl), sodium acetate ($C_2H_3NaO_2$), methylammoniumleadtribromide ($MAPbBr_3$) as well as cesium silver bismuth bromide ($Cs_2AgBiBr_6$). It can be seen that the solubility differs greatly for various materials, ranging from nearly constant solubility to even decreasing solubility for increasing temperature. Adapted from [80] and reproduced from [81] with permission from the Royal Society of Chemistry.

Figure 3.5 shows that the solubility stays nearly constant for NaCl while it is slightly increasing with temperature for $Cs_2AgBiBr_6$. Additionally, $C_2H_3NaO_2$ shows a strongly increased solubility at higher temperatures while a retrograde solubility is observed for $MAPbBr_3$.[28] The term retrograde solubility denotes a decreasing solubility when the solution temperature is increased.[28]

In order to grow high-quality crystals, a supersaturation of the precursor solution has to be reached. Supersaturation of a solution means that the concentration of the solution is slightly higher than the solubility at the growth temperature.[82] Figure 3.5 shows that supersaturation of a solution can be achieved in different ways, such as evaporation, employing antisolvents, heating up the solution or cooling it down.[76]

The above mentioned condition to reach supersaturation automatically leads to the different growth processes which have been developed over time. Crystal growth by

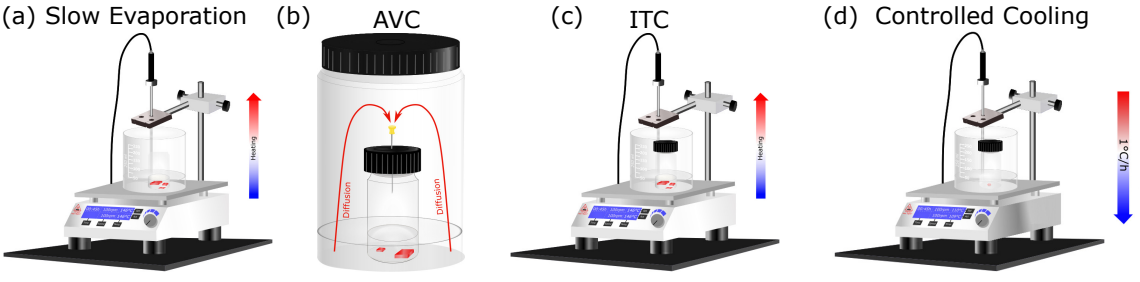

Figure 3.6: Schematics of the crystal growth setups of a) Slow Evaporation, b) Antisolvent-Vapor Crystallization (AVC), c) Inverse Temperature Crystallization (ITC) and d) Controlled Cooling. Adapted from [80]

slow evaporation (see Figure 3.6 a) is one of the simplest techniques to grow crystals, which is applicable especially for materials that do not show a temperature dependence of their solubility.[72], [83] For this method, a precursor solution is prepared by mixing several salts and dissolving them in a suitable solvent, with concentrations as high as the saturation point.[84] The solution is then left undisturbed at the desired temperature in a bottle with a perforated or slightly opened cap.[84] Most people already know this approach of crystal growth from daily life. A good analogy of the work principle of slow evaporation is the "pasta water" analogy. If salted pasta water is left on the stove top for a while, the water in the pot will completely evaporate and only NaCl crystals will be left on the bottom of the pot. This in turn means that by evaporating the water of the salt-water mixture, the concentration of NaCl in the liquid increases, reaching supersaturation at a certain point in time. This supersaturation then triggers the nucleation and crystallization of NaCl crystals. However, the NaCl crystal growth by leaving pasta water on your stove top results in rather poor-quality crystals. In order to obtain single crystals of high-quality, the growth parameters, such as temperature, evaporation rate and concentration of the solution have to be carefully controlled. The main advantage of crystal growth by evaporation is its applicability for a wide range of temperatures. In the case of $Cs_2AgBiBr_6$, the growth temperatures can be set between room temperature and 146 °C, with a growth time ranging from approximately 72 h to several months. Hence, even slight temperature variations of only 0.05 °C can greatly impact the growth velocity of the crystal and therefore lead to increased defect densities in the system.[72]

Another method to grow crystals at room temperature is the so called antisolvent-vapor crystallization (AVC) depicted in Figure 3.6b. Here, one uses so called antisolvents (solvents in which a material can not or only very poorly be dissolved) to reach supersaturation of the precursor solution. For this approach, a saturated precursor solution is prepared in a growth vessel.[83] This vessel is then placed into a larger vial, filled with an antisolvent. While the large vial is sealed, the smaller vial, containing the precursor solution, is kept open or covered with a perforated cap. Crystallization occurs when the antisolvent is slowly diffusing into the precursor solution. This process drastically decreases the solubility of the precursor salts in the prepared solution.[84] While the indiffusion of the antisolvent gradually decreases the solubility of the precursor solution, supersaturation is achieved and crystal growth initiated.[84] Single crystals can then be grown over a range of several hours up to several weeks. The antisolvents typically used for perovskites are chloroform or dichloromethane.[84] Although crystal growth by AVC is easily applicable at room temperature, controlling the crystal size is difficult.[84]

If the solubility curve of a material resembles the solubility of $MAPbBr_3$ in Figure 3.5, the material shows a retrograde or inverse solubility. In consequence, inverse temperature crystallization (ITC) can be employed. The exemplary setup for crystal growth by ITC is depicted in Figure 3.6c. For ITC, a saturated precursor solution is prepared at room temperature, completely dissolved and then placed onto a hot plate at temperatures exceeding room temperature. As the solubility of the material is decreased at elevated temperatures, supersaturation is achieved and nucleation and crystallization can start. This method is one of the typical growth techniques used for lead-halide based perovskites and was first introduced for perovskites in 2015 by Saidaminov et al.[28], [85] Although the growth temperatures of materials like $MAPbI_3$ and $MAPbBr_3$ typically lie at around 100 °C, it was also shown that growth temperatures can be reduced, while maintaining a high crystal quality, by additionally using primary alcohols as an additive in the precursor solution.[85], [86] As ITC is a highly controllable technique, which produces large crystals of high quality in short periods of time, it has become one of the most established growth techniques for perovskites up to date.[83], [87] To the best of our knowledge, however, no lead-free double perovskite crystal has been reported employing ITC as growth technique to this day.

Lastly, if solubility curves look like the ones of $Cs_2AgBiBr_6$ or $C_2H_3NaO_2$, which have an increasing solubility for increasing temperature, several possibilities to grow crystals exist. Clearly, slow evaporation as well as AVC are a possible growth technique. However, supersaturation can also be reached by slowly cooling down the solution as depicted in Figure 3.6d. This technique is called controlled cooling and is widely used for the growth of lead-free double perovskites.[17], [64], [88]–[90] Here, one dissolves the precursor in an appropriate solvent and then places the solution on a hot plate at elevated temperatures (e.g. 110 °C). The solution is kept at elevated temperatures for a couple of hours to completely dissolve the precursor salts in a first step. After that, the solution is slowly cooled down at a rate of 1 °C/h. Hence, supersaturation and nucleation occur when the solubility is lower than the initial concentration of the prepared solution.[84] When one employs this technique for double perovskites, acids like HBr and HCl are usually used as solvents.[17], [84], [91] It has furthermore been shown that the cooling rate is a critical parameter of crystal growth by controlled cooling. Yin et al. showed, that letting a solution cool down naturally leads to smaller crystals as well as crystals with poorer quality.[88] Hence, they conclude that during the crystal growth, a slow cooling rate is necessary in order to stay in the growth regime and therefore obtain high-quality and large single crystals.[88]

However, not all of the above described methods are applicable to lead-free double perovskites up to now. Therefore, this thesis will focus on the crystal growth of lead-

free double perovskites by controlled cooling and slow evaporation in the following chapters.

3.3 Quality assessment of crystals

After growing crystals from solution, one often studies the stoichiometry, structural properties and the crystal quality of the obtained samples. Furthermore, one often needs high-quality crystals for applications such as photodetectors but also when the fundamental physical properties of a material are to be investigated.[92]–[96]
In order to investigate the crystal stoichiometry and hence verify that the aimed crystal stoichiometry has been achieved, energy-dispersive X-ray spectroscopy (EDX) or X-ray fluorescence (XRF) can be employed. For further studying the structural parameters such as the crystal structure or the crystal quality, X-ray diffraction (XRD) is usually used. This section will give an overview over the consecutive measurement techniques and explain the fundamental principles behind X-ray analysis for crystal quality assessment.

3.3.1 XRF and EDX

In order to investigate the composition of a sample, X-rays as well as electrons can be used. By employing the techniques of EDX and XRF, it is possible to extract the elemental composition of a material by the emitted X-ray photons of the sample. Figure 3.7a illustrates the measurement geometry used when XRF is employed. During the whole measurement the angle α between X-ray source and detector stays constant as is depicted in Figure 3.7a. Furthermore, Figure 3.7b shows the process of X-ray fluorescence in more detail. If the energy of the incident ray is high enough, an electron from the inner shell can be excited and the atom becomes ionized. Hence, an electron is knocked out of the atom. Consequently, a vacancy is left in the K shell which needs to be filled by an electron from an outer shell (here the M shell). The residual energy of the electron relaxing to the K shell is then emitted by characteristic K_β radiation and can be specifically assigned to the transition from the M to the K shell of that specific element.[97]
Like this, the composition of the double perovskite crystals can be determined. The presented XRF data in this thesis was obtained using a General Electric XRD 3003 TT with monochromatic copper (Cu) K_α radiation source as well as an XR-100T detector from Amptek and an XRD setup from PHYWE with a molybdenum (Mo) K_α source.
Unfortunately, for lead-free double perovskites, XRF cannot confirm the exact stoichiometry of the grown crystals but merely provides information about the elements

contained in the grown perovskite crystal. Hence, to get exact information about the stoichiometry of the grown crystals, EDX is the characterization technique which should be used.

The basic principle of EDX is the same as of XRF unless electrons of variable energy are used for the excitation of the electrons in the atomic shell.[98] However, as the energy resolution of EDX is generally improved compared to XRF, EDX is a suitable technique for the determination of material stoichiometries.[98] Throughout this thesis, EDX characterization was performed by Stefan Braxmeier at the ZAE Bayern. The measurements were performed in high vacuum using an SEM Carl Zeiss Ultra 55+ and an INCAPentaFET-x3 Si(Li) detector.

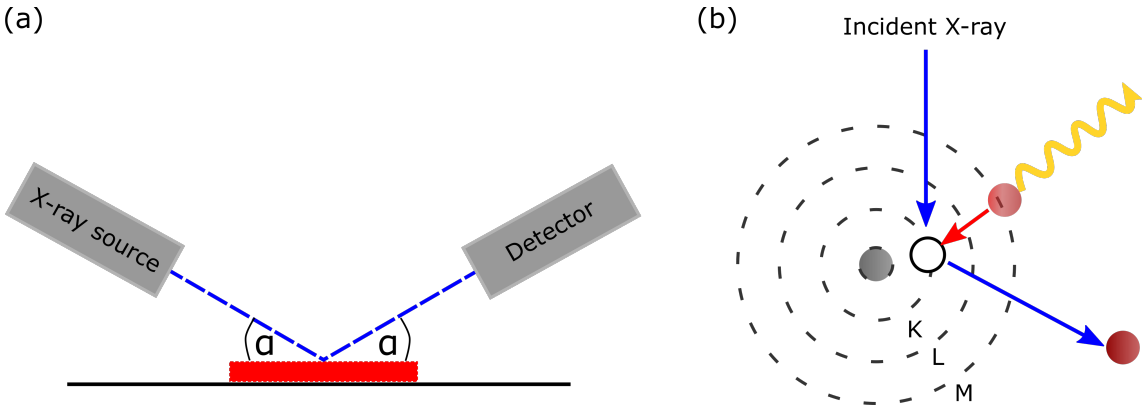

Figure 3.7: a) Measurement geometry for XRF spectra. b) Principle of XRF: The incident X-ray knocks out an inner shell electron. Hence, an electron from a higher lying shell can relax to the vacancy by emitting characteristic X-rays, specific for the related atom.

3.3.2 XRD

To further probe the structure of a material, powder XRD as well as single crystal XRD measurements are a helpful tool. However, when doing X-ray analysis on a material one should keep in mind that the electronic properties can easily be altered by X-ray radiation.[99] Especially, in organic compounds it has been shown that deep traps are introduced into the material, which affect charge carrier transport.[99] As a consequence, X-ray diffraction has only been measured on crystals which later were not used for other experiments in this thesis to exclude any effects on their optical and electrical properties due to X-rays. Also note, that only Cu-K_α and Mo-K_α radiation was used for XRD measurements throughout this thesis.

When XRD is employed, interference effects have to be considered. When an X-ray hits a material and therefore a lattice structure, the incident beam will be scattered. The direction of the scattering is described by the wave vector $|k| = \frac{2\pi}{\lambda}$ while the wave itself is

written as $A\exp\left(i(\vec{k}\cdot\vec{r}+\alpha)\right)$ with A being the amplitude of the wave, α the phase and $\vec{r}$ the radius of the points in space.[100] The basic principle of XRD relies on constructive

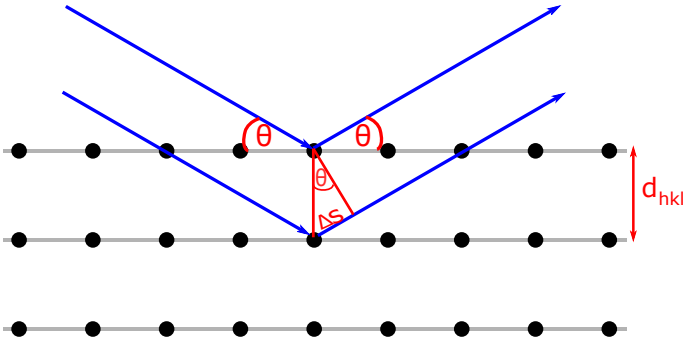

Figure 3.8: Scattering of X-rays by a sample. Adapted from [101] The incident X-rays are reflected from the lattice planes with distance d_{hkl} following the Bragg formula in Equation 3.15.[100]

interference of the incident rays as shown in Figure 3.8. When an X-ray hits the sample surface and therefore a lattice plane with distinct Miller indices (hkl), some of the rays will be reflected, whereas others can penetrate through the surface and will only be reflected at the next lattice plane, as shown in Figure 3.8. The distance of those lattice planes is d_{hkl}, also called the interplanar distance of the lattice. Hence, the condition for constructive interference of the rays and in consequence for a detected XRD peak can be described by Equation 3.15

$$n\lambda = 2d_{hkl}\sin\theta \tag{3.15}$$

with the interplanar distance d_{hkl} generally given by

$$d_{hkl} = \frac{1}{\sqrt{\left(\frac{h}{a}\right)^2+\left(\frac{k}{b}\right)^2+\left(\frac{l}{c}\right)^2}} \tag{3.16}$$

For a cubic system such as $Cs_2AgBiBr_6$ Equation 3.16 can be simplified to

$$d_{hkl} = \frac{a}{\sqrt{h^2+k^2+l^2}} \tag{3.17}$$

due to the identical lattice constant $a = b = c$ in all directions.[79] However, the Bragg condition depends on the energy of the incident X-rays. Hence, the location of observed diffraction peaks for different lattice planes differ in a diffractogram when different X-ray sources (e.g. Cu-K_α or Mo-K_α radiation) are used. To remove the wave-

length dependence in Equation 3.15, one can rewrite the Bragg equation in terms of the scattering vector q.[100]

$$q = \frac{4\pi}{\lambda} \sin\theta \tag{3.18}$$

The Bragg-Brentano geometry which fulfills Equation 3.15 is depicted in Figure 3.9a. Only when the scattered X-rays interfere constructively, a peak (corresponding to the specific lattice plane (hkl)) is visible in the diffractogram.[102] By assigning the Miller indices to the observed peak in a diffractogram, the lattice constant of a material can be calculated. Note that usually the diffractograms of powders are measured in order to calculate the lattice constant of a material. Although powder XRD provides a vast

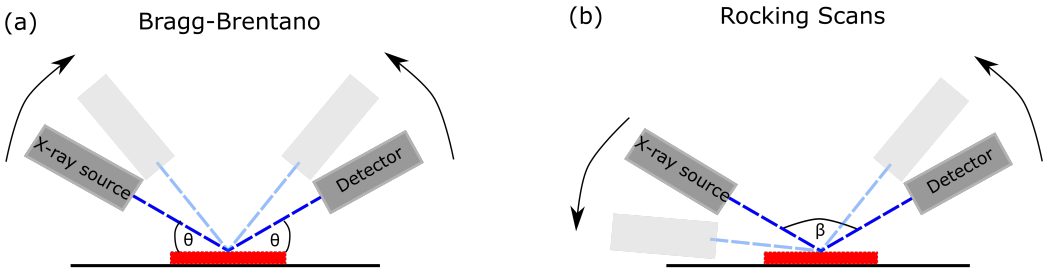

Figure 3.9: Scattering of X-rays by a sample. Adapted from [101] The incident X-rays are reflected from the lattice planes with distance d_{hkl} following the Bragg equation in Equation 3.15.[100]

amount of knowledge, including details about structural parameters such as the lattice constant, XRD patterns of crystals also contain lots of information. By measuring the XRD pattern of a crystal surface, one can draw conclusions about the growth direction of the crystal. This is due to the fact that only lattice planes parallel to the sample surface will fulfill the Bragg equation and therefore result in a peak in the XRD pattern.[102] As single crystals usually only grow along one axis of the unit cell, only one (hkl) plane and its corresponding higher orders will be visible in the XRD pattern.[102] Further, when single crystals are grown, the Bragg-Brentano geometry only provides information about the growth direction of the crystal. In order to study the quality of the grown crystals, rocking scans can be performed. When performing rocking scans the angle β between source and detector is set to a constant value, while source and detector are moved around the crystal as depicted in Figure 3.9b.

Conducting rocking scans can probe the mosaicity of a sample as peaks in XRD will only be observed when the Bragg condition is fulfilled, hence, when constructive interference between the incident rays is observed. In consequence, when only one single sharp peak is visible in a rocking scan, the single domains are all oriented in the same direction. However, when a rocking scan is broadened, the domains in the crystal are

slightly tilted towards each other, indicating a higher mosaicity of the crystal. In order to quantify the quality and mosaicity of a single crystal, the Full Width at Half Maximum (FWHM) is usually used whenever rocking scans are interpreted.[102]

4 Optical characterization

When new materials are studied, optical experiments can give important information about their physical properties. Optical methods are simple yet powerful techniques to probe the relationship of processing conditions and their influence on the physical properties of a material. Moreover, they provide essential information about bandgaps, defects and charge carrier recombination dynamics in a material. For this, the following chapter will introduce the techniques of photoluminescence (PL), photoluminescence excitation (PLE), photoluminescence quantum yield (PLQY) as well as absorption and the concept of Urbach energies.

4.1 The power of photoluminescence

Photoluminescence spectroscopy is a technique widely used to investigate the physical properties of materials. The principle of photoluminescence relies on the photoexcitation of charge carriers from the valence to the conduction band of a semiconductor. After excitation, the excited electrons will, by generation of phonons, relax to the energetically lowest level in the conduction band and ultimately recombine.[103] If the electron recombines radiatively with a hole, the energy is released by the emission of a photon, which subsequently can be detected during optical measurements. The spontaneous emission rate of a photon can be described by the Einstein coefficient A and the population of the excited state N using

$$\left(\frac{\mathrm{d}N}{\mathrm{d}t}\right)_{rad} = -AN \tag{4.1}$$

Solving Equation 4.1 leads to the radiative lifetime $\tau_{rad} = \frac{1}{A}$, which describes the lifetime of radiative recombination after excitation.[103] Although photoluminescence experiments rely on the detection of the radiative recombination of charge carriers, information about nonradiative and trapping processes can also be obtained by probing the

change of charge carrier density over time in transient PL experiments (trPL). Hence, the total recombination over time can be written as

$$\left(\frac{\mathrm{d}N}{\mathrm{d}t}\right)_{tot} = -\frac{N}{\tau_{rad}} - \frac{N}{\tau_{nonrad}} \tag{4.2}$$

with τ_{nonrad} being the lifetime for nonradiative processes.[103]
However, considering the different possible recombination mechanisms such as radiative band-to-band (second order) recombination, nonradiative Shockley-Read-Hall (first order) recombination and Auger (third order) recombination, Equation 4.2 can also be written as:

$$-\frac{\mathrm{d}N}{\mathrm{d}t} = k_1 N + k_2 N^2 + k_3 N^3 \tag{4.3}$$

Here, the recombination rates k_1, k_2 and k_3 represent the recombination rates for first, second and third order recombination in a material.
Additionally, the emission properties of a semiconductor closely correlate with its absorption properties. As the absorption defines the charge carrier density generated in a semiconductor, it is also a determining factor for the maximum photoluminescence intensity Y_{PL} which can be observed. Furthermore, the final PL intensity also depends on the blackbody spectrum Φ_{bb} as well as on the material's quasi-Fermi level splitting ΔE_f, which quantifies the intrinsic charge carrier density in the material.[104] Consequently, Equation 4.4 describes the photoluminescence spectrum of a semiconductor. Note, that Equation 4.4 assumes that the photoluminescence only stems from direct band-to-band recombination.[104] Another key assumption which leads to Equation 4.4 is that the absorptance and emission of a semiconductor are identical, as was stated earlier by Würfel.[104]–[107]

$$Y_{PL}(E) = \alpha(E)\Phi_{bb}(E) \cdot \exp\left(\frac{\Delta E_f}{k_b T}\right) \tag{4.4}$$

Equation 4.4 thus also shows that the emission spectra of PL is closely correlated to the absorption coefficient α and hence also correlates with the bandgap of the investigated material.
In consequence, photoluminescence spectroscopy can be used to study the photophysics and characteristic properties of a semiconductor. The following sections will describe the techniques and physics behind steady-state and transient photoluminescence as well as absorption in more detail.

4.1.1 Steady-state PL

In steady-state photoluminescence, only direct information about the radiative recombination of charge carriers can be extracted. Thus, only information about k_2 can be obtained. The radiative recombination rate k_2 is a material specific parameter described by the van Roosbroeck-Shockley equation,

$$k_2 n_i^2 = \int_0^\infty 4\alpha n_r^2 \Phi_{bb} dE \tag{4.5}$$

which connects the radiative recombination rate with the material's absorption coefficient. Here, α is the absorption coefficient, Φ_{bb} the blackbody spectrum and n_i the intrinsic charge carrier density of the perovskite.[108] However, steady-state photoluminescence also contains information about the applicability of materials in devices. The photoluminescence of a material is directly correlated to the achievable open-circuit voltage V_{OC} (represented by the quasi-Fermi level splitting ΔE_f) of a device by

$$\Delta E_f = \Delta E_f^{rad} + k_B T \cdot \ln(EQE) \tag{4.6}$$

where EQE is the external quantum efficiency or photoluminescence quantum yield. [109] In turn, this means that decreasing steady-state photoluminescene does not only result in increasing nonradiative losses but also that nonradiative losses will consequently lead to a decrease in the open circuit voltage of a device.[104]
To measure the steady-state PL of lead-free double perovskites, a FLS980 fluorescence spectrometer from Edinburgh Instruments was used. As light source a Xe-arc lamp or a pulsed EPL-375 diode laser with a wavelength of 375 nm and tuneable repetition rate was employed. Figure 4.1 shows the measurement setup of the FLS980.
Whenever the Xe-lamp is used for excitation, the beam is guided through a double monochromator in order to obtain light of a single wavelength. After that, the beam is directed into the sample chamber and lenses are used to further focus the beam onto the sample. A reference detector in the sample chamber monitors the intensity of the lamp and enables corrections of the detected PL spectra by the reference spectrum of the Xe lamp.
The emitted light from the sample enters the detection arm of the FLS980 and is guided through a double monochromator before it hits the photomultiplier system, which detects the intensity of the emitted light. The photomultiplier of the setup is constantly cooled to $-22\,^\circ$C in order to guarantee a low signal to noise ratio. It should also be noted, that employing the laser as an excitation source, the FLS980 can also be used for time correlated single photon counting (TCSPC), which will be explained in a later sec-

tion. The resulting PL spectra (shown in Figure 4.3a) can be plotted against the wave-

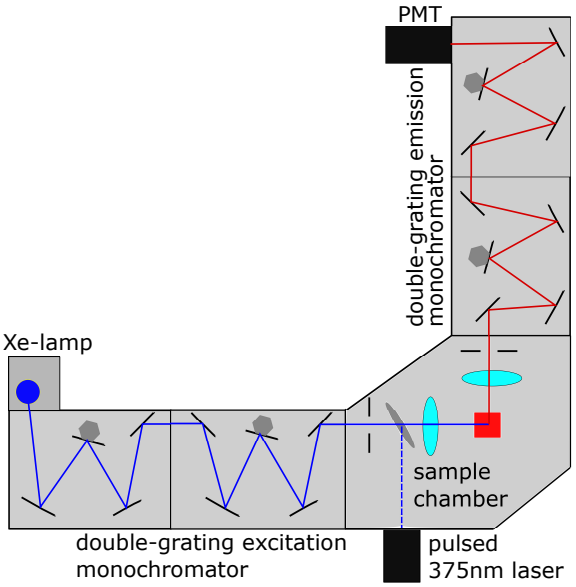

Figure 4.1: Measurement setup of the FLS980 PL spectrometer. The sample is excited either by a cw Xe-lamp or by a pulsed laser, while the PL is detected by a photomultiplier detection system.

length as well as against the energy. However, when a PL spectrum is converted from a wavelength dependence into an energy dependence, one needs to take the Jacobian transformation into account. A PL spectrum is recorded as PL intensity vs. wavelength units.[110] Nevertheless, as wavelength and energy are inversely proportional to each other, wavelength spacings are not identical to energy spacings as $\lambda = \frac{hc}{E}$. Using the Jacobi transformation one obtains

$$f(E) = f(\lambda)\frac{\mathrm{d}\lambda}{\mathrm{d}E} = -f(\lambda)\frac{hc}{E^2} \tag{4.7}$$

for the transformation of the data from intensity vs. wavelength to intensity vs. energy.[110]

Another possibility to investigate photophysical properties of a material is to perform fluence dependent steady-state photoluminescence measurements. Here, the sample is placed in a cryostat and PL is measured in transmission. A 415 nm Solis LED with variable power from Thorlabs is placed in front of the sample, while the integrated photoluminescence is detected by a silicon photodiode. An exemplary setup for fluence dependent PL is shown in Figure 4.2.

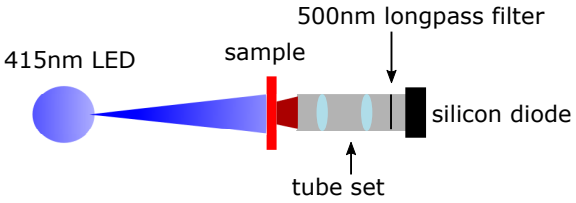

Figure 4.2: Measurement setup for fluence dependent steady-state PL. As the light source a 415 nm Solis LED (Thorlabs) is used. The sample is put in the setup in transmission geometry. In order to collect the light, a tube set with two lenses is used to focus the emitted PL onto a silicon diode which measures the integrated photoluminescence of the sample.

Fluence dependent steady-state PL is an easy tool to investigate the dominating recombination mechanisms in a material for different charge carrier densities. The quasi-Fermi level splitting, as a measure of PL, can also be written in dependence on the PL current density J_{PL}, which is proportional to the measured PL intensity and the photo current density in thermal equilibrium $J_{0,rad}$, as shown in Equation 4.8. Furthermore, J_{PL} can also be expressed in terms of the external photoluminescence quantum yield EQE_{PL} and the absorbed excitation flux J_{ex}. Inserting those variables in Equation 4.8, one obtains the expression of the second term. [111]

$$\Delta E_f = kT \ln\left(\frac{J_{PL}}{J_{0,rad}}\right) = kT\left[\ln\left(\frac{J_{ex}}{J_{0,rad}}\right) + \ln(EQE_{PL})\right] = \Delta E_{f,OC,rad} + kT\ln(EQE_{PL}) \tag{4.8}$$

with $\Delta E_{f,OC,rad}$ representing the maximum quasi-Fermi level splitting in the case of only radiative recombination.[111] Using the mass action law

$$\Delta E_f = kT \ln\left(\frac{n_e n_h}{n_i^2}\right) \tag{4.9}$$

with n_e and n_h being the electron and hole densities. One can further define the a slope m, in Figure 4.3b as $m = \frac{1}{p_e} + \frac{1}{p_h}$, with p representing the coefficient 1,2, or 3 for first, second and third order recombination of electrons and holes. Using the slope m one can then rewrite ΔE_f to

$$\Delta E_f \approx \left(\frac{1}{p_e} + \frac{1}{p_h}\right) kT \ln\left(\frac{J_{ex} - J_{e(h)}}{J_0}\right) = mkT \ln\left(\frac{J_{ex} - J_{e(h)}}{J_0}\right) \tag{4.10}$$

For optical measurements, one can assume the extraction rate of electrons and holes $J_{e(h)} = 0$ and the dark photo current $J_0 = const.$[111] In the case of pure optical experiments one can use the power law $n_{e(h)}^p$ for the quantitative description of the recombination processes. Here, p is again the coefficient 1,2 or 3 for the different recombination orders.[111].

In the case of pure second order radiative recombination, two particles take part in the recombination process. Therefore, $p_e = p_h$ will equal 2. Consequently, for purely radiative recombination one can expect a slope of $m = 1$, as m is given by $m = \frac{1}{p_e} + \frac{1}{p_h}$ in fluence dependent steady-state experiments.[111] As double perovskites often have large exciton binding energies, which are not neglectable at room temperature, one should also take excitons into account as a possible recombination mechanism.[70] In the case of excitons, literature has shown that a slope of 1 is often observed as well.[112], [113] This makes the interpretation of slopes in fluence dependent steady-state PL difficult as one cannot differentiate between recombination of excitons and band-to-band second order recombination.[112], [113] However, if the exciton binding energy of the investigated perovskite is known and larger than $k_b T$, one can assume that only a very small fraction of free carriers is present at room temperature, as suggested by the Saha-equation.[31] Therefore, the dominating recombination with a slope of 1 is caused by excitons.[31]

In the case of Shockley-Read-Hall (SRH) recombination, which is a first order process ($p_e = p_h = 1$), m should equal 2. However, this is not the case as the trap states in the middle of the bandgap will be occupied at different rates, depending on whether they are deep in the bulk or close to transport layers. Hence it was shown, that for single layers a slope of $m = 1.5$ should be expected.[111] This is caused by the charge selectivity of the midgap trap states. If the trap is selective for holes ($p_h = 1$), the electron can still recombine radiatively with another hole and therefore $p_e = 2$. In consequence, this leads to $\frac{1}{p_h} + \frac{1}{p_e} = \frac{3}{2}$.[111]

To complete the possible recombination mechanisms, Auger recombination will lead to a slope of $m = 2/3$ as three particles are participating in the recombination process.[111] Figure 4.3b shows a fluence dependent measurement of a $Cs_2AgBiBr_6$ thin film. It is visible that for low excitation intensities only slopes of $m = 1.5$ are visible, indicating dominating first order or trap assisted recombination. For higher intensities slopes of $m = 1$ are observed, which hints towards either radiative band-to-band recombination or recombination of excitons as the dominating recombination pathway. However, due to the high exciton binding energy of this type of double perovskite, slopes of $m = 1$ will be interpreted as excitonic processes during this thesis.

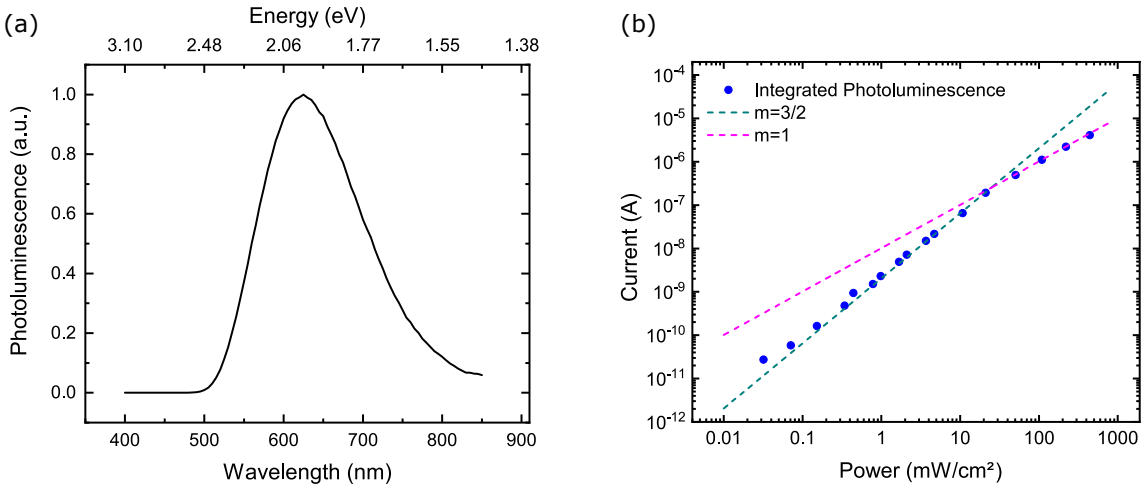

Figure 4.3: a) Exemplary PL spectrum of a) $Cs_2AgBiBr_6$ lead-free double perovskite measured with the FLS980 spectrometer. b) Fluence dependent steady-state PL showing different recombination regimes for varying excitation powers.

4.1.2 Transient PL

When the charge carrier dynamics of a system are of interest, transient photoluminescence (trPL) can be used to gain information about the rate constants for first, second and third order recombination as well as about the photoluminescence lifetimes of a material.[104]

Transient PL can typically be measured in two different configurations. Firstly, measuring trPL with a streak camera where the changing PL spectrum is recorded over time is possible. Hence, a trPL curve can be obtained when crosssections at specific wavelengths are taken.

Secondly, time correlated single photon counting (TCSPC), which has been used in this thesis, can be employed. Here, the measurement principle is similar to a stop watch as is presented in Figure 4.4. The excitation pulse (here a 375 nm pulsed laser) is exciting the sample. Additionally, the same laser pulse also initiates a trigger signal which is working as the start signal for the counter in the setup. The emitted PL then moves through the setup to the PMT detector. As soon as the first photon reaches the PMT, the counter stops. Hence, with every excitation event, there is a measurable time difference between start and stop pulse of the counter. As photon emission is a highly statistical process, the distribution of the different delay times after the start pulse can be monitored in a histogram. Hence, if only enough start-stop events are performed, the TCSPC or trPL curve can be monitored and analyzed. In this thesis, all TCSPC measurements were performed with the FLS980 in the configuration shown in Figure 4.1 and a pulsed diode laser as the excitation source. The achieved time resolution of this setup is approximately 2 ns and limited by the instrument response function of the

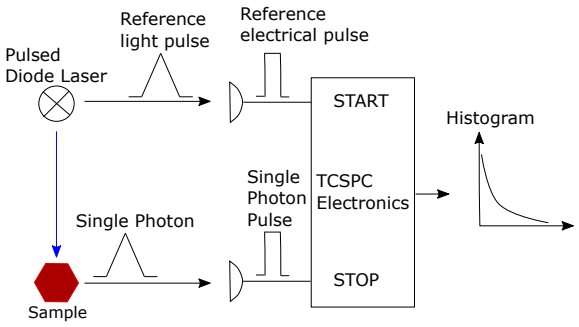

Figure 4.4: Schematics of the working principle of a TCSPC measurement.

setup. However, as PL lifetimes of perovskites are typically much longer than 2 ns, the FLS980 is a suitable spectrometer to investigate charge carrier dynamics of perovskite materials.

When it comes to analyzing trPL data, the rate equation in Equation 4.3 needs to be accounted for. In Equation 4.3, three processes are contributing to the change of charge carrier density over time. If we assume only first order recombination in a material, Equation 4.3 can be rewritten to:

$$-\frac{\mathrm{d}N}{\mathrm{d}t} = k_1 N \tag{4.11}$$

The solution to this equation would then be a standard exponential function $N(t) = N_0 \exp\left(-\frac{t}{\tau_1}\right)$ with $\tau_1 = \frac{1}{k_1}$, describing the PL lifetime of a purely first order process. This in turn means that if only SRH recombination is happening in a material, the trPL should look like a straight line on a logarithmic scale. However, for lead-free double perovskites, the decays are usually more complex as shown in Figure 4.5. The trPL de-

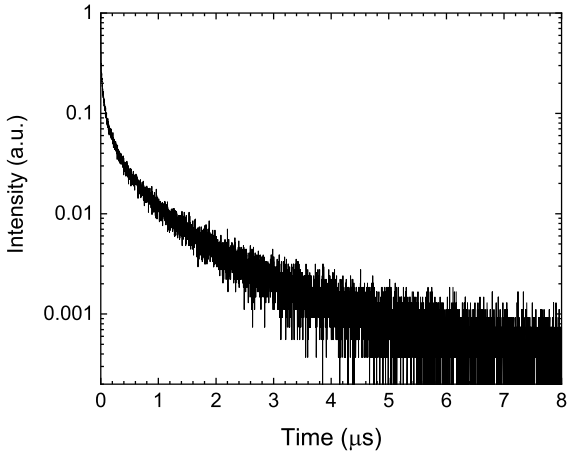

Figure 4.5: Transient PL decay of a lead-free double perovskite thin film. The shape of the trPL curve does not suggest a purely first order decay, but suggests that other processes dominate the recombination dynamics.

cay for a lead-free double perovskite in Figure 4.5 is clearly not monoexponential at the

used laser fluence. However, it is common practice within the community to fit such a decay with multiple exponential functions.[17], [91], [114]–[118] Doing this, one receives several different values for the lifetime of the material: one in a very short time range of a few ns, then one on a longer timescale of tens of ns and an even longer one in the range of hundreds of ns.[17], [91] When fits are done for multiple different samples of different stoichiometry or annealing temperatures, one can get an idea about the different timescales on which the PL is decaying. Therefore, fits can be used to illustrate the PL decay times in a quantitative way. Furthermore, the different decay times obtained by multi-exponential fits are often related to band-to-band or trap assisted recombination.

Although fitting multiple exponentials to a decay as shown in Figure 4.5 is common practice and acceptable in order to quantify and compare different samples, interpreting the obtained lifetimes as physical processes is strictly speaking not possible.[119], [120] As an exponential function only solves for pure first order recombination in a material, as shown in Equation 4.3, this would mean that the decay in Figure 4.5 consists of several different and independent first order processes while at the same time second order recombination is not present.[104], [119], [121] This however is fairly unknown for perovskite semiconductors and additionally, rate models have shown that it is usually not the case.[121]

Whenever trPL is measured, the used excitation fluence must be stated. As shown earlier for steady-state fluence dependent PL in Figure 4.3, the dominating recombination regime is changing when going from high to low excitation fluences. In trPL this has been shown in detail by Staub et al. when they showed that purely first order recombination can be seen for low excitation fluences.[104], [120] Hence, a straight line in the trPL data is visible on a logarithmic scale. When the excitation fluence increases, second order processes become more important. This changes the trPL curve from a straight line to a curve which is no longer monoexponential.[104], [120] As a consequence, trPL transients can be used in order to study the dominating recombination mechanisms of semiconducting materials, when the experiments are performed at several different fluences.

4.2 PLQY as tool for quality assessment of double perovskites

Another way to characterize crystals as well as thin films is photoluminescence quantum yield. The PLQY of a sample is a direct measure of the fraction of radiative recom-

bination, which a material emits relative to its absorption.[122] Generally, the quantum yield of a material can be calculated by

$$PLQY_i = \frac{k_2 N^2}{k_1 N + k_2 N^2 + k_3 N^3} \tag{4.12}$$

under the assumption that $n = p$.[104] This shows that the theoretical quantum efficiency of a semiconductor is strongly dependent on the rates k_1 and k_3, as the radiative recombination rate is a material dependent parameter. However, the nonradiative recombination rates k_1 and k_3 describing SRH and Auger recombination also have a significant impact on the quantum efficiency. Especially the nonradiative recombination of a material can be strongly influenced by trap states and defects introduced into the system during the fabrication. Hence, the PLQY can be used to quantify the quality of a material as well as its recombination losses.

However, when a material emits light, one has to consider that not all photons created in the sample will actually be outcoupled. To be more precise, some of the generated photons will be reabsorbed into the sample with a probability p_r while others will actually be emitted into the integrating sphere with a probability p_e.[104] Hence, Equation 4.12 only describes the internal PLQY, while the actually measured external PLQY is written as

$$PLQY_e = \frac{p_e PLQY_i}{1 - p_r PLQY_i} \tag{4.13}$$

In order to assess the PLQY experimentally, the samples are placed in an integrating sphere. For this thesis, the PLQY was measured in the FLS980, which has an adaptable sample holder for an integrating sphere. As the excitation source, a 405 nm diode laser was placed in front of the integrating sphere to create a defined illumination spot on the sample.

For being able to calculate the PLQY six different measurements in three configurations need to be conducted. A schematic of the three different measurement geometries is presented in Figure 4.6. In a first step, the spectrum of the excitation laser is measured in the configurations shown in Figure 4.6. One starts with the measurement of the laser spectrum L_a and an empty integrating sphere. This is followed by a measurement of the laser spectrum with the sample placed inside the integrating sphere but under indirect illumination (see Figure 4.6b). The resulting spectrum will be referred to as L_b. Lastly, the sample is placed directly in the excitation beam and again, the laser spectrum is measured, which is now called L_c (see Figure 4.6c). In a later step, L_c and L_b will give information about the absorption of the sample.

Following the laser spectrum, one also needs to measure the PL of the sample in the integrating sphere. For that, a reference measurement of the empty integrating sphere,

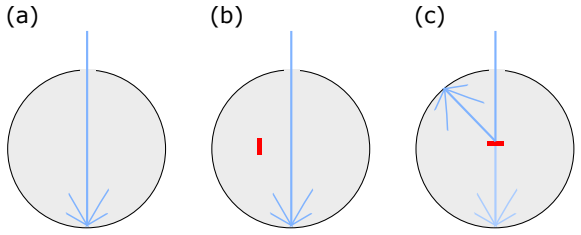

Figure 4.6: Measurement geometry for PLQY experiments. The sample is placed in an integrating sphere. However, several measurements are necessary. a) without the sample in the integrating sphere, b) with the sample in the sphere placed in a way, that direct light cannot hit the sample and c) direct illumination of the sample.

as depicted in Figure 4.6a, is performed which is called P_a. Then again, the sample is placed in the sphere without being directly illuminated and the PL of the sample is tracked (Figure 4.6b). This is spectrum P_b. Finally, the PL of the sample is measured with the sample directly in the excitation beam (Figure 4.6c). This measurement is referred to as P_c. Figure 4.7 shows the resulting spectra for all performed measurements as an example. The calculation of the external PLQY is done as suggested by de Mello

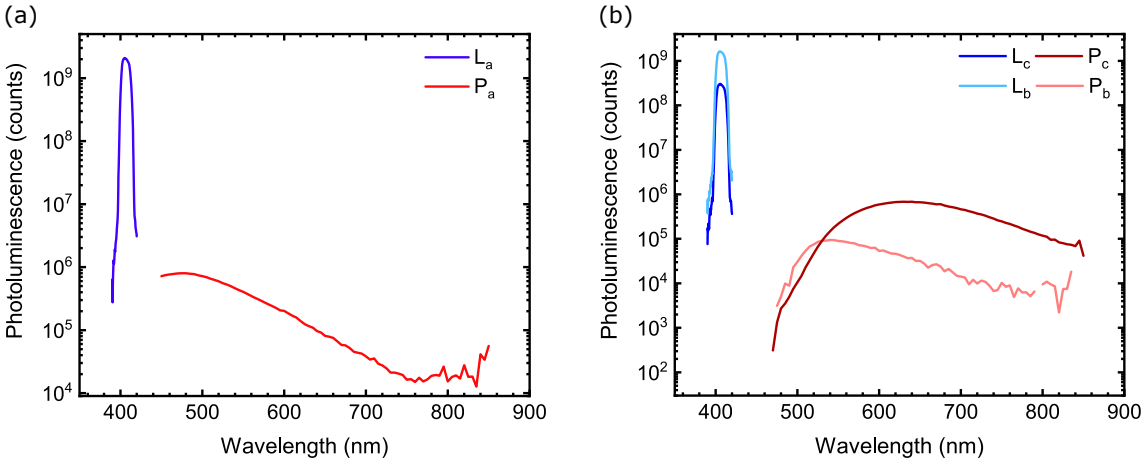

Figure 4.7: Exemplary measurement for PLQY on a lead-free double perovskite. a) shows the reference measurements L_a of the laser spectrum and P_a of the empty integrating sphere. b) shows the measurements L_b and L_c of the laser spectrum with the sample under indirect and direct illumination as well as the PL of the sample under indirect P_b and direct P_c illumination.

et al.[122] Note that in order to calculate the PLQY, the integrated PL values are used for the evaluation. At first, the absorption of the sample is calculated by

$$A = 1 - \frac{L_c}{L_b} \tag{4.14}$$

Knowing the absorption of the sample, one now deals with the obtained emission spectra P. Figure 4.7a clearly shows that the integrating sphere itself emits light. Therefore,

the actual sample PL is calculated by subtracting P_a from the PL data P_b and P_c. Like this, the spectra in Figure 4.7b are obtained. As a next step, the number of absorbed photons is calculated by

$$\#\text{photons}_A = L_a \cdot A \tag{4.15}$$

Knowing the absorption properties of the sample, one can now deal with the number of emitted photons in the next step. The emission is given by

$$\#\text{photon}_E = P_c - (1 - A) \cdot P_b \tag{4.16}$$

Finally, the PLQY can be calculated as

$$PLQY_e = \frac{\#\text{photons}_E}{\#\text{photons}_A} = \frac{L_a \cdot A}{P_c - (1 - A) \cdot P_b} \tag{4.17}$$

From Equation 4.17 one clearly sees how increased nonradiative recombination will affect the PLQY value. As nonradiative recombination increases and hence $\#\text{photons}_E$ decreases while $\#\text{photons}_A$ stays constant, a decrease of the PLQY can be expected. Hence, PLQY is an easy method to optimize the fabrication parameters of devices and thin films.

4.3 Optical characterization of perovskite crystals by absorption

Using PL spectroscopy to investigate the properties of a material gives important information about charge carrier dynamics as well as nonradiative recombination losses. However, if the bandgap and defects are of interest, absorption spectroscopy can be employed.
Additionally, one has to consider that PL spectroscopy is generally a surface sensitive technique due to the low penetration depth of the excitation beam. Hence, using absorption measurements and employing a white light source can give additional information about the bulk properties of a material. Especially when crystals are used, absorption experiments should be conducted additionally to PL measurements in order to gain more information about the bulk properties of the crystal. Therefore, the following section will introduce different techniques to measure absorption on a crystal and introduce the concept of Urbach energies.

4.3.1 Light absorption in semiconductors

When a photon is absorbed by a material, an electron from the valence band of the material is excited into the conduction band of the semiconductor. The transition rate of the electron into the conduction band depends on the density of states as well as on the matrix element M describing the effect of light on the electrons.[103] The matrix element is given by

$$M = \int \psi_f^*(\vec{r}) H'(\vec{r}) \psi_i(\vec{r}) d^3\vec{r} \tag{4.18}$$

Here, H' is the perturbation arising from the light wave described by

$$H'(\vec{r}) = e\vec{\epsilon}_0 \vec{r} \exp(i\vec{k}\vec{r}) \tag{4.19}$$

while $\vec{r}$ is the vector describing the position of the electron. Furthermore, the electron states in the semiconductor can be described by Bloch functions. Hence, the wavefunctions $\psi_f(\vec{r})$ and $\psi_i(\vec{r})$ can be rewritten depending on the periodicity of the crystal lattice.[103] The absorption properties of a semiconductor also depend on the joint density of states for parabolic bands which is described by

$$g(E) = \frac{1}{2\pi^2} \left(\frac{2m*}{\hbar^2} \right)^{\frac{3}{2}} E^{\frac{1}{2}} \tag{4.20}$$

with m^* being the effective mass of the electron.
For a direct semiconductor and excitation of charge carriers above the bandgap Equation 4.20 changes to

$$g(E) = \frac{1}{2\pi^2} \left(\frac{2\mu}{\hbar^2} \right)^{\frac{3}{2}} (E - E_g)^{\frac{1}{2}} \tag{4.21}$$

with μ being the effective electron-hole mass.[103]
While in a direct semiconductor, the electron is excited directly from the valence into the conduction band, in an indirect semiconductor, an additional phonon participates in the absorption (and emission) process.[103] As a result, the absorption coefficient α of a direct bandgap semiconductor is proportional to $\alpha(E) = 0$ for $E < E_g$ and $\alpha(E) \propto (E - E_g)^{\frac{1}{2}}$ for excitation energies $E > E_g$. However, for an indirect semiconductor the absorption coefficient changes to $\alpha_{\text{indirect}}(E) \propto (E - E_g \mp \hbar\Omega)^2$, as the phonon contribution has to be included.[103] Hence, the absorption coefficient also contains information about the nature and energy of the material's bandgap. Moreover, if the absorption coefficient of a material is known over a wide range of energies, the bandgap of a material can be determined.
Unfortunately, in standard measurements the absorption coefficient of a material is not directly accessible. As a consequence, only the absorption A of the material can be

accessed experimentally.
When light with intensity I_0 is shone onto a material, the light intensity $I(d)$ is attenuated according to the law of Lambert-Beer

$$I(d) = I_0 \exp(-\alpha(E)d) \tag{4.22}$$

Experimentally, this is realized by measuring transmittance and reflectance of a material. Such measurements are usually conducted by placing the sample in an integrating sphere and using a tuneable white light source for excitation. By measuring I_0 of the light source, followed by measuring the remaining intensity of the light while the sample is inside the integrating sphere, the reflectance R and transmittance T of the sample can be obtained. The resulting absorptance is then given by

$$A = 1 - T - R \tag{4.23}$$

Figure 4.8 shows the evolution of the absorptance spectra of a material for different calculated sample thicknesses. In Figure 4.8 one sees that no information about the bandgap of the material can be obtained from just plotting the absorptance vs. wavelength as the absorption onset is redshifting continuously with increasing layer thickness. Hence, only the absorption coefficient can be considered a thickness independent material parameter and should therefore be calculated when the absorption properties of a material are investigated. Due to the large thickness of the crystals pre-

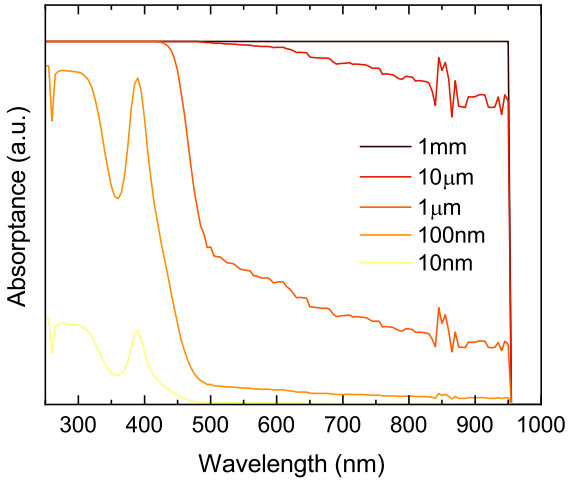

Figure 4.8: Evolution of the absorption onset of a material for different layer thicknesses. The absorption onset is redshifting with increasing sample thickness and hence does not include information about the bandgap of the sample.

sented in this thesis, the following sections will elaborate on different measurement techniques to gain information about the absorption properties of the grown lead-free

double perovskites.
In a first step, crystal transmission is introduced to get knowledge about subbandgap absorption. Secondly, photoluminescence excitation can be used as a surface sensitive technique to gain knowledge about the absorption properties above the bandgap of a perovskite crystal.

4.3.2 Transmission measurements

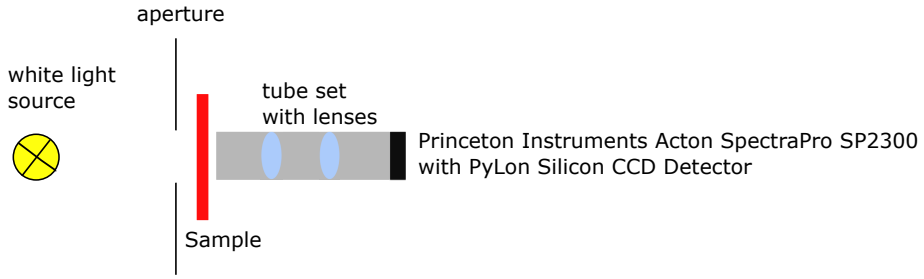

Figure 4.9: Measurement geometry for transmission experiments on lead-free double perovskite crystals. The sample is placed in a cryostat and excited with white light. In order to limit the spot size to the size of the crystal, an aperture is glued on top of the crystal. A tube set is used to collect and focus the transmitted light. The collected transmittance is detected by a PyLon Silicon CCD Detector.

To measure the transmittance of a crystal, the sample is glued onto a glass substrate and placed inside a cryostat. A white light source is used to excite the sample. The beam is guided through an aperture to limit the spot size to the size of the investigated crystal. The transmitted light is then collected by a tube set and focused into a fiber, connected to a Princeton Instruments Acton SpectraPro SP2300 Spectrometer. The transmission signal is detected by a cooled PyLoN Silicon CCD Detector. Additionally, the lamp spectrum is measured separately as a reference in order to correctly calculate the transmittance of the crystal.
The transmission of the crystal is then calculated by $T = \frac{I_{\text{crystal}}}{I_{\text{lamp}}}$. The absorption was obtained using Equation 4.23 with $R = 0$, as the reflectance is neglected during this measurement. Using the law of Lambert Beer as

$$A = 1 - \exp(-\alpha d) \tag{4.24}$$

the absorption coeffcient can be calculated.

4.3.3 Photoluminescence excitation

Due to the large thickness of the crystals, transmission measurements can only probe states below the band edge of the crystal, as the absorption coefficient of the material is rather high at energies above the band edge. Hence, only light with energies in the range of low absorption coefficients will be transmitted, while light with energies above the bandgap will be completely absorbed by the crystal. However, when a surface sensitive technique, such as PLE is applied, it is still possible to monitor the optical properties of a material at energies above the bandgap, due to the low penetration depth of the incident light and the measurement being performed in a reflection geometry.
As PLE measures the emitted photoluminescence for different excitation wavelengths, the obtained signal is still determined by radiative recombination in the sample. Hence, the PLE intensity will depend on the PLQY of the sample given by Equation 4.12.[123] However, it has been shown that PLE can still be treated as a measure of absorption, if two concerns can be addressed. First, the detected PL intensity has to be dependent on the absorption coefficient of the material. This rule has been formulated by Vavilov in 1922 and means that the PLQY of a material is independent of the excitation energy.[124] Second, Kasha's rule also has to be fulfilled. Kasha states, that the observed emitting state must always be the lowest excited state in a material.[125] Although there are materials which violate both of those rules, no such violation was found for lead-free as well as lead-halide perovskites up to date. Therefore, PLE can be treated as a measure of absorption when lead-free double perovskites are investigated.
In this thesis, PLE was measured using the FLS980 setup, presented in Figure 4.1. Before measuring the PLE of a crystal, a PL spectrum was always obtained in order to provide the wavelength of the PL maximum. For PLE, the PL emission wavelength is fixed to the position of the PL maximum, while the excitation wavelength is continuously changed. Like this, the intensity of the PL can be tracked for different excitation wavelengths, allowing the electronic energy structure of a material to be tracked similarly to conventional absorption spectroscopy.[126]

4.3.4 Characterization of tailstates by Urbach energy

Ideally, the absorption of a semiconductor shows a steep increase of the absorption coefficient at the bandgap. However, a more gradual absorption edge is often observed in indirect semiconductors or materials which show a high density of tailstates.[127] Tailstates are considered a density of states which extends into the bandgap of a semiconductor and in consequence presents a possibility for parasitic recombination of charge carriers and a broadening of the absorption edge.[128]–[130] In turn, such par-

asitic recombination can lead to additional losses of the open circuit voltage (V_{OC}) of a solar cell.[130] Hence, when designing an absorbing layer, additional attention should be paid to the reduction of tailstates.[131]

Those states below the bandgap can be caused by either structural or thermal disorder, which can be introduced during the fabrication of the material.[132] Additionally, phonons, static disorder, defects, as well as variations of the bond lengths and band gap fluctuations can lead to the observation of tailstates in a material.[129], [130] In order to describe subbandgap states phenomenologically, Urbach energies E_U can be used if an exponential absorption tail is observed.[133], [134] Subsequently, using Equation 4.25 to fit the low energy part of the absorption spectra makes an estimation of the Urbach energy possible.[134]

$$\alpha(E,T) = \alpha_0 \exp\left(-\frac{E_0 - E}{E_U(T)}\right) \tag{4.25}$$

Here, E_0 is the energy of the material's absorption edge, E the photon energy and $E_U(T)$ the Urbach energy, representing the slope of the absorption edge. The temperature dependence of the Urbach energy can also be expressed by summation of a static and a dynamic contribution. The static contribution to the Urbach energy is caused by structural disorder while the dynamic contribution takes thermal broadening into account as shown in Equation 4.26.[134]

$$E_U(T) = E_U^{stat} + E_U^{dyn}(T) \tag{4.26}$$

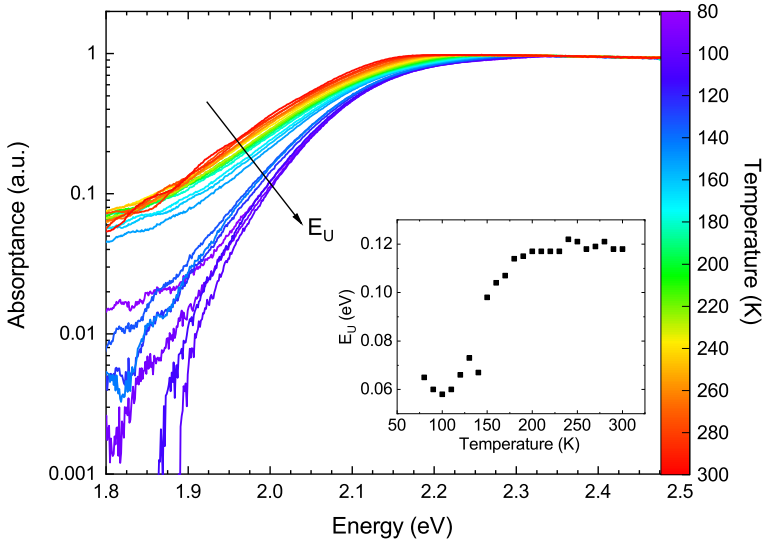

Figure 4.10: Temperature dependent absorptance of a lead-free double perovskite showing the temperature dependence of the absorption tail. In the inset the extracted Urbach energies are depicted for the measured temperature range.

Figure 4.10 shows the temperature dependence of the absorption edge and Urbach energies for a $Cs_2AgBiBr_6$ crystal. The absorptance was obtained by transmission measurements of a crystal as described in subsection 4.3.2. Figure 4.10 also shows a continuous decrease of the Urbach energy from 180 K to 100 K, indicating a change of the material's disorder at lower temperature. This shows that absorption measurements and Urbach energy fitting can also be used to gain knowledge about the structural disorder and defect properties over a wide temperature range.[131]

5 Influence of crystallization and precursor stoichiometry on the physical properties of $Cs_2AgBiBr_6$

High-quality single crystals are a good model system to investigate the physical properties of a material independent of stoichiometric changes, which can be introduced during sample fabrication. Therefore, the first part of this chapter will deal with the impact of growth temperature and growth method on the optical properties of high-quality $Cs_2AgBiBr_6$ crystals. Here, a new growth technique based on the slow evaporation of organic solvents is introduced. Comparing the solubility curves of the newly established evaporation technique to the conventional controlled cooling method, the advantages of the developed growth method can be proven. Moreover, it is shown that the growth temperature significantly affects the optical properties of crystals. By relating the crystal growth conditions to changes in the optical properties of this material, the first part of this chapter will contribute to a better understanding of the structure-property relationship of $Cs_2AgBiBr_6$ and like this provide a solution for further optimization of $Cs_2AgBiBr_6$ solar cells.
The second part of this chapter will then elaborate on the impact of small stoichiometric changes on the optoelectronic properties of $Cs_2AgBiBr_6$ thin films. In order to analyze the influence of the stoichiometric changes, a focus will be set on structural and optical measurements, such as XRD, PL and PLQY. It will be shown that a small excess of Bi in the film leads to higher crystallinity in the film, as well as longer PL lifetimes and higher power conversion efficiencies in the fabricated device.

5.1 Influence of crystallization on the structural and optical properties of $Cs_2AgBiBr_6$ perovskite crystals

The work presented in this section is based on the publication "Influence of crystallisation on the structural and optical properties of $Cs_2AgBiBr_6$ perovskites crystals" by **Melina Armer**, Julian Höcker, Carsten Büchner, Sophie Häfele, Patrick Dörflinger, Maximilian T. Sirtl, Kristofer Tvingstedt, Thomas Bein and Vladimir Dyakonov published in CrystEngComm in 2021, volume 23, pages 6848-6854.

5.1.1 Discrepancies in PLE spectra of $Cs_2AgBiBr_6$ crystals and thin films

Lead-free double perovskites have up to now been evaluated as prototypes of photodetectors,[64], [135]–[137] light-emitting diodes,[138]–[140] solar cells,[141]–[145] and X-ray detectors.[88], [117], [146] An important development of such electronic devices was made by employing $Cs_2AgBiBr_6$, [17], [46] due to the easy applicability of this material as polycrystalline films or single crystals. [17], [88], [117], [135], [136], [141]–[144], [146] However, the physical properties of $Cs_2AgBiBr_6$ which are currently intensively discussed in the community, are not yet fully understood. For example, the optical properties have shown puzzling differences in UV-Vis absorption, PL and PLE between crystals and thin films.[69], [147], [148] Most prominently, the PLE spectra of $Cs_2AgBiBr_6$ crystals show a sharp increase at excitation energies around 2.4 eV when measured at 5 K, followed by a pronounced drop at 2.85 eV, which is assigned to a resonant excitation of direct band gap excitons.[65], [147] The difference between the absorption and PLE is explained by the emission of a color center located deep in the bandgap of $Cs_2AgBiBr_6$.[147] However, measurements on thin films revealed a different behavior: although a slight drop of the PLE signal at 2.8 eV has been observed by several groups, the signal is not quenched completely, in contrast to the behavior of single crystals.[69], [148] Furthermore, the sharp initial increase of the PLE signal was not observed in films. The rise of the signal is instead flattened and blue shifted when compared to the PLE of single crystals.

In the following sections, it will be shown, that the optical properties and particularly the PLE differ even for differently grown crystals. Although the reasons for the reported discrepancies are not yet fully understood, a possible key factor investigated in this section is the different structure and stoichiometry of thin films and crystals due to synthesis processes, which may lead to differences in the optical properties. When thin

films are processed, the precursor salts of $Cs_2AgBiBr_6$ are usually dissolved in dimethyl sulfoxide (DMSO) and annealed at rather high temperatures up to 285 °C after spin coating to evaporate the solvent and to form a polycrystalline film. [141], [142], [144] In contrast to that, crystals are synthesized differently. To be more precise so far crystals have been exclusively grown via an acid-based and controlled cooling crystallization technique. [17], [46], [88], [91], [136], [145], [149] When acids are used, the formation of crystals is promoted by slowly cooling the precursor solution, in contrast to the fast annealing process used for the crystallization of thin films.
In this section, an alternative method for growing $Cs_2AgBiBr_6$ crystals by slow evaporation is presented. In fact, growth by evaporation is a common and simple method to grow perovskite crystals.[83], [87], [150], [151] Importantly, the physical properties of the crystals grown by slow evaporation are more comparable to those of thin films. This can be attributed to the preparation conditions and crystallization mechanisms which are more similar to those being used in the synthesis of thin films.

5.1.2 Experimental methods to investigate structural and optical properties of $Cs_2AgBiBr_6$

Materials and solvents

DMF (99.8 %), DMSO (>99.9 %), cesium bromide (CsBr) (99.999 %, trace metals basis) were acquired from Sigma-Aldrich. Bismuth bromide ($BiBr_3$) (99.998 %, metals basis) and silver bromide (AgBr) (99.998 %, metals basis) were purchased from Alfa Aesar. HBr (48 wt%) was purchased from our in-house chemical supply of the Faculty of Chemistry and Pharmacy of the University of Würzburg. All chemicals were used as received and without further purification.

Solubility curves of $Cs_2AgBiBr_6$

CsBr (2 eq, 47.88 mg, 0.225 mmol), AgBr (1 eq, 21.12 mg, 0.1125 mmol) and $BiBr_3$ (1 eq, 50.48 mg, 0.1125 mmol) were weighed in stoichiometric amounts into a 4 ml glass vial in a nitrogen filled glovebox with a water and oxygen content below 1 ppm. The solubility curve for the acid-based process was achieved by adding small amounts of hydrobromic acid (HBr) (50 μl) every hour under constant stirring of the solution, until the precursor salts were completely dissolved. This was done for a temperature range from 25 °C to 100 °C, in order to obtain an exact solubility curve for $Cs_2AgBiBr_6$ in HBr. The error of this process was estimated to be 100 μl for each precursor solution.
The solubility curves of $Cs_2AgBiBr_6$ in DMF/DMSO (1 : 2) and pure DMSO were obtained in a similar way: CsBr (2 eq, 301.42 mg, 1.42 mmol), AgBr (1 eq, 132.98 mg,

0.071mmol) and $BiBr_3$ (1 eq, 317.75 mg, 0.071 mmol) were weighed in stoichiometric amounts in a nitrogen filled glovebox. By adding either a mixture of DMSO/DMF or pure DMSO under constant stirring, the solubility behavior was determined for different temperatures. Every hour, 50 μl of the corresponding solvent were added to the solutions, until the precursor salts were completely dissolved. The error of this process was estimated to be 10 g/l.

$Cs_2AgBiBr_6$ crystal growth and thin film synthesis

Crystal growth from controlled cooling In order to obtain $Cs_2AgBiBr_6$ crystals from HBr, the commonly known crystal growth protocol was followed. [17] A 0.3 molar solution of CsBr (2 eq, 319.21 mg, 1.5 mmol), AgBr (1 eq, 140.83 mg, 0.75 mmol), and $BiBr_3$ (1 eq, 336.52 mg, 0.75 mmol) was prepared with 10 ml of 48 wt% HBr. The solution was placed on a hotplate, in an oil bath, and heated to 110 °C for 2 h in order to obtain a completely dissolved precursor solution. To promote crystal growth, the solution was cooled down to room temperature (RT) at a rate of 1 °C/h. The crystals were then washed and dried with dichloromethane (DCM) in order to avoid any precursor precipitates remaining on the surface.

Crystal growth by slow evaporation A 1.5 molar stoichiometric solution of CsBr, $BiBr_3$ and AgBr was prepared by weighing 478.82 mg (2 eq, 2.25 mmol) of CsBr, 211.24 mg (1 eq, 1.125 mmol) of AgBr and 504.78 mg (1 eq, 1.125 mmol) of $BiBr_3$. The precursors were dissolved in 3 ml of a 2 : 1 DMSO/DMF mixture on a hotplate. After complete dissolution, the solution was filtered using a Poly(1,1,2,2-tetrafluoroethylene) (PTFE) filter with a pore size of 0.20 μm. The precursor solution was then placed at 146 °C on a hotplate for approximately 72 h until crystallization occurred. The resulting crystals were taken out of the solution and then washed with DCM to avoid any precursor precipitates on the surface.

Thin film synthesis Thin films were obtained using the protocol described in Sirtl et al. and were fabricated by Maximilian T. Sirtl from the group of Thomas Bein at LMU Munich.[144] A stoichiometric precursor solution was prepared by dissolving CsBr (212.8 mg, 1 mmol, Alfa Aesar 98.999 % metals basis), $BiBr_3$ (224.4 mg, 0.5 mmol, Alfa Aesar 99.9 % metals basis) and AgBr (93.9 mg, 0.5 mmol, Alfa Aesar 99.998 % metals basis) in 1 ml of DMSO. The solution was stirred at 130 °C until it was completely dissolved. Afterwards, the thin films were spin coated dynamically in a nitrogen filled glovebox (Step 1: 1000 rpm for 10 s, Step 2: 5000 rpm for 30 s). 7 s before the end of the second spin coat-

ing step, 400 μl of 2-propanol were dripped quickly onto the substrate. This procedure was followed by annealing the films for 5 min at 275 °C.

Characterization of the grown crystals and thin films

Characterization of stoichiometry and crystal structure XRF, XRD and EDX measurements were performed in order to characterize the obtained stoichiometry as well as the crystal structure of the samples. For EDX measurements, at least 4 working areas were measured. The obtained data was then normalized and averaged to obtain an average stoichiometry and elemental distribution over the whole crystal surface. EDX measurements were performed by Stephan Braxmeier at the ZAE Bayern.
For crystal structure analysis an orange block-like specimen of $Cs_2AgBiBr_6$, with approximate dimensions of 0.020 mm · 0.020 mm · 0.030 mm, was used for the X-ray crystallographic analysis. The X-ray intensity data were measured on a Bruker D8 Venture TXS system equipped with a multilayer mirror optics monochromator and a Mo K_α rotating-anode X-ray tube (λ =0.071 073 Å). The measurements were performed at room temperature (RT). The crystal structure analysis was performed in the group of Thomas Bein at the LMU Munich.

Optical characterization of the absorption tail PLE spectra were measured with a FLS980 spectrometer as described in subsection 4.3.3. All measurements were performed under ambient conditions. As the absorption coefficient is a thickness independent material property, the PLE spectrum must overlap with the absorption coefficient of the thin film in the energy range of 2.2 eV to 2.4 eV. The absorption coefficient for PLE measurements was therefore obtained by shifting the PLE spectra to the absorption coefficient of the thin film in the energy range of 2.2 eV to 2.4 eV. In this range, the shape of the PLE spectrum aligned perfectly with the shape of the calculated absorption coefficient of the thin film.
In order to further probe the optical absorption edge of the $Cs_2AgBiBr_6$ crystals, the transmission of the crystals was measured as described in subsection 4.3.2. An exemplary absorption coefficient for transmission and PLE, together with the measured penetration depths and measured energetic ranges for PLE and absorptance, are depicted in Figure 5.1.

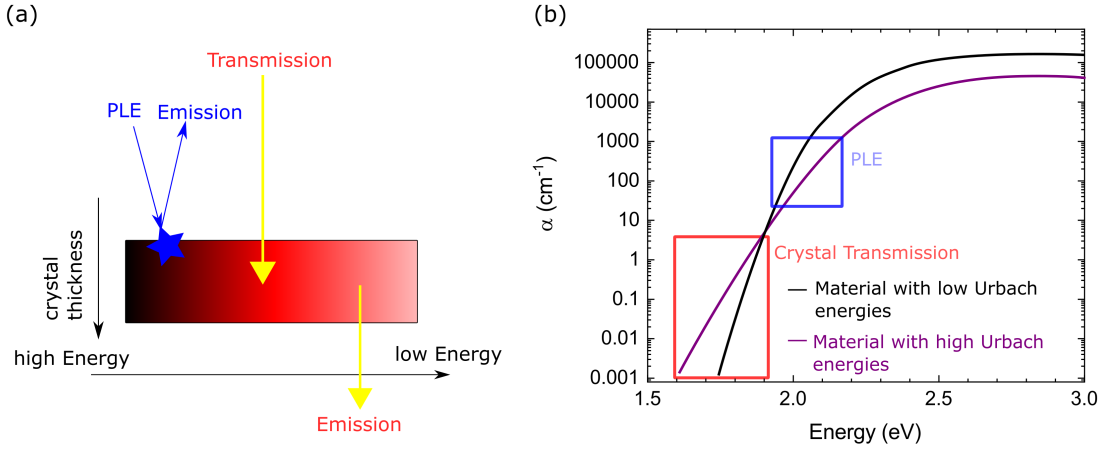

Figure 5.1: a) Probing depths for PLE and transmission measurements on the $Cs_2AgBiBr_6$ crystals. The blue arrows indicates that the PLE is only probing the surface of the crystals. Additionally, as PLE is only measured at energies higher than the PL emission, the absorption tail can only be probed at higher energies. The yellow arrows show that transmission can only be detected in the low energy region, as no light is transmitted by the crystal at higher energies due to a large absorption coefficient. b) Scheme of the absorption coefficient for materials with high (purple line) and low (black line) Urbach energies. The red and blue squares demonstrate the regions in which the absorption coefficient is probed by crystal transmission and PLE. Reproduced from [81] with permission from the Royal Society of Chemistry.

5.1.3 Solubility curve of $Cs_2AgBiBr_6$

In order to understand the crystallization of $Cs_2AgBiBr_6$ via evaporation and controlled cooling, solubility diagrams were prepared.[46] To ensure the correct stoichiometry of the precursor solution, the precursor salts CsBr (1 mmol), $BiBr_3$ (0.5 mmol) and AgBr (0.5 mmol) were dissolved either in a 2 : 1 mixture of DMSO and DMF, pure DMSO or HBr (48 wt%, boiling point (Bp)= 126 °C [152]). The colored curves in Figure 5.2 show the solubility of dissociated $Cs_2AgBiBr_6$ in different organic solvents as well as by dissolving bromine-containing salts in HBr. In Figure 5.2, an increase in solubility with rising temperature can be observed for all prepared solutions. The blue squares are consistent with the values reported in literature [88] and provide information about the ongoing crystallization process: slow cooling in steps of 1 °C/h of the hot saturated precursor solution slowly reduces the solubility of the perovskite. Finally, the solution supersaturates at a temperature of about 90 °C and crystal nuclei form spontaneously which, upon further cooling, form red crystals with defined facets and edges and a clearly visible octahedral shape as shown in the inset of Figure 5.2.

By comparing the red (DMSO/DMF) and violet (DMSO) solubility curves, it becomes clear that the perovskite is much more soluble in organic solvents than in aqueous acids. On average, the solubility of the perovskite in pure DMSO is nine times higher

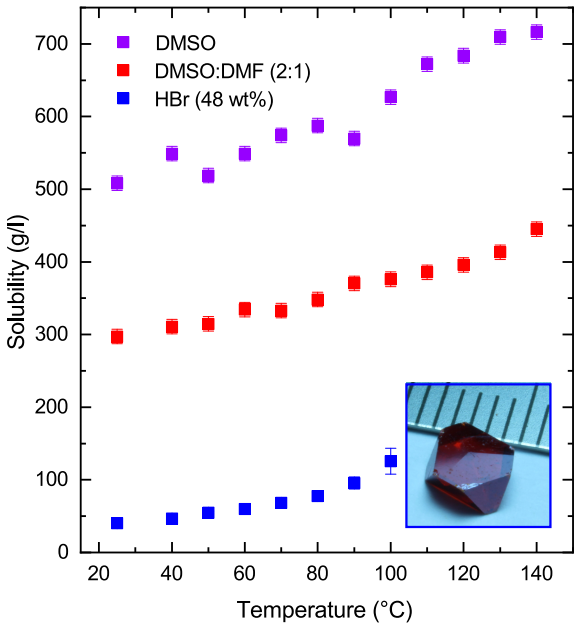

Figure 5.2: Solubility curves of $Cs_2AgBiBr_6$ in the organic solvent DMSO, the mixture DMSO:DMF and HBr (48 wt%). The inset displays an image of a crystal grown by controlled cooling. Reproduced from [81] with permission from the Royal Society of Chemistry.

than in HBr. Although the solubility in a mixture of DMSO and DMF is reduced by a factor of 1.7 compared to pure DMSO, these solvents seem to be inadequate to crystallize the double perovskites by controlled cooling due to the relatively high solubility of $Cs_2AgBiBr_6$ in these organic solvents. Moreover, one can exclude crystal growth by "inverse temperature crystallization" [85] since a decreasing solubility with increasing temperature would be required, which is clearly not the case here.[28], [86]
Despite the high solubility of $Cs_2AgBiBr_6$ in organic solvents, it is nevertheless possible to use these solvents to grow crystals in a controlled manner, e.g. by reducing the solubility of the perovskite via evaporating the precursor solution to obtain a supersaturated solution.

5.1.4 Crystal growth by evaporation and controlled cooling

To assess the crystallization process of the double perovskite in an organic solvent, $Cs_2AgBiBr_6$ in the DMSO:DMF blend was used as it has a lower solubility. This solvent mixture combines the advantages of a sufficient amount of the double perovskite being dissolved with the faster solvent evaporation. A faster solvent evaporation is expected due to the lower Bp of DMF (Bp = 153 °C)[153] compared to DMSO (Bp = 189 °C).
The precursor solutions were first filtered into a bottle using a syringe filter, which thereafter was placed on a hotplate with and without bottle cap as shown in Figure 5.3 for crystal growth by either controlled cooling or slow evaporation. In the initial phases

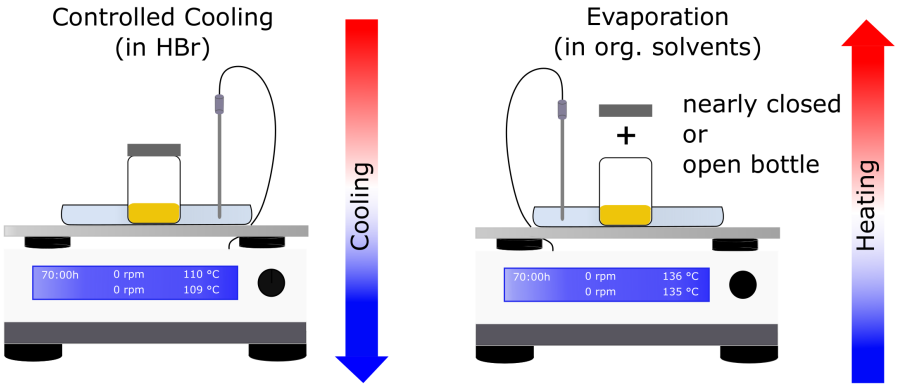

Figure 5.3: Schematic illustration of the crystallization techniques controlled cooling and (slow) evaporation for the growth of mm-sized $Cs_2AgBiBr_6$ crystals. Reproduced from [81] with permission from the Royal Society of Chemistry.

of crystal growth by slow evaporation, the yellow solution turns turbid over time as shown in Figure 5.4, and the crystalline side phases AgBr and cesium silver bromide ($CsAgBr_2$) are formed. As an example, the turbidity of the solution could be observed at 60 °C after approximately 2 h, followed by the formation of the sidephase for about another hour. For comparison, at even lower temperatures e.g. 40 °C, the solution turns turbid after 3 h followed by the formation of the sidephase 3 h later. This indicates that the process of crystal growth as well as sidephase formation strongly depend on the chosen growth temperature. Figure 5.5 shows the corresponding EDX and XRD patterns for crystals of the AgBr and $CsAgBr_2$ sidephases. Table 5.1 shows the corresponding stoichiometries determined by EDX of the corresponding sidephases. The powder XRD in Figure 5.5b proposes an orthorhombic crystal structure for $CsAgBr_2$ with lattice constants of a =20.05 Å, b =5.05 Å and c =6.01 Å, which is in good agreement with the values for the β-phase of $CsAgBr_2$ in literature.[154]

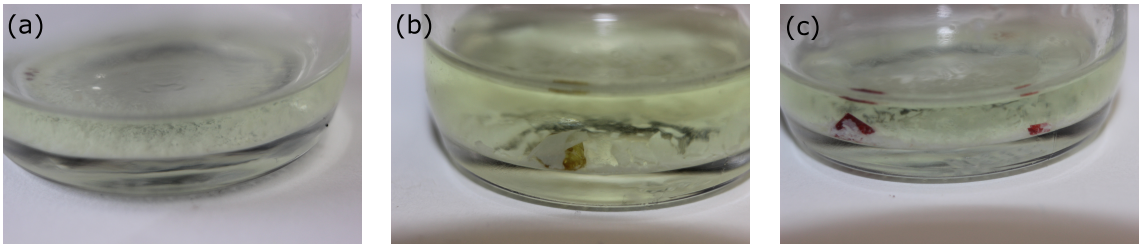

Figure 5.4: Formation of sidephases during crystal growth by slow evaporation. (a) The at first clear solution turns turbid over time when the sidephases $CsAgBr_2$ and AgBr are formed as shown in (b). (c) Growth of the $Cs_2AgBiBr_6$ crystal following the sidephase formation. Reproduced from [81] with permission from the Royal Society of Chemistry.

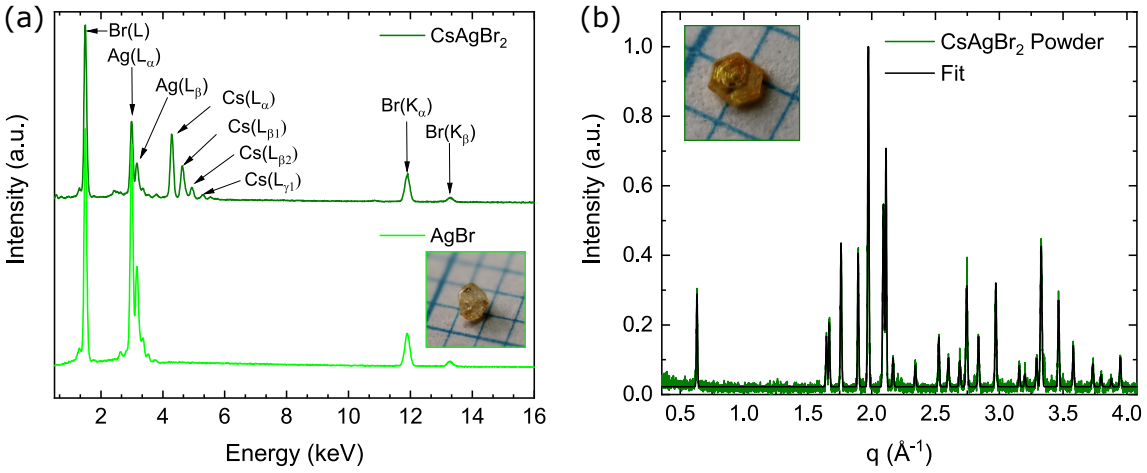

Figure 5.5: (a) EDX spectra of the sidephases AgBr and $CsAgBr_2$. (b) Powder XRD pattern of $CsAgBr_2$ with corresponding fit to evaluate the lattice constant. Reproduced from [81] with permission from the Royal Society of Chemistry.

Element	**AgBr**		**$CsAgBr_2$**	
	Expected atom fraction [%]	Experimental atom fraction [%]	Expected atom fraction [%]	Experimental atom fraction [%]
Cs	0	0.5	25	23.37
Ag	50	48.03	25	21.35
Br	50	51.47	50	54.48
Bi	0	0	0	0.80

Table 5.1: Theoretical stoichiometry and experimental data of the sidephases AgBr and $CsAgBr_2$. The exact determined stoichiometries by EDX were $Cs_{0.5}Ag_{48.03}Br_{51.47}$ and $Cs_{23.37}Ag_{21.35}Bi_{0.8}Br_{54.48}$. As only 0.5 at% of Cs were found in the $Cs_{0.5}Ag_{48.03}Br_{51.47}$ side phase, it is safe to assume that some Cs precursor salt can still be found on the AgBr crystals. Furthermore, the amount of Bi in the $Cs_{23.37}Ag_{21.35}Bi_{0.5}Br_{54.48}$ was below 1 at%. Hence, one can conclude that some Bi is found on the crystal surface, while the bulk of the yellow phase follows the stoichiometry of $CsAgBr_2$.

However, as time progressed, the white AgBr and yellow $CsAgBr_2$ polycrystals mostly dissolved again, and small $Cs_2AgBiBr_6$ crystals eventually formed on the bottom of the bottle. By increasing the growth temperature, the evaporation rate increased and a shorter growth period was found, as shown by the orange dots in Figure 5.6. As a consequence, many small crystals were formed in a short period of time, which is a clear indication of crystallization caused by evaporation. However, increasing the growth temperature also led to a strongly increased evaporation rate of the solvent when the bottle cap was slightly opened. Therefore, only polycrystals were formed. The evaporation rates and hence growth times for the crystals are depicted in Figure 5.6. By optimizing the extent of the bottle opening, it is possible to suppress the polycrystal growth so that mm-sized crystals can grow both at room temperature (RT) and at higher temperatures (146 °C). However, one should note that the slow evaporation method requires much more time, as the solvent can only escape slowly, thus preventing a faster decrease in solubility followed by crystallization. Nevertheless, very slow evaporation is an important prerequisite for high-quality crystal growth as will be shown below.

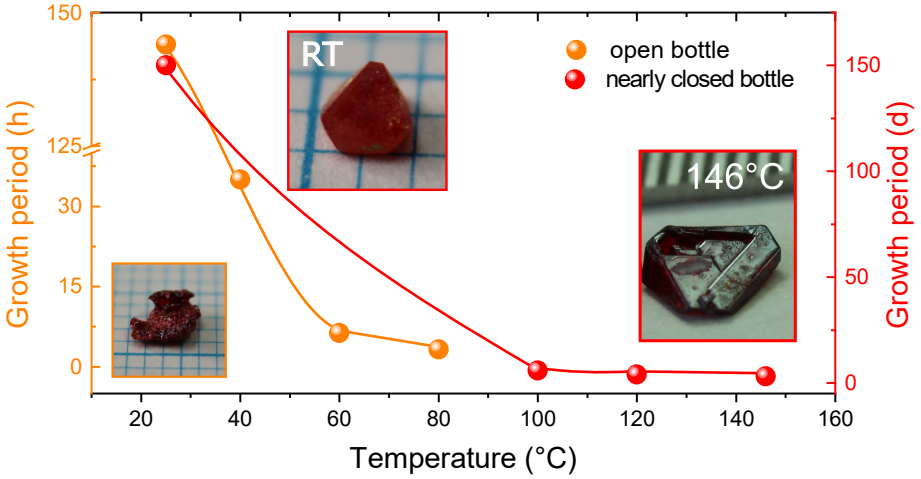

Figure 5.6: Growth period as a function of temperature to grow $Cs_2AgBiBr_6$ perovskite crystals by evporating the organic solvent. The insets show the corresponding crystals, whereby the color of the frame enables the assignment to the bottle opening during crystal growth. Reproduced from [81] with permission from the Royal Society of Chemistry.

5.1.5 Characterization of the crystal structure and crystal quality

The crystals grown by controlled cooling and evaporation were in a next step analyzed using XRF in order to detect the photon energies of the elements Cs, Ag, Bi and Br. For these measurements, the crystals were ground into a fine powder. Besides Br, Figure 5.7 clearly shows the $L_{\alpha 1}$, $L_{\beta 1}$ and $L_{\gamma 1}$ shell emission lines of Bi and the X-ray lines of Cs ($L_{\alpha 1}$; $L_{\beta 1}$).

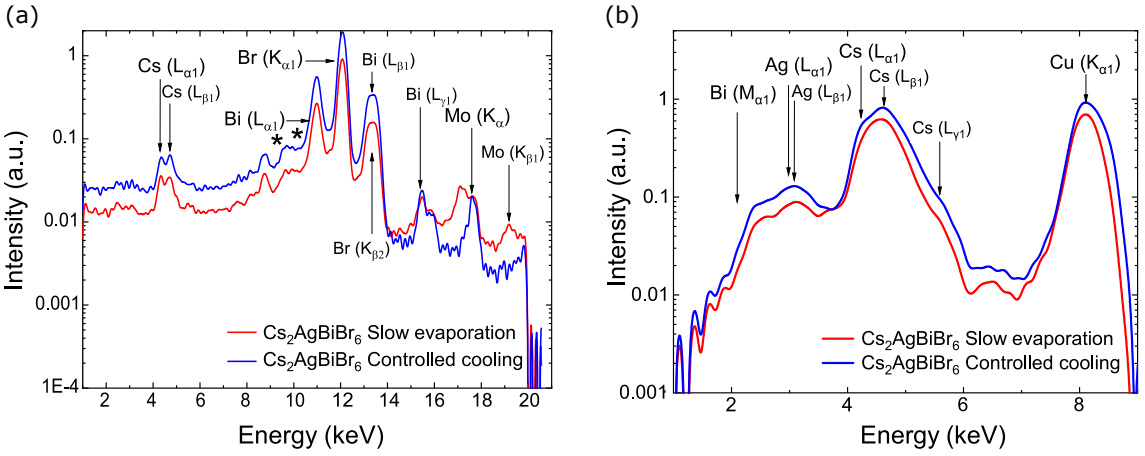

Figure 5.7: XRF spectra of the $Cs_2AgBiBr_6$ powder grown by slow evaporation (RT) and controlled cooling, evaluating the elements Cs, Ag, Bi, Br. a) XRF spectra recorded with a molybdenum radiation source. The asterisk marked peaks are caused by the sample holder. b) XRF spectra recorded with a copper radiation source. Reproduced from [81] with permission from the Royal Society of Chemistry.

The elements on the crystal surfaces were identified by energy dispersive X-ray (EDX) measurements. Besides the photon energies of Cs, Figure 5.8 shows the L-shell emission (L=1.49 keV) and the K-shell emission (K_α=11.89 keV; $K_{\beta 1}$=13.28 keV) of Br as well as the emission lines of Ag (L_α; L_β). Moreover, the XRF and EDX spectra of the crystals grown at different temperatures are almost identical, which indicates that the evaporation method is suitable for growing $Cs_2AgBiBr_6$ crystals. In addition, the EDX and XRF data suggest no difference for the crystals grown by slow and fast evaporation as shown in Figure 5.9.

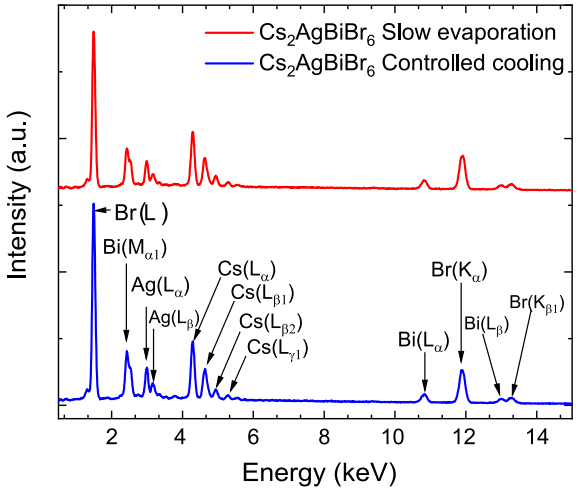

Figure 5.8: EDX measurements to detect the elements on the crystal's surface for crystals grown by controlled cooling and slow evaporation. Reproduced from [81] with permission from the Royal Society of Chemistry.

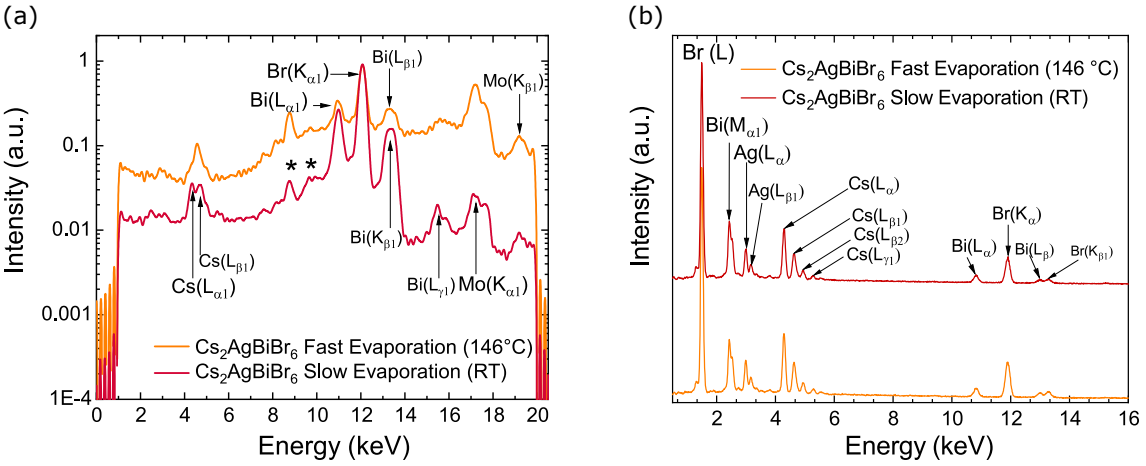

Figure 5.9: a) XRF spectra of the $Cs_2AgBiBr_6$ powders, obtained from crystals grown by fast evaporation 146 °C and slow evaporation (RT). The asterisk marked peaks are caused by the sample holder. (b) EDX spectra of $Cs_2AgBiBr_6$ crystals, grown by fast and slow evaporation, revealing the photon energies of the elements Cs, Ag, Bi and Br. Reproduced from [81] with permission from the Royal Society of Chemistry.

To confirm the correct stoichiometry of the crystals, the EDX data was evaluated quantitatively to obtain the atom fractions of the elements on the crystal surfaces. Table 5.2 shows a nearly perfect stoichiometry of $Cs_2AgBiBr_6$ for all growth methods. Additionally, inductively coupled plasma optical emission spectrometry (ICP-OES) and EDX measurements of the crystal powders also confirmed the stoichiometry determined with EDX measurements, as shown in Table 5.3 and Table 5.4.

After the correct stoichiometries of the grown crystals were ensured, the crystal structures were investigated for each growth technique. For this, XRD patterns of the crystal

Atom fraction [%]	**Theory**	**Controlled Cooling**	**Slow evaporation (RT)**	**Fast evaporation** (146 °C)
Cs	20	19.77	21.53	19.96
Ag	10	9.64	10.76	9.48
Bi	10	9.63	13.53	9.81
Br	60	60.96	54.18	60.74

Table 5.2: Quantitative analysis of the $Cs_2AgBiBr_6$ crystal surfaces by EDX

Atom fraction [%]	**Theory**	**Experimental**
Cs	20	19.9
Ag	10	10.0
Bi	10	10.0
Br	60	60.1

Table 5.3: Theoretical stoichiometry and experimental data of $Cs_2AgBiBr_6$ grown by controlled cooling, determined by ICP-MS, ICP-AES and ion chromatography. The measurements were performed at VOM Münster. A stoichiometry of $Cs_{19.9}Ag_{10.0}Bi_{10.0}Br_{60.1}$ was found.

powders were recorded which are shown in Figure 5.10. The fits of the obtained pow-

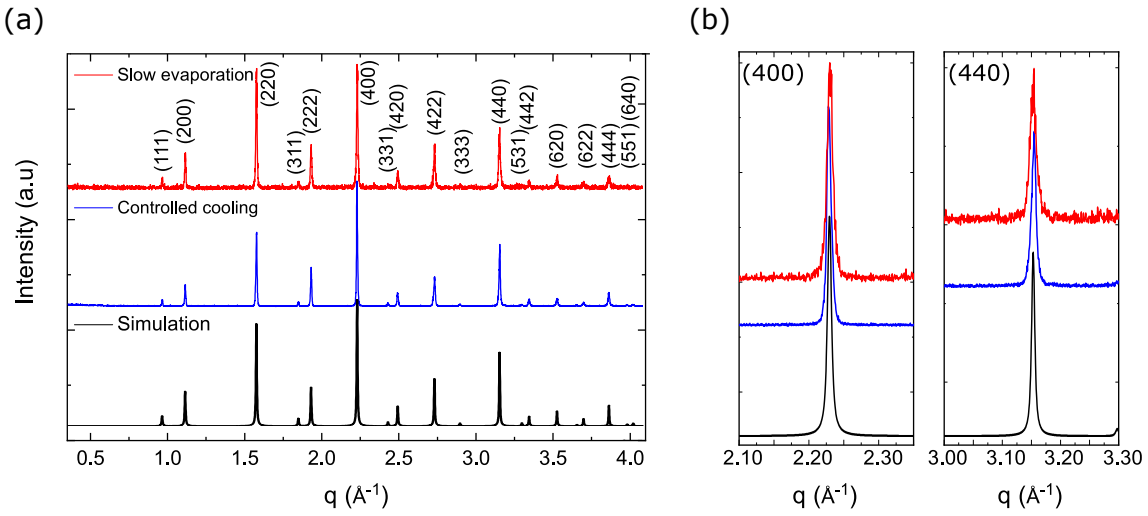

Figure 5.10: a) Powder XRD pattern of $Cs_2AgBiBr_6$ to compare the growth methods slow evaporation (RT) and controlled cooling with the simulation. The peaks are assigned to a simple cubic crystal structure. b) The (400) and (440) peaks of the powder patterns demonstrate no significant peak shift (same color coding as in a). Reproduced from [81] with permission from the Royal Society of Chemistry.

der patterns in Figure 5.11 enabled the assignment of the Miller indices and suggested a simple cubic (sc) crystal structure for all growth methods. Additionally, the lattice constants a of the grown crystals could be calculated to $a = (11.2704 \pm 0.0029)$Å for controlled cooling and $a = (11.2704 \pm 0.0017)$Å for fast evaporation. Those values are in good agreement with literature. [17], [18] However, for slow evaporation at low temperatures, a lattice constant of $a = (11.3187 \pm 0.0308)$Å was found. Although this is slightly

atom fraction [%]	**Theory**	**Controlled Cooling**	**Slow evaporation (RT)**	**Fast evaporation** (146 °C)
Cs	20	22.0	20.1	20.0
Ag	10	10.25	10.8	10.3
Bi	10	9.85	10.1	9.9
Br	60	57.9	59.0	59.8

Table 5.4: Theoretical stoichiometry and experimental data of $Cs_2AgBiBr_6$ grown by controlled cooling, slow evaporation and fast evaporation of crystal powders, determined by EDX.

larger than the lattice constant measured for fast evaporation and controlled cooling, it is still in good agreement with the expected values.[17], [18]

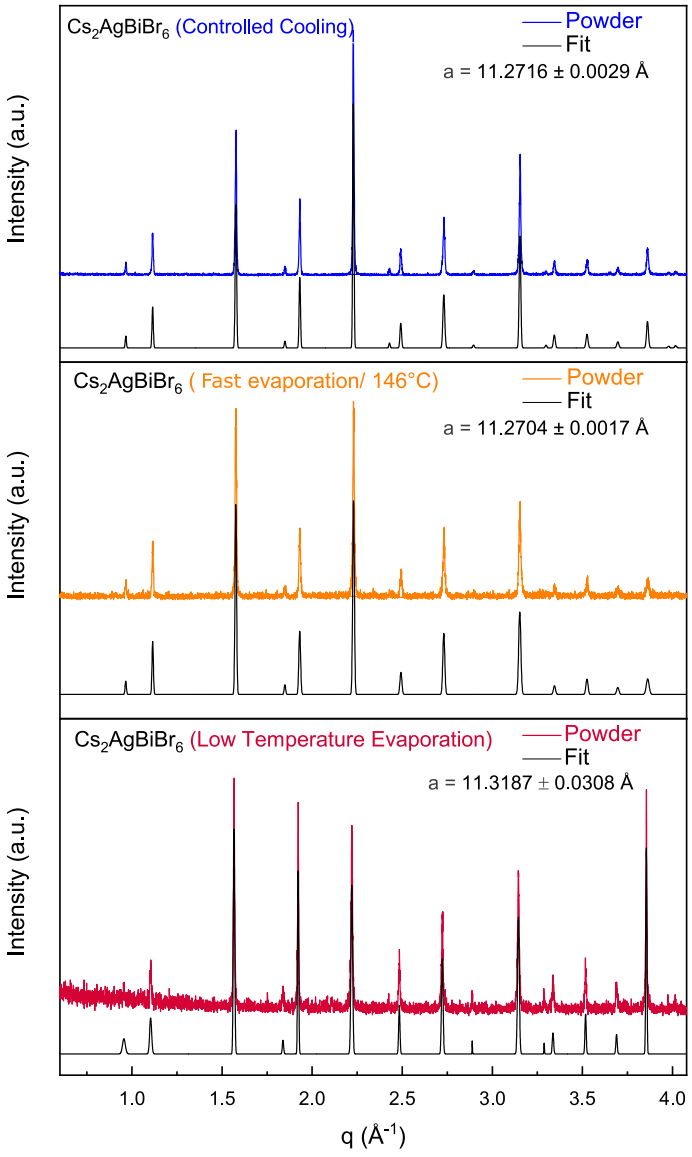

Figure 5.11: Powder XRD patterns of $Cs_2AgBiBr_6$, with corresponding fits to evaluate the lattice constant. Reproduced from [81] with permission from the Royal Society of Chemistry.

The theoretical powder pattern, which is also shown in Figure 5.10a, was obtained by crystal structure analysis measurements on a small $Cs_2AgBiBr_6$ single crystal. Like this, it was possible to confirm the lattice constants presented above. The detailed study confirms that $Cs_2AgBiBr_6$ crystallizes in the cubic $Fm\bar{3}m$ space group with the unit cell dimensions $a = b = c = 11.2727$Å and $\alpha = \beta = \gamma = 90\,°$. Moreover, the experimentally determined powder diffractograms and the simulations are almost identical. The perfect phase purity for both samples can also be seen from Figure 5.10b. The peaks of the (400) lattice planes and the (440) planes show no shift and hence confirm the success of the slow evaporation technique. In addition, the obtained XRD pattern of a polycrystalline $Cs_2AgBiBr_6$ thin film is in good agreement with the crystal powder pattern as shown in Figure 5.12. A further comparison of the two growth methods was per-

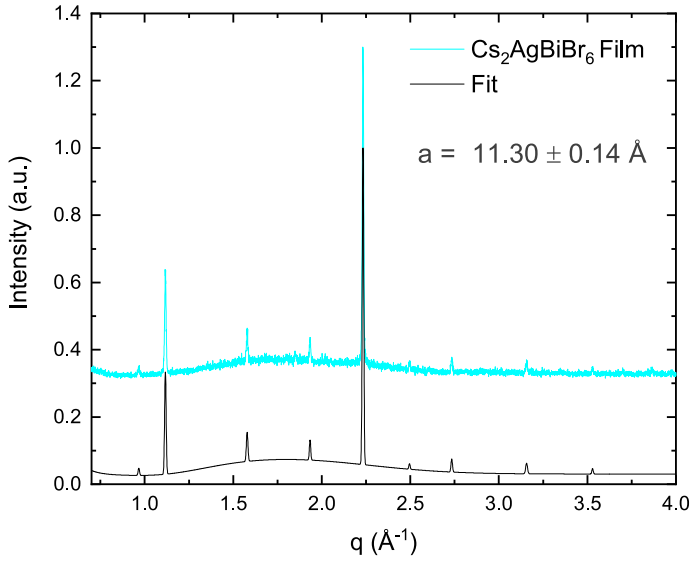

Figure 5.12: XRD measurement of a polycrystalline $Cs_2AgBiBr_6$ thin film with associated fit to evaluate the lattice constant. By fitting the reflections of the pattern, a simple cubic crystal structure for the film was found, which is in perfect agreement with the crystal powders as well. Reproduced from [81] with permission from the Royal Society of Chemistry.

formed by out-of-plane XRD measurements to verify the quality of the crystal surfaces, which are shown in Figure 5.13. The Bragg reflections of the acid-grown crystals reveal scattering along the [111] axis up to the 5th order.[136], [146] Besides the very sharp peaks of the {111} series, no other reflections are visible even on a logarithmic intensity scale, which is a clear indication of a single crystal surface. In addition, the rocking curve in Figure 5.14a of the (222) reflection only shows one single peak with a narrow FWHM of 0.015 ° for controlled cooling. This reveals a perfect crystal quality and proves the successful growth of $Cs_2AgBiBr_6$ single crystals with only one single domain. The XRD pattern of the crystal grown by slow evaporation also shows the {111} peak series

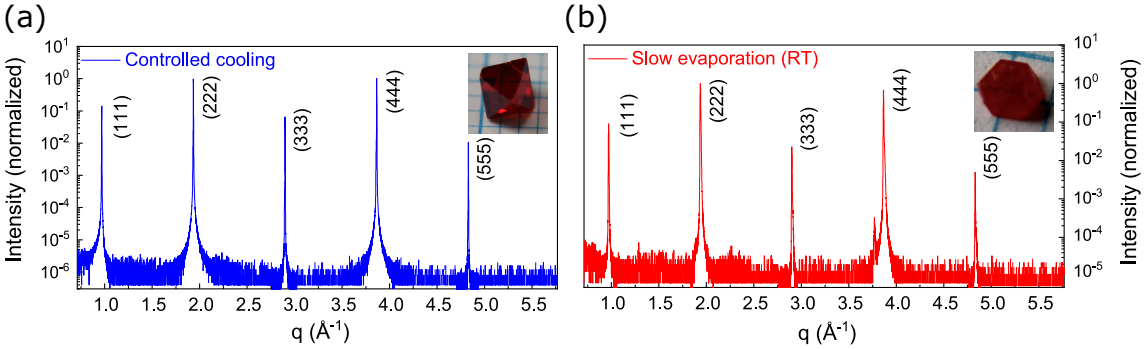

Figure 5.13: Out-of-plane XRD measurements of the crystals' surfaces revealing high crystal quality for a) controlled cooling and b) slow evaporation at RT. Reproduced from [81] with permission from the Royal Society of Chemistry.

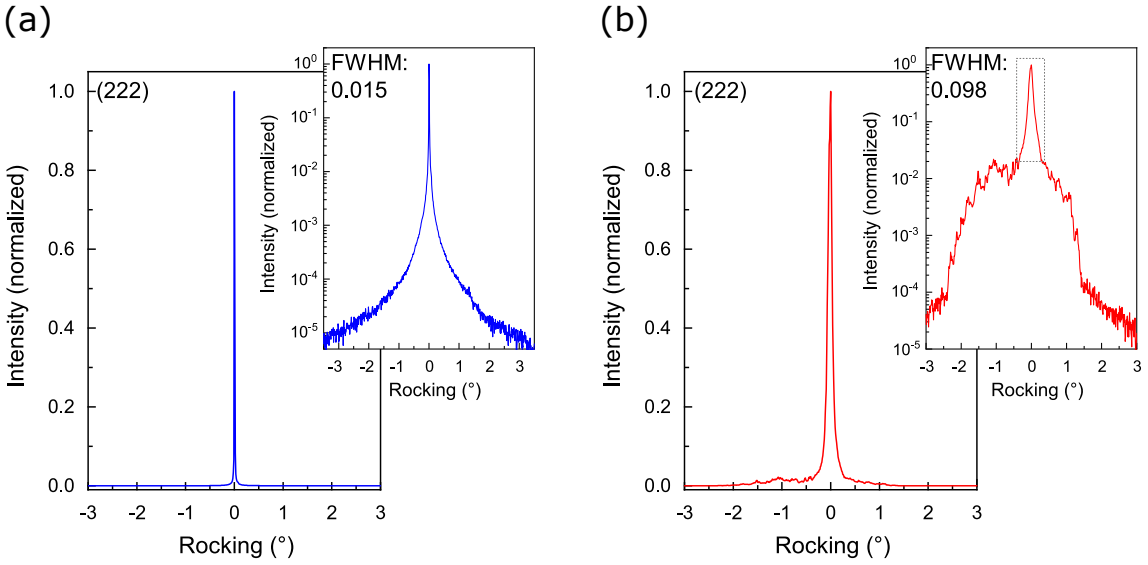

Figure 5.14: Rocking scan of the (222) reflection in linear and logarithmic scale performed on the crystal surfaces. a) Rocking scan of a crystal grown by controlled cooling. b) The rocking scan of the crystal grown at RT by slow evaporation shows a sharp peak in the linear plot but features small lattice defects, illustrated in the logarithmic plot. For the evaluation of the full width at half maximum, the peaks shown in the insets of a and b were used. Reproduced from [81] with permission from the Royal Society of Chemistry.

Growth Method	Controlled cooling		Slow evaporation
	this work	Literature	this work
Temperature	80 °C	70 °C- 110 °C[17], [155], [156]	20 °C-146 °C
Duration	92 h	52 h - 302 h[17], [155], [156]	6 months - 72 h
Solvent	HBr	HBr [17], [145], [155]	DMF/DMSO
Lattice constant	11.27 Å	11.25 Å -11.281 Å[17], [88], [155], [156]	11.32 Å
Lattice plane of top crystal surface	(111)	(111)[146], [155]	(111)
FWHM rocking scan	0.015 °	0.064 °-0.130 °[88], [155], [156]	0.098 °

Table 5.5: Overview of growth methods for $Cs_2AgBiBr_6$ crystals and their structural parameters.

that indicate a growth along this direction and therefore demonstrates a comparable surface quality to the crystals grown by the controlled cooling method. Although the rocking scan of the (222) peak is also of high quality, the logarithmic plot indicates that the crystallites are slightly tilted and offset from each other. This can be seen from the background in Figure 5.14b. Unfortunately, it was not possible to prove the crystal quality for the crystals grown at 146 °C due to their rough surface. Therefore, it is valid to assume that these crystals are generally of lower crystal quality caused by the fast evaporation and hot growth conditions of the crystals. In general, it can be concluded that the crystallographic quality of the $Cs_2AgBiBr_6$ crystals is strongly influenced by the chosen growth method.

When comparing the presented growth techniques of this section to those in literature, one finds that controlled cooling is the most prominent growth technique with growth temperatures between 70 °C and 110 °C, as shown in Table 5.5.[17], [155], [156] In comparison to controlled cooling, the growth duration of slow evaporation is significantly increased. However, the fact that crystals can be grown easily in a temperature range of 20 °C to 146 °C and without hydrobromic acid is a big advantage of slow evaporation. Additionally, the successful growth of $Cs_2AgBiBr_6$ crystals using the slow evaporation method is confirmed by the comparison of the lattice constants in Table 5.4.[17], [88], [156] The method even produces crystals with the same crystallographic plane of the crystal surface.[146], [155] By comparing the rocking scans, it becomes obvious that even the FWHM of the slow evaporation crystal is comparable to those in literature, [88], [155], [156] which is an indicator of the quality of the technique.

5.1.6 Optical properties and tailstates in $Cs_2AgBiBr_6$ crystals

Looking at the color of the grown crystals, clear distinctions can be seen. It was already shown in Figure 5.6 that the $Cs_2AgBiBr_6$ crystals grown by evaporation at 146 °C look significantly darker, compared to the crystals grown by controlled cooling or slow

evaporation at RT. This indicates that not only the crystal quality but also the optical properties of the crystals are affected by the growth method.
To prove that the growth conditions have an influence on the optical properties of the crystals, transmission studies were conducted in order to calculate the absorptance of the different crystals. The spectra depicted in Figure 5.15 show a drastic difference between the crystals grown by controlled cooling (blue) and by fast evaporation (red). In fact, the red curve reveals a broadened absorption edge, compared to the blue one. To quantify this difference between the two curves, the absorption tails were fitted with exponentials in order to determine the corresponding Urbach energies. This makes it possible to specify the degree of disorder and thus to evaluate the amount of tailstates in the crystal, as was explained in subsection 4.3.4.[91], [157]

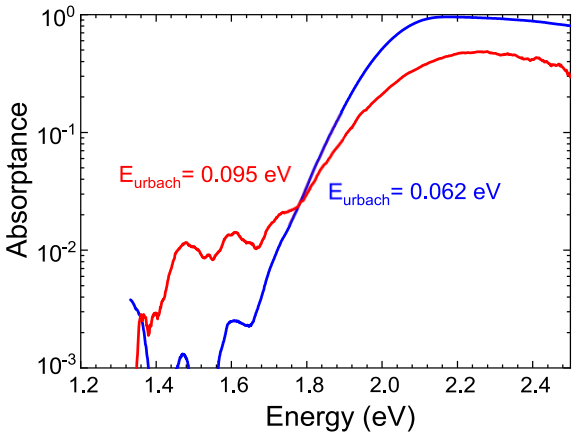

Figure 5.15: Absorptance of the crystals grown by controlled cooling (blue) and fast evaporation (red) at (146 °C) measured by crystal transmission. The Urbach energies reveal a higher amount of disorder for the crystals grown by evaporation. Reproduced from [81] with permission from the Royal Society of Chemistry.

It becomes clear that the crystals grown by fast evaporation exhibit a significantly higher Urbach energy of 95 meV than the crystals grown by controlled cooling (E_u =62 meV). The results strongly suggest a greater degree of structural disorder, related to either the stoichiometry of the double perovskites or to lattice defects (e.g. vacancies), for the crystals grown by fast evaporation. Similar observations were made for $MAPbI_3$ in [158], where a distinct relationship between low growth temperatures and high crystal quality was proposed.[158]
Furthermore, TRPL measurements in Figure 5.16 also suggest differences in the optical properties of the grown $Cs_2AgBiBr_6$ crystals. Very fast initial decays for the crystals grown by fast evaporation compared to crystals grown by slow evaporation and controlled cooling can be observed. Moreover, the PL lifetimes of crystals grown by slow evaporation and controlled cooling are increased compared to the PL lifetimes found

for crystals grown by fast evaporation at high temperatures. Those results hint towards a more pronounced trap assisted recombination when fast evaporation is used as a growth technique.

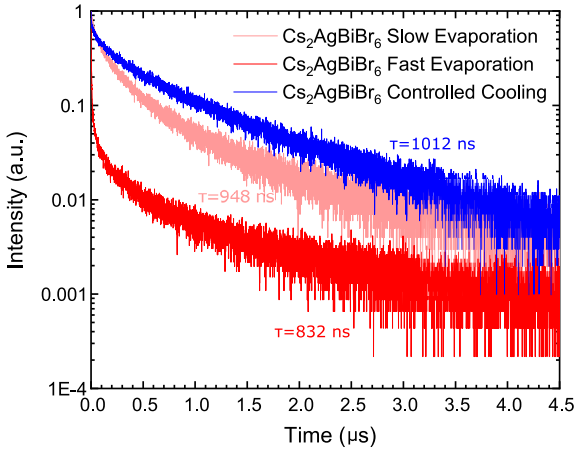

Figure 5.16: Transient photoluminescence measurement of $Cs_2AgBiBr_6$ crystals. A difference in the decay was found depending on the chosen growth method. Crystals grown by fast evaporation show a very fast initial decay compared to crystals grown by slow evaporation and controlled cooling. Furthermore, longer lifetimes are observed for crystals grown by controlled cooling. Reproduced from [81] with permission from the Royal Society of Chemistry.

To further assess the optical properties of the crystal surfaces and thin films with respect to absorption edge states, PLE spectroscopy was applied. Figure 5.17 shows the different PLE onsets for the crystals and for the thin film varying between 2.03 eV and 2.30 eV. Note that PLE monitors PL intensity at 1.9 eV over a wide range of excitation energies as described in subsection 4.3.3 and that the PL peak position (but not the intensity) is independent of the excitation wavelength. Therefore, the PLE spectra can be treated as a measure of absorption, as the rules of Vavilov and Kasha are fulfilled for $Cs_2AgBiBr_6$.[124], [125] Since the logarithm of PLE versus excitation energy in Figure 5.17 shows different slopes, one can assume a broader absorption edge for crystals grown by the evaporation technique and for the thin film, compared to the crystals grown by controlled cooling.

However, before the absorption onset of the crystal absorptance shown in Figure 5.15 and the PLE in Figure 5.17 can be directly compared, the probing depths of the two methods must be clarified. The absorptance of thick crystals only represents the absorption tail in a low-energy region (1.8 eV - 2.0 eV), as stated in subsection 4.3.3. There-

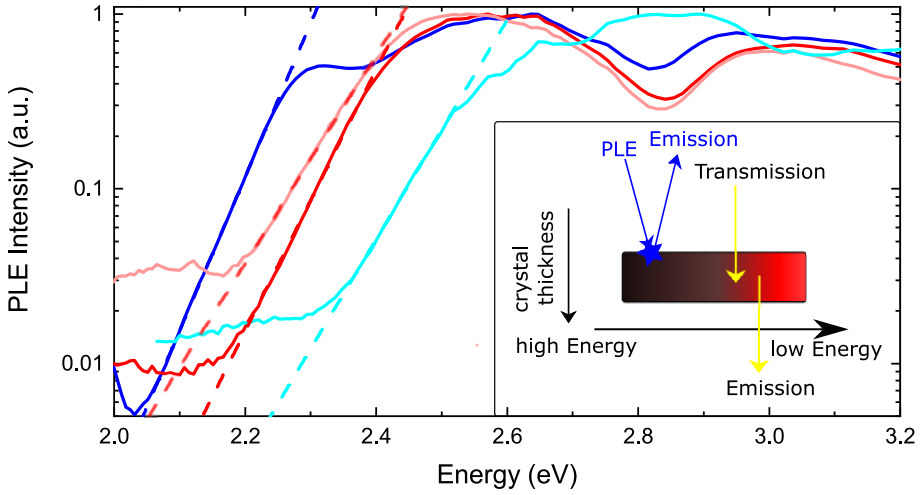

Figure 5.17: Photoluminescence excitation spectra for the crystals grown by controlled cooling (blue) and fast (red) and slow (light red) evaporation at different temperatures. The PLE is also shown for a thin film (turquoise). The different slopes of the absorption edge are indicated by dotted lines. Reproduced from [81] with permission from the Royal Society of Chemistry.

fore, the full spectrum of the absorption coefficient cannot be represented by only measuring the crystal transmittance according to

$$\alpha(E) = -\frac{\ln(T)}{d} \tag{5.1}$$

where d is the sample thickness and T is the transmittance. This has a simple reason: in the high energy range, well above the absorption edge, no light is transmitted by the crystal, due to its large thickness. In contrast, PLE examines the absorption at energies higher than the observed PL maximum, i.e. above 1.9 eV. Therefore, both measurement techniques probe the absorption tail in different energetic regions to extract the absorption coefficient in a broader energy range, as is schematically shown in the inset of Figure 5.17 and in Figure 5.1b. Figure 5.18 shows the resulting absorption coefficient for the different crystals and a thin film. Further information regarding the determination of α can be found in section 4.3 and in Figure 5.1. It becomes obvious that crystals grown by evaporation show a broadened absorption tail compared to crystals grown by controlled cooling. This again shows a greater degree of structural disorder in crystals grown by the evaporation growth method compared to crystals grown by controlled cooling. Remarkably, the absorption coefficient of the crystals grown by fast evaporation is similar to that of thin films in the spectral range of 2.2 eV to 2.4 eV shown in Figure 5.18. Therefore, one can conclude that tailstates still seem to be an issue to overcome in thin film preparation.

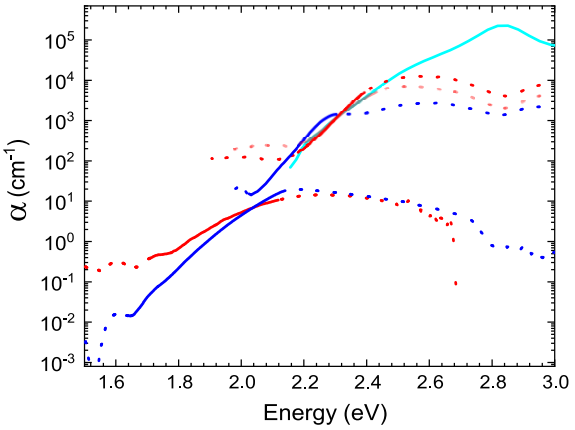

Figure 5.18: Derived absorption coefficient from absorptance and PLE measurements for the crystals and thin film. Dotted lines represent the neglected parts of the crystal absorptance and PLE spectra for the calculation of the absorption coefficient. The absorption coefficient for crystals grown by controlled cooling is depicted in blue, for crystals grown by fast evaporation in red, for slow evaporation the absorption coefficient is shown in light red whereas for a thin film it is shown in turquoise. Reproduced from [81] with permission from the Royal Society of Chemistry.

5.1.7 Conclusion

In this section, slow evaporation was presented as a new crystallization technique to grow $Cs_2AgBiBr_6$ crystals from organic solvents. This presents an alternative technique to the known controlled cooling method. Additionally, it could be shown that slow evaporation as growth technique possesses advantages to the commonly used controlled cooling method. While the acid based controlled cooling method is limited to one crystallization temperature, the evaporation process can be performed at both RT and high temperatures. Furthermore qualitative, quantitative and structural measurements provided clear evidence of the successful growth of the $Cs_2AgBiBr_6$ crystals via slow evaporation. When considering the out-of-plane XRD data, the crystals grown from controlled cooling exhibited an excellent single crystal quality. In addition, the crystals grown at RT by slow evaporation had a comparable quality, while only demonstrating small lattice imperfections. Hence, crystals grown by controlled cooling and the crystals grown at RT by slow evaporation are both suitable for building optoelectronic device prototypes. Additionally, it was shown in this section that different growth methods and particularly the high temperature evaporation growth, have a large impact on the optical properties of the $Cs_2AgBiBr_6$ crystals. Moreover, one can conclude that $Cs_2AgBiBr_6$ thin films resemble the lower quality of the crystals grown by fast evaporation at 146 °C and hence still possess a pronounced presence of optically detected tailstates.

Altogether, these results open a way to grow $Cs_2AgBiBr_6$ crystals which better repro-

duce and represent the optical properties of thin films and therefore possess the potential to help improve the quality and applicability of lead-free double perovskites in the future.

5.2 Influence of precursor stoichiometry on the optoelectronic properties of $Cs_2AgBiBr_6$ thin films

The following section is based on the paper "Optoelectronic Properties of $Cs_2AgBiBr_6$ Thin Films: The Influence of Precursor Stoichiometry" by Maximilian T. Sirtl, **Melina Armer**, Lennart K. Reb, Rik Hooijer, Patrick Dörflinger, Manuel A. Scheel, Kristofer Tvingstedt, Philipp Rieder, Nadja Glück, Pallavi Pandit, Stephan V. Roth, Peter Müller-Buschbaum, Vladimir Dyakonov and Thomas Bein, published in ACS Appl. Energy Mater. in 2020, volume 3, pages 11597-11609.

After the effects of crystallization temperature and growth method on the tailstates in $Cs_2AgBiBr_6$ were studied in the previous section, the following section will further elaborate on the influence of the precursor stoichiometry on the optoelectronic properties of $Cs_2AgBiBr_6$ and its impact on device efficiency. Here, the focus will be put on thin films, as stoichiometry changes have been shown to be an important parameter to optimize stability and efficiency of devices.[114], [159]–[161]

5.2.1 Application of $Cs_2AgBiBr_6$ as absorber layer in perovskite solar cells

Hybrid metal-halide perovskite solar cells have already reached efficiencies of 25.5 %. [41], [162], [163] However, as presented in section 2.1, their high toxicity and low long-term stability have raised concerns regarding their commercialization in the future.[12], [164]–[166]

Computational studies have put effort into finding new lead-free materials but also revealed additional issues such as thermodynamic stability, solubility in suitable solvents and suitable optoelectronic properties for the application of those materials in solar cells.[118], [167]–[172] When $Cs_2AgBiBr_6$ was proposed as lead-free double perovskite, the favorable optoelectronic properties and their high stability toward ambient conditions quickly suggested promising results for their application in photovoltaic devices, in spite of their large bandgap.[17], [68], [142], [173]–[175]

Up to now, several solar cell designs have been demonstrated with $Cs_2AgBiBr_6$ now reaching power conversion efficiencies of up to 4.23 % when organic dyes are used as an additional layer in the devices.[71] Moreover, different fabrication methods for the $Cs_2AgBiBr_6$ absorber layer have been developed, ranging from vapor-assisted annealing to vapor deposition.[71], [114], [141], [143], [176]

As already established in the previous section, crystallinity, crystal orientation and qual-

ity are essential parameters if efficient solar cells are to be fabricated.[81], [177]–[183] Therefore, a capillary-assisted dip-coating method was developed.[184] With that, it was possible to achieve crystalline $Cs_2AgBiBr_6$ films at 160 °C with a preferred orientation parallel to the (002) plane.[184] Additionally, it was shown that the optoelectronic properties of $Cs_2AgBiBr_6$ thin films are improved if the stoichiometry of the perovskite is kept as exact as possible.[114]
In this section, the influence of the precursor stoichiometry on the properties of $Cs_2AgBiBr_6$ is investigated. To do that, the amount of AgBr and $BiBr_3$ which was added to the stock solution, was varied systematically. By using a combination of AgBr excess with a $BiBr_3$ deficiency, a significant increase in the orientation and crystallinity of the thin films could be observed. Optoelectronic properties of the thin films were studied by means of time-resolved microwave conductivity (TRMC), trPL, PLQY as well as fluence dependent PL.
Thus, this section provides a simple way to investigate the properties of $Cs_2AgBiBr_6$ using a two-step spin-coating process in order to improve the efficiency of $Cs_2AgBiBr_6$ solar cells. Additionally, an easy way to increase the orientation and hence optimize the optoelectronic properties and power conversion efficiencies of $Cs_2AgBiBr_6$ solar cells is proposed.

5.2.2 Experimental methods to characterize the $Cs_2AgBiBr_6$ thin films and solar cells

Materials and thin film synthesis

The precursor solution was prepared by dissolving CsBr (212.8 mg, 1 mmol, Alfa Aesar, 99.999 % metals basis), $BiBr_3$ (224.4 mg, 0.5 mmol, Alfa Aesar, 99.9 % metals basis) and AgBr (93.9 mg, 0.5 mmol, Alfa Aesar, 99.998 % metals basis) in 1 ml of DMSO (Sigma Aldrich, anhydrous, ≥ 99.9 %) at 130 °C to obtain a 0.5 M solution for the stoichiometric reference films. In order to change the stoichiometry, the amounts of AgBr and $BiBr_3$ were altered as described in Table 5.6. The films were then deposited by dynamically spin-coating (1000 rpm for 10 s followed by 5000 rpm for 30 s) 80 μl onto the substrate. After 33 s, 400 μl of 2-propanol were dripped on top of the substrates, followed by annealing the thin films at 275 °C for 5 min.

Solar cell fabrication

Fluorine-doped tin oxide (FTO) coated glass sheets (7 Ω/sq) were patterned by etching with zinc-powder and 3 M HCl, cleaned with a detergent, followed by washing with acetone and ethanol and dried under an air stream. Directly before applying the hole

Film stoichiometry	AgBr [mg]	$BiBr_3$ [mg]	CsBr [mg]
1 : 1.15	93.9	258.0	212.8
1 : 0.85	93.9	190.7	212.8
1.15 : 1	108.0	224.4	212.8
1.15 : 0.85	108.0	190.7	212.8

Table 5.6: Stoichiometric changes of the $Cs_2AgBiBr_6$ precursor solution and the weighed in ratios of AgBr:$BiBr_3$ investigated in this chapter.

blocking layer, the substrates were plasma-cleaned with oxygen for 5 min. A compact TiO_2 layer was prepared from a sol-gel precursor solution by spin-coating 300 μl onto the 3 cm·3 cm substrates for 45 s at 2000 rpm and calcination afterwards at 500 °C for 30 min in air, resulting in a 50 nm thick layer. For the sol-gel solution, 2 M HCl (35 μl) in 2.53 ml of dry 2-propanol were added dropwise to a solution of 370 μl titanium isopropoxide in 2.53 ml dry 2-propanol under vigorous stirring. After cooling down, the substrates were again plasma-cleaned for 5 min and transferred to a nitrogen-filled glovebox. On top of the titania layer, the active layer was deposited as described above. For P3HT, 55 mg of the material (Ossila, batch M1011; MW: 60150; RR: 97.6 %, Mn: 28650; PDI: 2.1) was dissolved in 1 mL of ortho-dichlorobenzene and deposited dynamically by spin-coating 90 μl of a 55 mg/ml solution at 600 rpm for 120 s at ambient conditions. The top electrode with a thickness of 40 nm was deposited subsequently by thermal evaporation of gold under vacuum (ca. 10^{-6}mbar).

Materials characterization

X-ray Diffraction The XRD data on thin films was recorded using a Bruker D8 Discover diffractometer with Ni-filtered Cu K_α radiation and a DECTRIS solid-state strip detector MYTHEN 1K in Debye-Scherrer geometry. The XRD measurements were performed in the group of Thomas Bein at LMU Munich.

Scanning Electron Microscopy (SEM) SEM images were obtained with a FEI Helios G3 UC instrument with an acceleration voltage of 5 kV for the cross-sectional images and 2 kV for the top-view images and EDX studies. All samples were sputtered with carbon beforehand, and both mirror and through the lens detectors were used. The SEM measurements were performed by Dr. Steffen Schmidt at LMU Munich.

Steady-State Photoluminescence and Time Correlated Single Photon Counting The thin films were deposited onto the respective substrate by spin-coating as described above and PL measurements were performed in air with a FluoTime 300 spectrofluorometer from PicoQuant GmbH.

To excite the samples for steady-state measurements, a pulsed solid-state laser of 375 nm wavelength (LDH375 Pico Quant) with a fluence of 20 pJ/cm^2 at 40 MHz repetition rate was used in order to obtain steady-state conditions.
For TCSPC measurements, the samples were excited using a pulsed solid-state laser of 375 nm (LDH375, PicoQuant) with the following power and repetition rates: AgBr:$BiBr_3$ =1:1.15 (4.1 μW; 0.25 MHz), 1:0.85 (3.8 μW; 0.23 MHz), 1.15:1 (4.9 μW; 0.29 MHz), 1.10:0.90 (4.2 μW; 0.26 MHz), 1.15:0.85 (3.8 μW; 0.23 MHz), 1.20:0.80 (4.6 μW; 0.28 MHz). The illuminated area was 100 μm·100 μm.
The emission of the sample was collimated, focused on the entrance slit of the monochromator and attenuated with a neutral density filter such that the photomultiplier tube (PMT) could only detect one single photon at a time. The time difference between laser triggering and detection of a photon was measured and collected in a histogram. After a sufficiently large number of counts, the decay of the charge carrier dynamics could be obtained. The TCSPC and steady-state PL measurements were conducted by Maximilian T. Sirtl from the group of Thomas Bein, while fluence-dependent measurements were performed in Würzburg.
Fluence-dependent TCSPC measurements were carried out with an FLS980 Edinburgh Instruments spectrometer as described in section 4.1. As an excitation source, a pulsed 375 nm laser (EPL-375) with a repetition rate of 0.2 kHz was used for all samples. The excitation fluence was varied between 9.2 nJ/cm^2 and 0.5 nJ/cm^2 by the use of neutral density filters.
Fluence-dependent steady-state PL was measured with the setup described in section 4.1.

Time-Resolved Microwave Conductivity Measurements The stoichiometrically altered $Cs_2AgBiBr_6$ thin films were fabricated on sapphire substrates by spin-coating. The films were placed in a microwave cavity and the change in reflected microwave power at 9 GHz was measured after pulsed excitation (1 kHz) with a wavelength of 355 nm. The films were illuminated from the backside. TRMC experiments were conducted by Patrick Dörflinger from the Dyakonov group in Würzburg.

Absorption Measurements The linear absorption spectra of the thin films were recorded using a Lambda 950 PerkinElmer UV-Vis spectrometer with an integrating sphere. The measurements were performed at ZAE Bayern with assistance of Clara Scheuring.

Solar Cell Charaterization The solar cells were characterized by Maximilian T. Sirtl in the group of Thomas Bein at LMU Munich. Current-voltage (J-V) characteristics of the perovskite solar cells were measured using a Newport OrielSol 2A solar simulator with a Keithley 2401 source meter. The devices were illuminated through a shadow mask, yielding an active area of 0.083 cm^2. The J-V curves were recorded under standard AM 1.5 G illumination from a xenon lamp and calibrated to a light intensity of 100 mW/cm^2 with a Fraunhofer ISE certified silicon diode. The input bias voltage was scanned from −1.5 V to 0 V in steps of 0.05 V with a rate of 0.2 V/s. All prepared devices show a comparable degree of hysteresis between the forward and the reverse scan, which is negligibly small.
To obtain the EQE spectra, the respective solar cell was illuminated with chopped monochromatic light of a tungsten light source. The resulting current response was recorded via a lock-in amplifier (Signal Recovery 7265) at a chopping frequency of 14 Hz. The current response of a reference diode was used to obtain the incident light power in order to calculate EQE(λ). By integrating the resulting EQE curve over the reference solar spectral irradiance (global tilt, American Society for Testing and Materials, ASTM G173), the theoretical short circuit current under one sun condition was extracted. Philipp Rieder from the Dyakonov group assisted with EQE measurements and evaluation.

5.2.3 Thin film processing and antisolvent screening

For thin film preparation, CsBr, AgBr and $BiBr_3$ were dissolved in DMSO at a temperature of 130 °C in order to obtain a 0.5 M solution. The solution was then spin-coated on the substrates followed by an annealing step at 275 °C for 5 min as shown in Figure 5.19. However, for the preparation of the $Cs_2AgBiBr_6$ thin films, a variety of different antisolvents were screened to find the optimal processing conditions for perfect surface coverage and grain size. As a result, the best film coverage and morphology was obtained using 2-propanol (IPA) and working in a nitrogen-filled glovebox. IPA has also been previously reported to be a good antisolvent for the preparation of $Cs_2AgBiBr_6$ thin films.[114], [143]
Moreover, SEM analysis of the double perovskite thin films revealed that IPA as antisolvent results in the best film morphology and complete film coverage as shown in Figure 5.20. In consequence, IPA is used as antisolvent for all thin films presented in this section. Table 5.7 lists the stoichiometric variations used in the precursor solutions for the fabrication of thin films to investigate the influence of stoichiometry variations on the optoelectronic properties of $Cs_2AgBiBr_6$.
In general, phase purity and high crystallinity are essential parameters for the per-

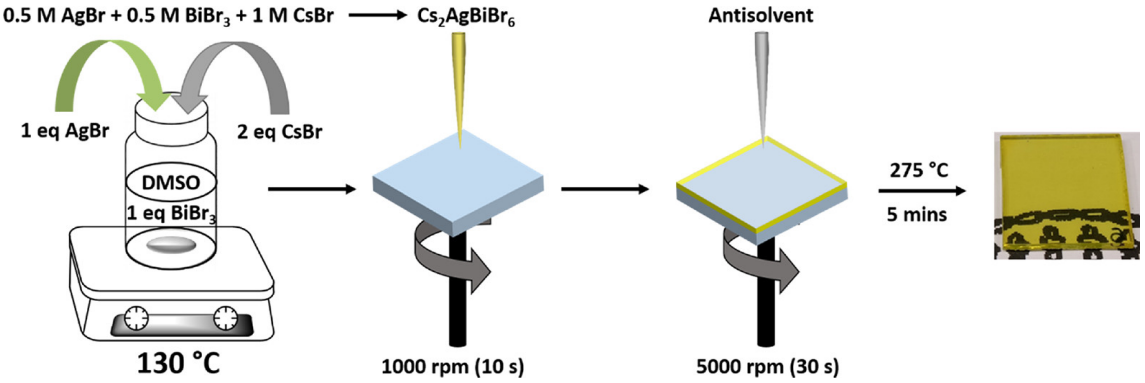

Figure 5.19: Synthesis protocol for the $Cs_2AgBiBr_6$ thin films. In a first step, the precursors were dissolved in DMSO at 130 °C and, in a second step, the solution is spin-coated in a two-step antisolvent process. The phase-pure double perovskite films were obtained after an additional annealing step at 275 °C for 5 min. Reprinted with permission from [144]. Copyright 2020 American Chemical Society.

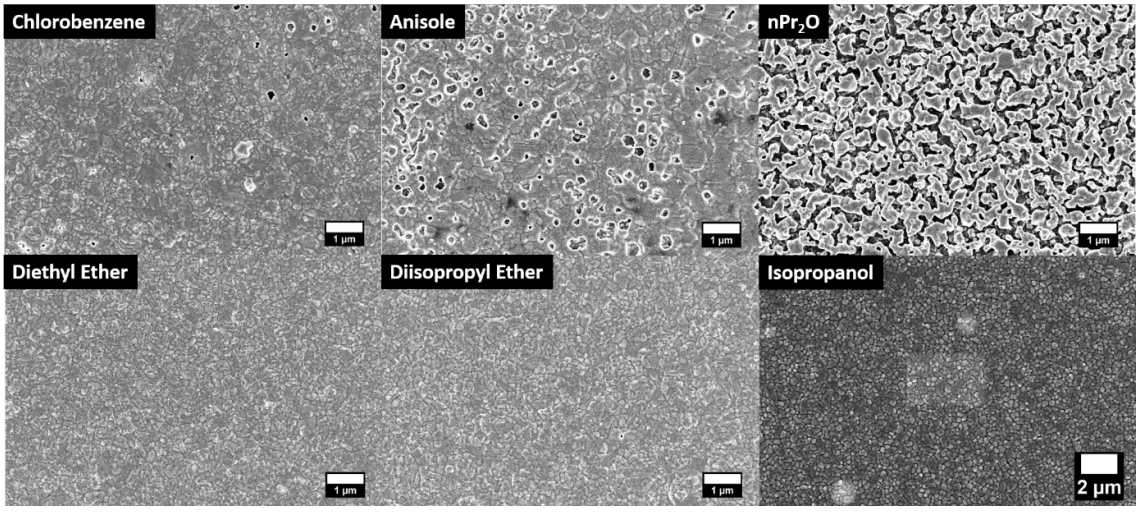

Figure 5.20: SEM images of the $Cs_2AgBiBr_6$ film surface for different antisolvents, showing the best surface coverage when IPA is used as antisolvent. Reprinted with permission from [144]. Copyright 2020 American Chemical Society.

formance of double perovskite films when used as absorbers in solar cells.[91], [114], [141]–[143], [176], [185] However, in the case of phase purity it has been shown for lead-based perovskites that a small PbI_2 excess can be beneficial for the performance of solar cells and the trap densities in the device.[186]–[188]. Therefore, the influence of stoichiometry on the crystallization and orientation of the $Cs_2AgBiBr_6$ thin film was studied as a first step and the results presented in the following.

AgBr	**$BiBr_3$**	**CsBr**	**abbreviation**
−10%	1	1	0.90 : 1
+10%	1	1	1.10 : 1
1	+10%	1	1 : 1.10
1	−10%	1	1 : 0.90
+10%	+10%	1	1.10 : 1.10
+10%	−10%	1	1.10 : 0.90
−15%	1	1	0.85 : 1
+15%	1	1	1.15 : 1
1	−15%	1	1 : 0.85
1	+15%	1	1 : 1.15
+15%	−15%	1	1.15 : 0.85
−15%	+15%	1	0.85 : 1.15
+15%	+15%	1	1.15 : 1.15
−20%	1	1	0.80 : 1
+20%	1	1	1.20 : 1
1	−20%	1	1 : 0.80
1	+20%	1	1 : 1.20
+20%	−20%	1	1.20 : 0.80
−20%	+20%	1	0.80 : 1.20
+20%	+20%	1	1.20 : 1.20

Table 5.7: Concentration changes of the precursor solution

5.2.4 Crystallization and thin film orientation

In order to achieve crystallization conditions similar to a solar cell device, the perovskite layer was spin-coated on top of a compact TiO_2 layer on a FTO substrate. The resulting films were then investigated using XRD as shown in the diffractograms in Figure 5.21. The XRD patterns show that changing from Bi^{3+}-rich and/or Ag^{+}-poor conditions to Ag^{+}-rich and Bi^{3+}-poor conditions strongly increases the crystallinity and the orientations of the crystallites in the film. However, small amounts of a side phase can be found in the powder XRD patterns of the films, which will be identified and discussed at a later point.

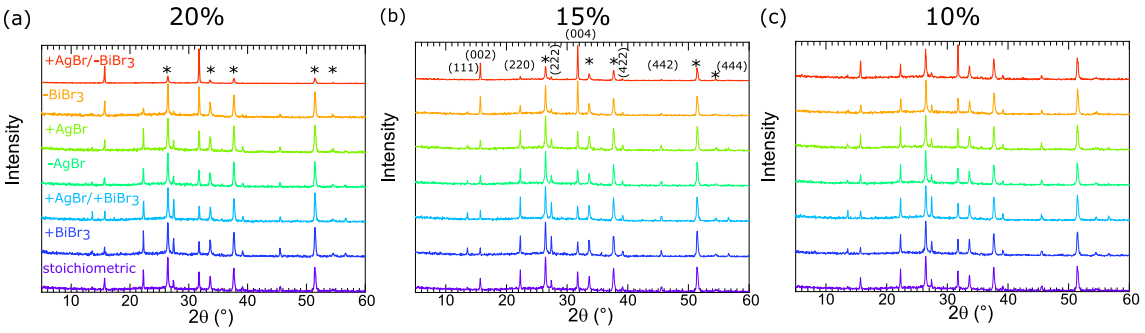

Figure 5.21: XRD patterns of $Cs_2AgBiBr_6$ thin films obtained by changing the precursor ratio by a) 20 %, b) 15 % and c) 10 %. The impact of crystallinity is visible by comparing the (002) and (004) peak intensities with respect to the FTO peak (marked with asterisks). Reprinted with permission from [144]. Copyright 2020 American Chemical Society.

As all prepared films have approximately the same thickness of 150 nm, the increasing peak ratio of the perovskite and the FTO peaks in the XRD patterns indicate an increased crystallinity. Additionally, it becomes clear that the crystallinity drastically changes for Bi-deficient films as well as for a Bi deficiency combined with an Ag excess. Furthermore, an increase of the crystallite orientation within the film is indicated by lacking (111) and (022) peaks from the stoichiometric reference in the XRD patterns. Only the Bragg peaks of the (002) and (004) planes can be found in the XRD pattern for 20 mol% Ag excess with a simultaneous Bi deficiency. Figure 5.21a therefore displays the effect of changes in the stoichiometry by 20 mol% as this variation seems to mostly affect the crystallinity and orientation of the films. However, a smaller impact on stoichiometric changes was found for films with 15 mol% and 10 mol%, which is shown in Figure 5.21b and c.

For further comparison, Figure 5.22 shows the XRD patterns of films with only $BiBr_3$ excess, pure $BiBr_3$ deficiency, the combination of $BiBr_3$ excess and AgBr deficiency, as well as pure AgBr excess for the different concentrations. In Figure 5.22a, a clear indication can be seen that the orientation and the crystallinity of the films are strongly influenced by the amount of $BiBr_3$ in the precursor solution. Figure 5.22a shows that the crystal orientation of the films remains similar as the number of visible peaks in the XRD pattern does not change. However, the peak intensities of the (111) and the (022) direction are increased compared to films with a concentration of 15 mol%. Additionally, the peak intensities are decreasing again for a concentration of 20 mol%.

For stoichiometries of $1:(1-x)$, the XRD patterns in Figure 5.22b exhibit a decrease of the Bragg peak intensities of the (111) and (022) planes and hence hints towards an increased orientation of these films. Furthermore, the effect of increasing crystallite orientation can be improved by using an additional AgBr excess and hence a stoichiometry of $(1+x):(1-x)$. The XRD patterns for the $(1+x):(1-x)$ stoichiometry reveal only

the (002) and (004) planes as can be seen from Figure 5.22c. In addition, an increase in crystallinity could be observed, as the peak ratio of the (002) and (004) planes relative to the FTO peaks increases significantly. The higher crystallinity is also indicated by a decrease of the FWHM of the (004) direction at 31.8 ° going from 0.21 ° for the stoichiometric reference to 0.16 ° for the $(1+x)$:$(1-x)$ film. However, if just pure AgBr was used, no impact on the crystal orientation could be found as shown in Figure 5.22d. To further asses the phase purity of the $Cs_2AgBiBr_6$ thin films, powder XRD measure-

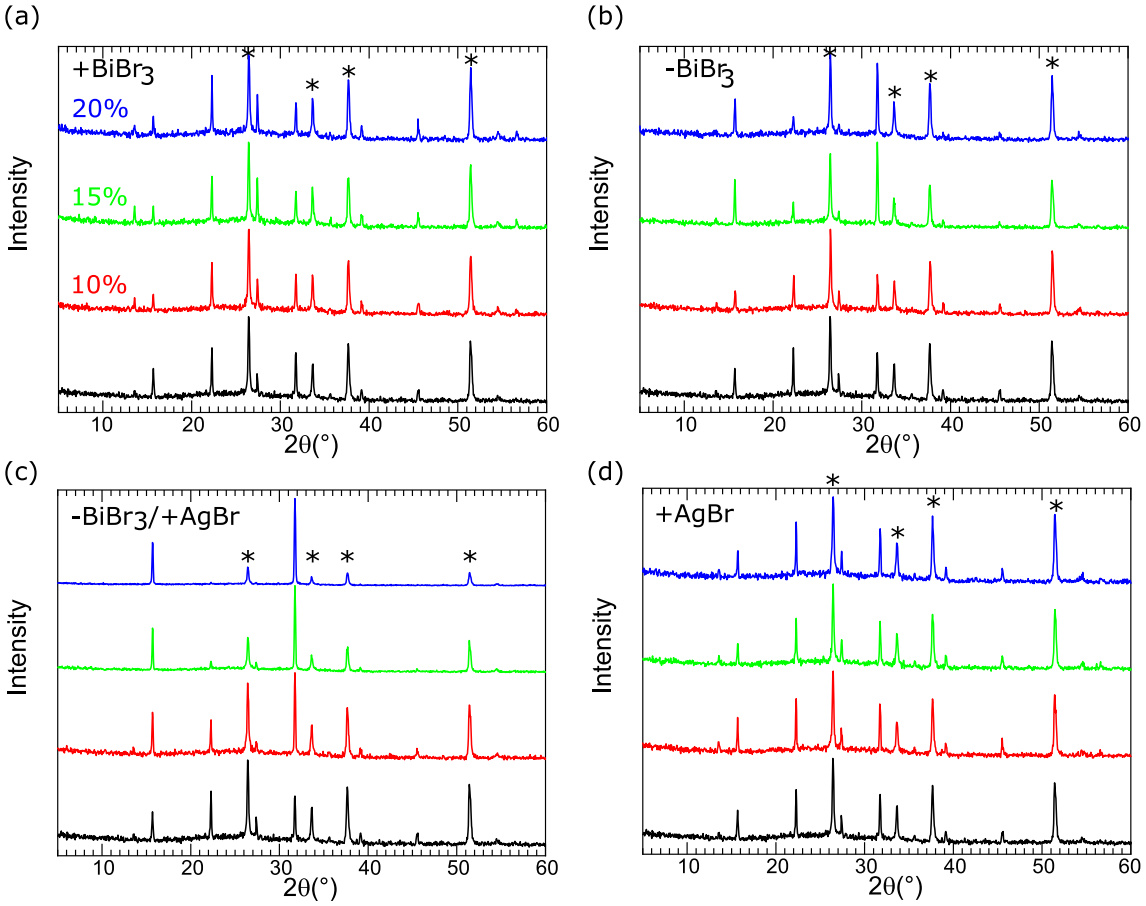

Figure 5.22: XRD patterns of $Cs_2AgBiBr_6$ thin films with the largest change in crystallinity and orientation. a) presents only films with $BiBr_3$ excess, b) shows films with $BiBr_3$ deficiency, c) depicts a thin film prepared from a combination of $BiBr_3$ deficiency and AgBr excess while d) only includes films with AgBr excess. The color coding for all graphs is identical and the black line always represents the stoichiometric reference. Asterisks label the Bragg reflections of the FTO substrate. Reprinted with permission from [144]. Copyright 2020 American Chemical Society.

ment were performed. To obtain the powder, the deposited films were scratched off the substrates. The powder XRD patterns in Figure 5.23 reveal different secondary phases for powders with different stoichiometric ratios. However, side phase formation when synthesizing the $Cs_2AgBiBr_6$ double perovskite can be expected for films with different

stoichiometry as presented below in Table 5.8. This can also be seen in Figure 5.23a for

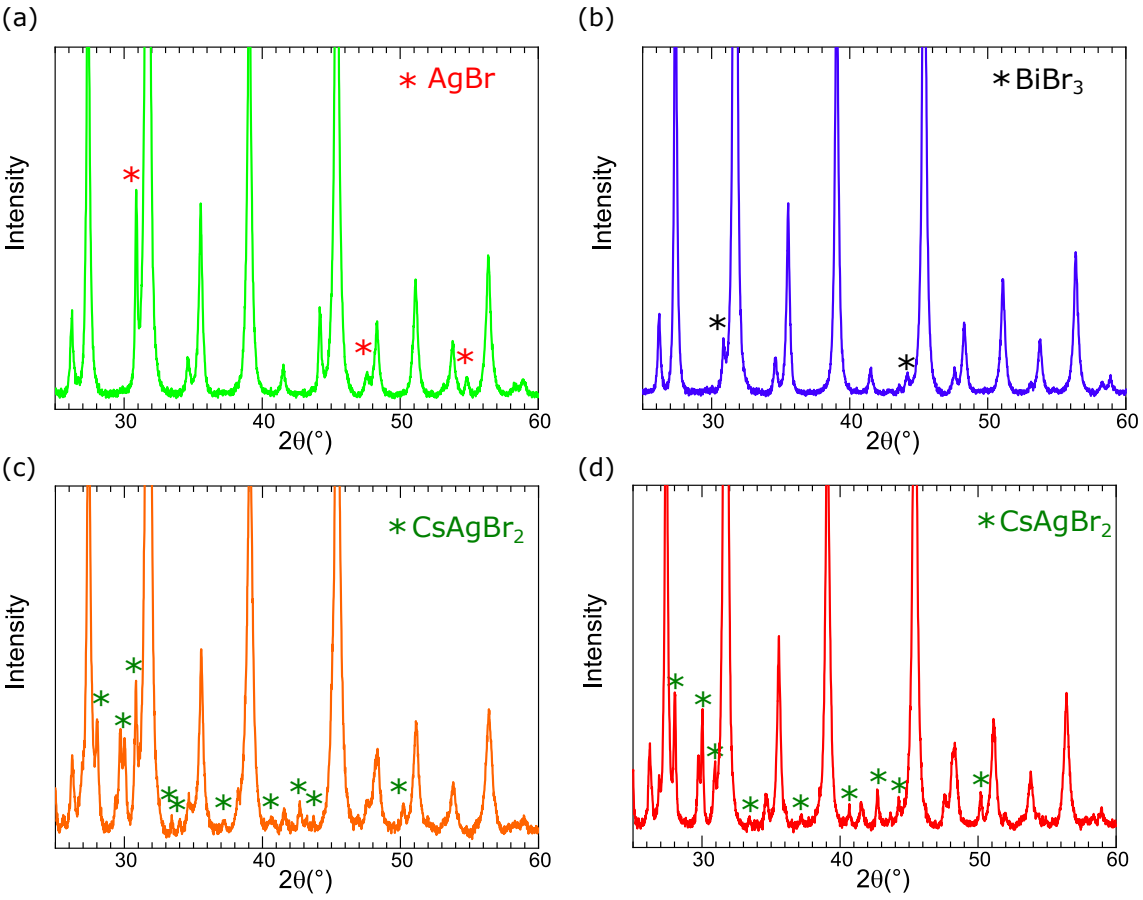

Figure 5.23: Powder XRD patterns of $Cs_2AgBiBr_6$ thin films with the following change in stoichiometry: a) (1.15 : 1), b) (1 : 1.15), c) (1 : 0.85) d) (1.15 : 0.85). The Bragg peak positions of the side phases are marked with asterisks. Red represents the side phase of AgBr, black of $BiBr_3$ while green depicts the $CsAgBr_2$ secondary phase. Reprinted with permission from [144]. Copyright 2020 American Chemical Society.

the (1.15 : 1) films as they show peaks at angles of 30.81 °, 44.13 ° and 54.86 °, which are caused by the AgBr sidephase. Additionally, films with the stoichiometry of (1 : 1.15) exhibit Bragg peaks at comparable angles. However, as no peak at 54 ° can be identified, it indicates a cubic $BiBr_3$ secondary phase for this stoichiometric alteration. This can be expected as described in Table 5.8 and depicted in Figure 5.23b. Moreover, films with a (1 : 0.85) stoichiometry only show the sidephase of $CsAgBr_2$. From the reaction scheme in Table 5.8, it is visible that in this case, CsBr should have formed additionally to $CsAgBr_2$. However, the Bragg peaks of CsBr are likely obscured by the Bragg peaks of $Cs_2AgBiBr_6$ in this case, as is shown in Figure 5.23c and d. In addition, the $CsAgBr_2$ secondary phase can also be found as the only side phase in (1.15 : 0.85) films, which supports the identification of the $CsAgBr_2$ side phase. The $CsAgBr_2$ side phase could also be confirmed by synthesizing pure $CsAgBr_2$, which was used for the powder XRD

1 : 1	$2\,CsBr + AgBr + BiBr_3 \longrightarrow Cs_2AgBiBr_6$
1.15 : 1	$2\,CsBr + 1.15\,AgBr + BiBr_3 \longrightarrow Cs_2AgBiBr_6 + 0.15\,AgBr$
1 : 1.15	$2\,CsBr + AgBr + 1.15\,BiBr_3 \longrightarrow Cs_2AgBiBr_6 + 0.15\,BiBr_3$
1 : 0.85	$2\,CsBr + AgBr + 0.85\,BiBr_3 \longrightarrow Cs_2AgBiBr_6 + 0.15\,CsAgBr_2 + 0.15\,CsBr$
1.15 : 0.85	$2\,CsBr + 1.15\,AgBr + 0.85\,BiBr_3 \longrightarrow 0.85\,Cs_2AgBiBr_6 + 0.3\,CsAgBr_2$

Table 5.8: Reaction scheme for double perovskite thin films with different stoichiometries

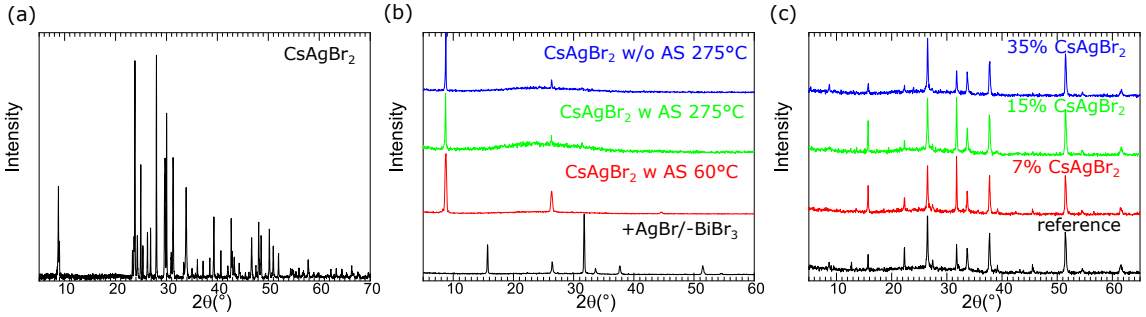

Figure 5.24: Powder XRD patterns of a) pure $CsAgBr_2$ and XRD pattern of thin films with $CsAgBr_2$ secondary phase with b) (1.15 : 0.85) stoichiometry for different annealing temperatures and IPA used as antisolvent (red and green lines), as well as pure $CsAgBr_2$ spin-coated without antisolvent (blue line). c) represents XRD patterns of thin films after adding $CsAgBr_2$ to the precursor solution. Reprinted with permission from [144]. Copyright 2020 American Chemical Society.

measurements in Figure 5.24a. Additionally, pure $CsAgBr_2$ thin films were fabricated and XRD patterns recorded in Figure 5.24b. Interestingly, the characteristic peak at 8 ° for the $CsAgBr_2$ sidephase is not visible in the thin film XRD but only in the recorded powder patterns. This indicates that only a very small ratio of this secondary phase can be found in the films. Furthermore, it hints at a rather low crystallinity of $CsAgBr_2$ compared to the double perovskite $Cs_2AgBiBr_6$. However, the formation of the secondary phase for (1.15 : 0.85) thin films could be confirmed by EDX measurements of the scraped-off powders, which is shown in Table 5.9. To further investigate the influ-

Element	**stoichiometric film [atom%]**	**1.15:0.85-film [atom%]**
Cs	19.84	21.60
Ag	10.59	12.73
Bi	9.58	8.53
Br	60.04	57.14

Table 5.9: Resulting atom% distribution in the powders of the stoichiometric $Cs_2AgBiBr_6$ thin film and the (1.15 : 0.85) thin film obtained from EDX measurements

ence of the $CsAgBr_2$ secondary phase on the crystallization behavior, stoichiometric $Cs_2AgBiBr_6$ thin films were prepared by spin coating them on top of a pure $CsAgBr_2$ layer. Following the thin film fabrication, XRD measurements of the thin films were

conducted. Figure 5.24c shows the behavior of film orientation differs from thin films produced directly from $BiBr_3$ deficiency combined with an AgBr excess. Furthermore, by adding $CsAgBr_2$ to the stoichiometric $Cs_2AgBiBr_6$ precursor solution at varying concentrations, it was not possible to achieve a similar orientation and crystallinity as compared to the (1.20 : 0.80) thin films. Even adding $CsAgBr_2$ at high concentrations of 35 %, no comparable crystallite orientation to the films with an excess/deficiency combination could be obtained. However, all films with added $CsAgBr_2$ show a strong Bragg reflection at 8 °, which could not be found in the XRD patterns of highly oriented $Cs_2AgBiBr_6$ thin films. In consequence, this shows that the $CsAgBr_2$ side phase hardly influences the structural properties of the $Cs_2AgBiBr_6$ thin films presented in this section.

5.2.5 Optoelectronic properties of $Cs_2AgBiBr_6$ thin films

A high orientation along the (001) plane in thin films has been proven to be beneficial for charge transport in lead-based perovskite systems.[186]–[188] Hence, the influence of crystallite orientation and change in stoichiometry of double perovskite thin films was studied by TRMC and PL measurements in a next step.
Figure 5.25a shows the different PL spectra of $Cs_2AgBiBr_6$ thin films with different precursor ratios with respect to the stoichiometric reference. The steady-state spectra were recorded on five different spots of the corresponding films and the results were later averaged. To prevent any influence of the FTO/TiO_2 substrates, all films were deposited on glass substrates. One can see, that all films show a significant Stokes-shift and broad PL peak around 2 eV, which is in good agreement with literature reports and was attributed both to the indirect bandgap emission and trap assisted recombination in $Cs_2AgBiBr_6$.[17], [91], [176] To further rule out any possible influence of $CsAgBr_2$ on the optoelectronic properties of the double perovskite thin films, UV-Vis and PL was performed on pure $CsAgBr_2$ films as well. The results in Figure 5.26 reveal no influence of the secondary side phase on the PL or absorption in the visible region. This suggests that $CsAgBr_2$ does not influence the optoelectronic properties of double perovskite thin films. While the UV-Vis absorption of the stoichiometric altered films in Figure 5.27a does not change significantly, the PL in Figure 5.27b shows the highest intensity for the (1 : 0.85) $BiBr_3$ deficient films. Additionally, a slight increase in the PL signal compared to the stoichiometric reference can be observed for the (1.15 : 0.85) and (1.20 : 0.80) films, although they show lower absorption than the stoichiometric reference. Furthermore, the PL data suggests that combining AgBr excess with $BiBr_3$ deficiency is most beneficial at a ratio of 15 mol%, as lower molar ratios show decreased PL in Figure 5.27b. Note that a higher steady-state intensity implies a larger amount of

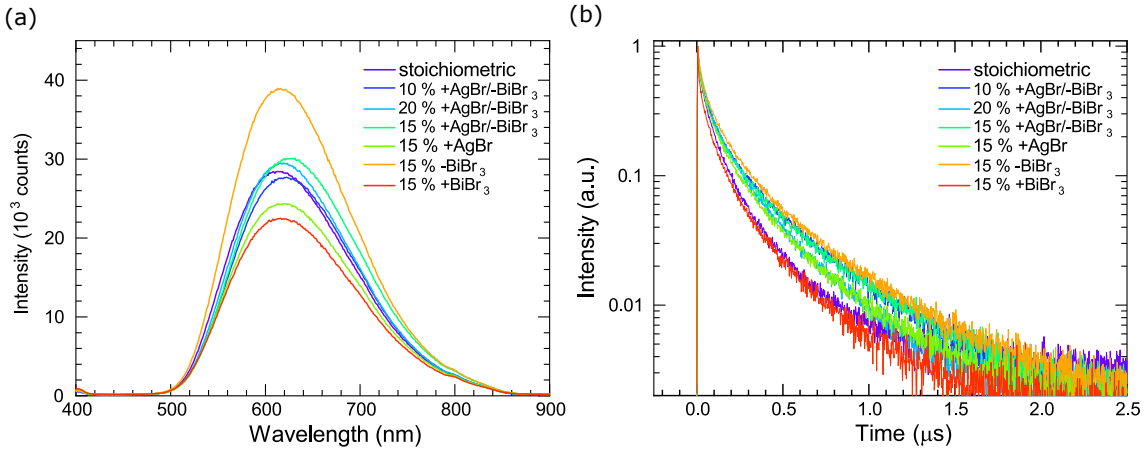

Figure 5.25: a) Steady-state photoluminescence and b) time-resolved photoluminescence of $Cs_2AgBiBr_6$ films with different precursor stoichiometry. Reprinted with permission from [144]. Copyright 2020 American Chemical Society.

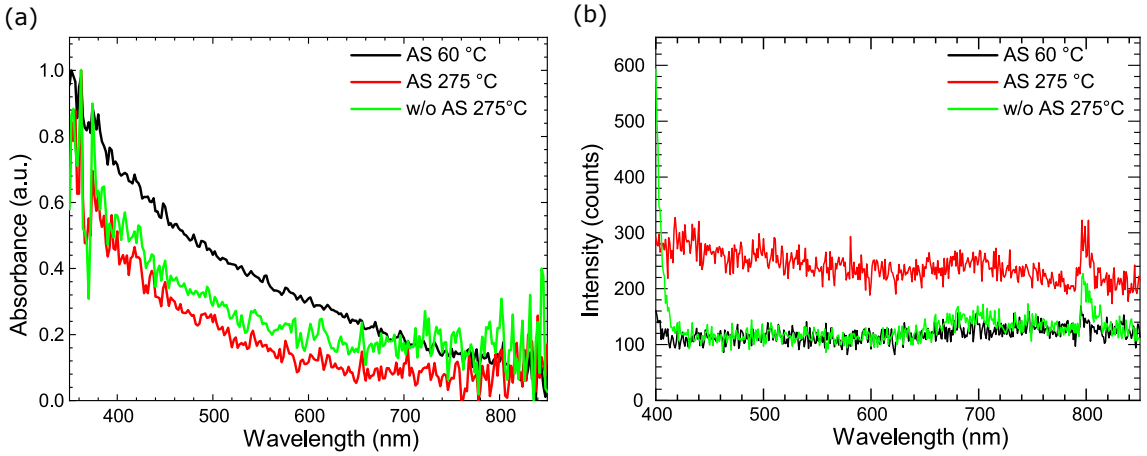

Figure 5.26: a) UV-Vis absorption and b) steady-state PL of pure $CsAgBr_2$ films. The black spectra depict absorption and PL of films annealed at 60 °C with isopropanol used as antisolvent. The red lines indicate films with isopropanol as antisolvent and an annealing temperature of 275 °C, while for the green spectra no antisolvent was used. Reprinted with permission from [144]. Copyright 2020 American Chemical Society.

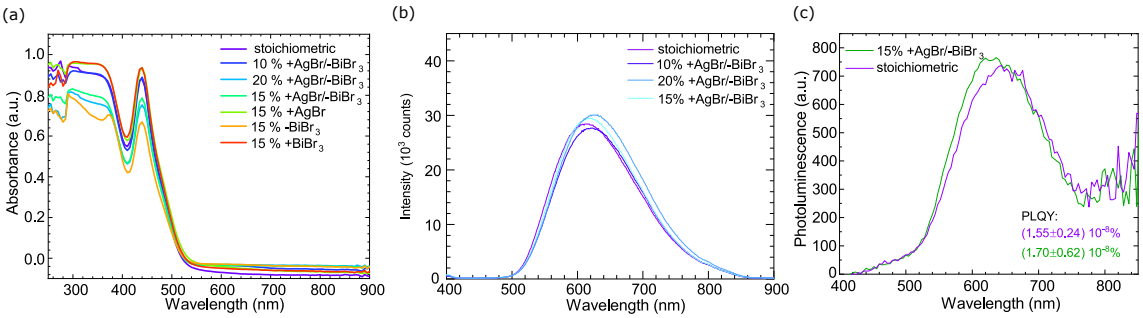

Figure 5.27: a) UV/Vis absorbance spectra and b) steady-state photoluminescence of $Cs_2AgBiBr_6$ thin films with different precursor stoichiometry. c) PLQY of a stoichiometric $Cs_2AgBiBr_6$ thin film as well as a film with 15 mol% AgBr excess and $BiBr_3$ deficiency. Reprinted with permission from [144]. Copyright 2020 American Chemical Society.

free charge carriers, [91] which in turn is beneficial for the open-circuit voltage and hence the power conversion efficiency of solar cells. Consequently, these results suggest that an additional amount of Bi^{3+} is detrimental for the films' performance as an increase of the $BiBr_3$ amount seems to have the largest negative impact on the PL of the films. However, in the case of AgBr excess, only the combination with a $BiBr_3$ deficiency results in an improvement of the PL signal. This further supports the fact that the amount of Bi^{3+} is a crucial part for stoichiometric changes of $Cs_2AgBiBr_6$ thin films. In order to quantify the recombination in $Cs_2AgBiBr_6$ thin films, PLQY measurements were conducted on the stoichiometric reference and the thin films with 15 mol% AgBr excess and $BiBr_3$ deficiency. Figure 5.27c shows very low PLQY values for both prepared stoichiometries, although stoichiometrically altered films reach slightly higher values. It has been shown in literature that only low PLQYs could be reached with this material system up to now, which shows that so far, $Cs_2AgBiBr_6$ still suffers from tremendous nonradiative losses within the material, which have to be addressed in the future.[189] To gain further knowledge about the charge carrier dynamics and the influence of precursor stoichiometry on the recombination dynamics, TCSPC measurements were performed. The data shown in Figure 5.25b were fitted with triple exponential functions to account for all contributions to the signal, as has been done in literature to evaluate transient photoluminescence data for $Cs_2AgBiBr_6$. This conventional evaluation has been chosen in order to compare the different films based on the different decay contributions discussed in literature.[17], [70], [141] However, as has been pointed out in section 4.1, multiexponential fitting has to be done with great care and does not enable a physical interpretation of the data. Hence, the presented lifetimes in Table 5.10 are only used to quantify the PL decays and make the comparison of the data easier.
Figure 5.25b shows that all films possess a fast decay component with lifetimes below

20 ns, followed by a slower component around 80 ns - 150 ns, as well as a long decay on larger time scales.
While the underlying mechanism of the first two decay contributions has not yet been explained in literature, the slowest fraction of the decay τ_3 was attributed to trap-assisted recombination in the past.[17], [70], [141]
Comparing the long living decay component reveals longer lifetimes for films either containing a sole $BiBr_3$ deficiency (505.2 ns) or a simultaneous combination with AgBr excess (464.4 ns). This hints towards a slowed down recombination via trap states and consequently should result in an improvement of solar cell efficiencies. Furthermore, the correlation between films showing the highest steady-state PL intensity with longer PL lifetimes suggests an overall reduced nonradiative recombination, although this effect might be rather small as was shown in Figure 5.27. However, these findings support the results from steady-state measurements that the trap density can be reduced if a Bi^{3+}-deficient system is employed, which also is in good agreement with the calculations of Li et al.[190]
Furthermore, fluence-dependent steady-state and time-resolved photoluminescence

Film	τ_1 **(ns)**	τ_2 **(ns)**	τ_3 **(ns)**	τ_{AVG} **(ns)**
stoichiometric	13.0 ± 1.4	82.5 ± 1.7	303.5 ± 5.5	172.3
10 mol% +AgBr/-$BiBr_3$	17.7 ± 1.4	116.6 ± 2.6	445.3 ± 5.5	285.5
15 mol% +AgBr/-$BiBr_3$	18.3 ± 1.5	122.8 ± 2.9	464.4 ± 6.6	291.1
20 mol% +AgBr/-$BiBr_3$	19.6 ± 1.6	110.4 ± 2.1	363.1 ± 4.8	223.0
15 mol% +AgBr	16.8 ± 1.3	101.9 ± 2.0	378.3 ± 4.9	232.0
15 mol% -$BiBr_3$	25.4 ± 1.7	143.9 ± 2.8	505.2 ± 6.8	299.5
15 mol% +$BiBr_3$	7.2 ± 8.5	76.2 ± 1.7	307.1 ± 5.2	187.6

Table 5.10: Overview of TRPL lifetimes extracted from triple exponential fits

measurements have been performed to study the recombination dynamics in the thin films in more detail. As the difference between the (1.15 : 0.85) film and the stoichiometric reference was the greatest, only those two stoichiometries will be investigated in the following.
The fluence-dependent steady-state measurements in Figure 5.28 reveal two different slopes between 1 mW/cm^2 and 1000 mW/cm^2 for both tested stoichiometries. For low intensities, a slope of 1.4 was found for both films. This is in agreement with literature and indicates a recombination pathway dominated by Shockley-Read-Hall recombination and therefore hints towards trap-assisted processes.[111] For high excitation intensities however, a slope of $m = 1$ was found for both films, which could be assigned to an excitonic contribution, since higher excitation intensity leads to a strongly increased amount of charge carriers. This in turn can lead to a smaller ratio of free

charge carriers to excitons as is stated by the Saha-Langmuir equation.[31] The data of

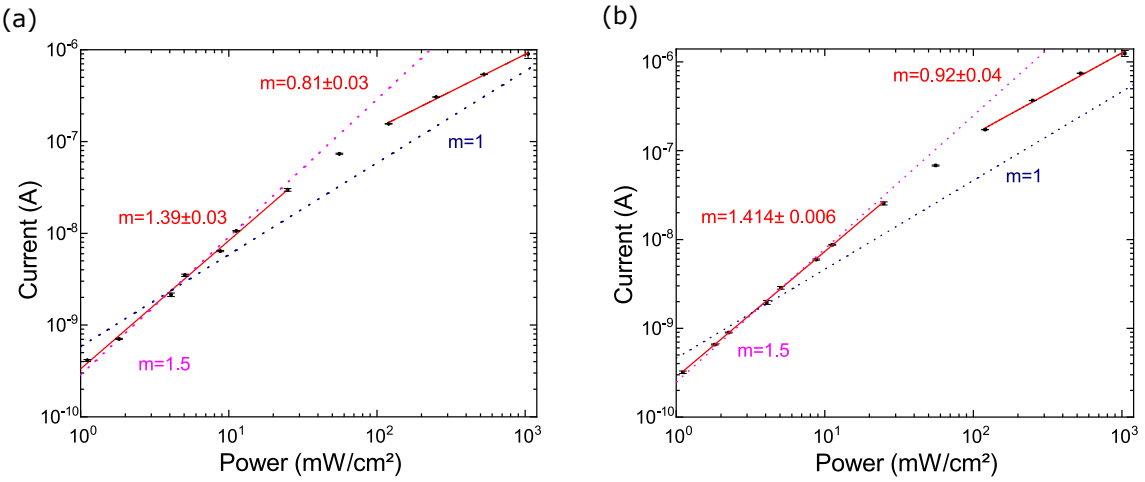

Figure 5.28: Fluence-dependent steady-state photoluminescence of a) the stoichiometric reference and b) a (1.15 : 0.85) $Cs_2AgBiBr_6$ thin film. The red lines represent the fits to the experimental data with the obtained slopes m shown in red. Pink and blue lines represent guides to eye for slopes $m = 1.5$ and $m = 1$. Reprinted with permission from [144]. Copyright 2020 American Chemical Society.

fluence-dependent TRPL measurements shown in Figure 5.29 show a similar behavior of both films, which is consistent with the results obtained by the steady-state experiments in Figure 5.28. This indicates the same dominating recombination pathways for both stoichiometries, which is in agreement with the fluence-dependent steady-state results. Additionally, neither of the films show a fluence-dependent behavior of the recombination rates in Figure 5.29, which is in agreement with the results obtained by other groups.[91] Hence, one can conclude that altering the stoichiometry of $Cs_2AgBiBr_6$ does not influence the dominating recombination mechanisms in this material. To get a better understanding of the charge carrier dynamics and to investigate the charge carrier mobility in $Cs_2AgBiBr_6$ thin films, TRMC measurements were conducted. As the PL results already indicated the $(1+x)$:$(1-x)$-films of 15 mol% to be the most promising, the focus was set on this stoichiometric alteration in the experiments. Figure 5.30 presents the obtained TRMC transients for the different stoichiometries. In TRMC, the change of photoconductance ΔG is measured as a function of time after pulsed optical excitation of the sample.[191] For this purpose, the sample was placed in a TRMC cavity and excited with a 355 nm pulsed 1 kHz laser. In order to obtain information about the charge carrier mobility μ, one has to look at the proportionality of the quantum yield Φ and the sum of the electron and hole mobility $\Sigma\mu$ to ΔG as shown below.

$$\Phi\Sigma\mu = \frac{\Delta G_{max}}{\beta e I_0 F_A} \tag{5.2}$$

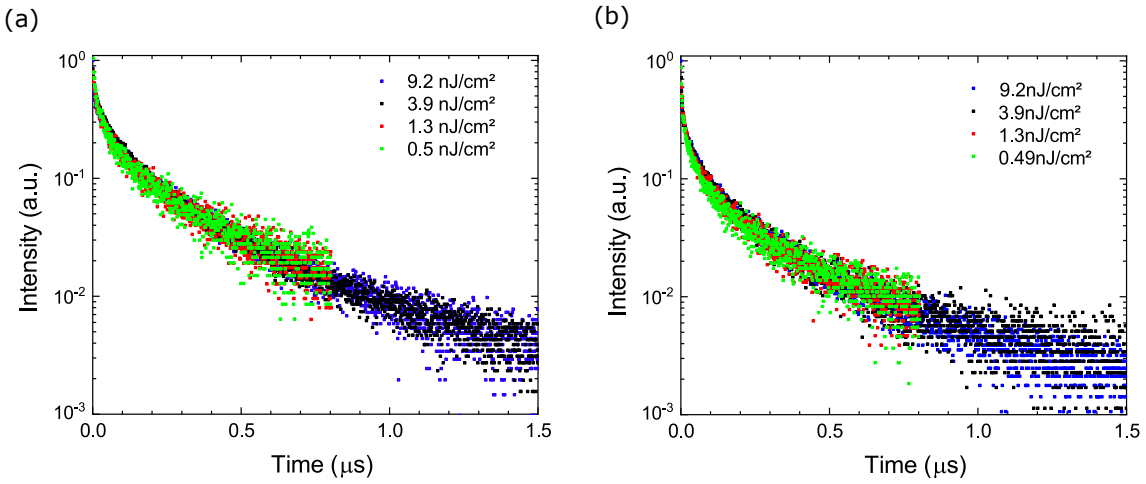

Figure 5.29: Fluence-dependent TRPL of a) the stoichiometric reference and b) a (1.15 : 0.85) $Cs_2AgBiBr_6$ thin film. Reprinted with permission from [144]. Copyright 2020 American Chemical Society.

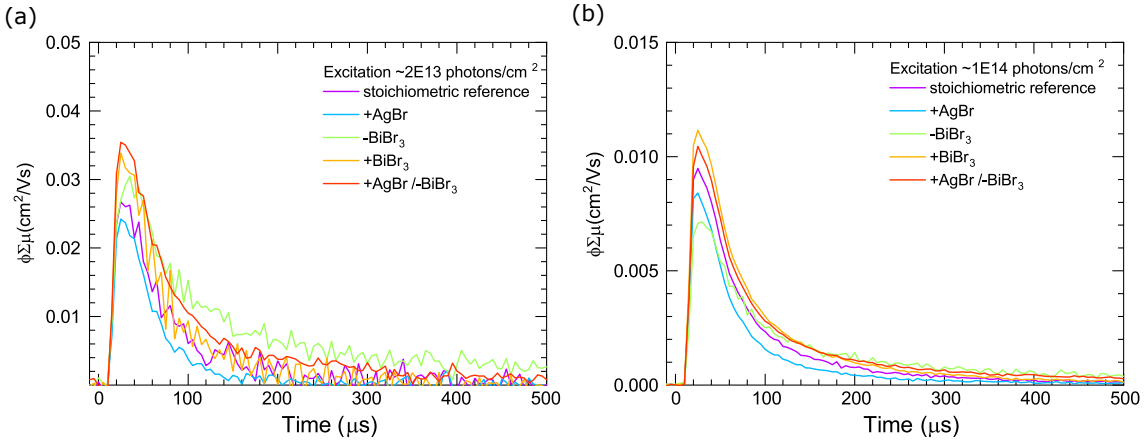

Figure 5.30: Intensity-dependent mobility obtained at RT for $Cs_2AgBiBr_6$ thin films with different stoichiometries of 15 mol% variation. Note that the product of mobility and quantum yield does not seem to saturate for low intensity values, which can be assigned to excitonic contributions of the material. Reprinted with permission from [144]. Copyright 2020 American Chemical Society.

Here I_0 presents the number of incident photons, F_A is the fraction of absorbed light, e is the elemental charge and β represents the ratio of the inner dimensions of the TRMC cavity.

In 2018, Bartesaghi et al. first investigated $Cs_2AgBiBr_6$ single crystals using TRMC and revealed that the material presents a large number of surface traps.[173] Additionally, Bartesaghi et al. showed only low mobilities of at least 0.1 $cm^2/(Vs)$.[173] Using a similar setup and a microwave frequency of 9 GHz, intensity dependent $\Phi\Sigma\mu$ measurements were performed at room temperature. For high excitation intensity, only a small value of $\Phi\Sigma\mu$ can be observed, although the strong absorption at 355 nm indicates a high charge carrier density. However, a higher amount of charge carriers in general leads to a faster recombination within the response time of the TRMC setup. Furthermore due to an overall reduced ratio of free charge carriers to excitons the quantum yield reaches values below 1.[191] Figure 5.31 shows the $\Phi\Sigma\mu$ product for different intensities. It becomes obvious that the product of quantum yield and mobilities does not saturate for lower intensities. However, the mobility in general is considered an intensity-independent property. Therefore, this strengthens the assumption that the free carrier quantum yield is significantly below 1 for $Cs_2AgBiBr_6$ and that additionally a large amount of strongly bound Frenkel excitons are created within the material. Thus, to reach a quantum yield of 1, a considerably smaller excitation intensity is required.

However, it was not possible to obtain TRMC decays with a sufficient signal-to-noise ratio for low excitation intensities, which might be caused by the rather high exciton binding energy of 268 meV in $Cs_2AgBiBr_6$.[70] As a consequence a lower estimate for the charge carrier mobility of the investigated films can be provided in this section.

To further rule out different behavior of the films, due to different film thicknesses and absorption behavior, absorption measurements were performed and the film thickness was estimated by profilometry. The obtained film thicknesses are shown in Table 5.11. Note that the thicknesses provided in Table 5.11 differ from the ones achieved for PL measurements. This is due to the use of sapphire-glass with a lower surface roughness compared to the used FTO substrate employed for the PL measurements, presented earlier. Hence, one can conclude that the different behavior of the thin films is not caused by thickness variations but is instead an intrinsic property of the investigated film. In agreement with literature, the product of quantum yield and the sum of the electron and hole mobilities of the different films drop with an increase of laser intensity in Figure 5.31.[173] This can be related to the smaller quantum yield at higher intensity caused by the smaller ratio of free charge carriers to excitons and faster recombination. The results in Figure 5.31 show that the product of quantum yield and

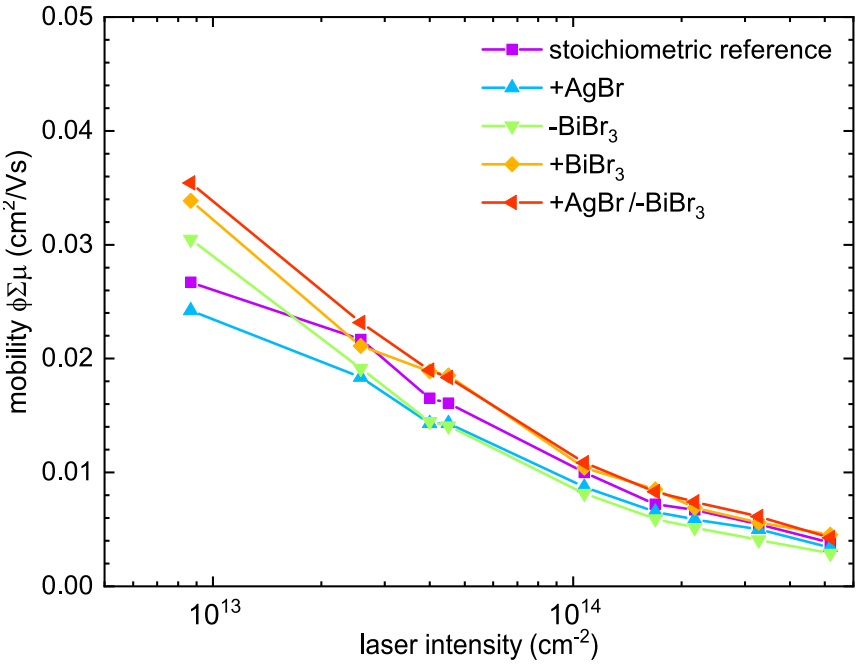

Figure 5.31: Intensity-dependent mobility obtained at RT for $Cs_2AgBiBr_6$ thin films with different stoichiometries of 15 mol% variation. Note that the product of mobility and quantum yield does not seem to saturate for low intensity values, which can be assigned to excitonic contributions of the material. Reprinted with permission from [144]. Copyright 2020 American Chemical Society.

mobility is the highest for (1.15 : 0.85)-films for all laser intensities. Moreover, at lower laser intensity, the stoichiometric reference and the (1 : 1.15)-films show comparable values.

Although the exciton binding energy in $Cs_2AgBiBr_6$ is ten-fold higher compared to conventional perovskites like $MAPbI_3$, excitonic contributions cannot be taken into account by TRMC.[70] This is due to the fact, that TRMC can only measure contribution from free charge carriers compared to other optical techniques such as PL, where all mechanisms which influence the charge carrier recombination are influencing the detected signal. With the performed TRMC measurements, one must consider that the obtained charge carrier mobilites are significantly underestimated since the quantum yield is strongly dependent on the fraction of free charge carriers and therefore also on the exciton binding energy as shown in Equation 5.3.[31] To further determine the absolute values of the charge carrier mobility, the quantum yield was corrected with the Saha-Langmuir equation in Equation 5.3.

$$\frac{x^2}{1-x} = \frac{1}{n}\left(\frac{2\pi m^* k_B T}{h^2}\right)^{\frac{3}{2}} \exp^{-\frac{E_b}{k_B T}} \tag{5.3}$$

film parameter	quantum yield	$\Phi\Sigma\mu$ [cm^2/Vs]	$\Phi\Sigma\mu$ [cm^2/Vs]	thickness [nm]
reference	0.0064	0.027	4.2	116 ± 20
1.15 : 1	0.0069	0.024	3.5	134 ± 19
1 : 1.15	0.0067	0.034	5.1	125 ± 16
1 : 0.85	0.0064	0.031	4.8	101 ± 21
1.15 : 0.85	0.0072	0.036	5.0	136 ± 18

Table 5.11: Quantum Yield, Product of quantum yield and mobility, estimated mobility and measured thicknesses for the double perovskite films of different stoichiometries

Here x is the fraction of free charge carriers, n the total charge carrier density, T the temperature, k_B the Boltzmann constant, E_B the exciton binding energy and m^* is the reduced exciton mass, which was determined by Feng et al.[31], [192] Using this correction, the true charge carrier mobility shown in Equation 5.3 could be estimated. However, one must note that a large fraction of the free charge carriers recombines within the response time of the TRMC setup. Therefore, the $\Phi\Sigma\mu$ product presented here must be considered a lower limit for the actual charge carrier mobility in these $Cs_2AgBiBr_6$ thin films.
Hence, employing the Saha-Langmuir equation resulted in the highest charge carrier mobility for (1.15 : 0.85) thin films, as can be extracted from Table 5.11. However, earlier reports on mobilities of lead-free double perovskites did not account for excitonic contributions. Hence lower mobility values compared to the values presented in this section were reported by Bartesaghi et al.[173] Taking the low quantum yields of the prepared samples into account finally allows for a more precise estimate of the lower boundary of the actual mobility of lead-free double perovskites.
Altogether, the presented results confirm the trend observed from PL studies which suggest improved charge carrier dynamics for films with a (1.15 : 0.85) stoichiometry.

5.2.6 Influence of stoichiometry on device performance

To further study the impact of stoichiometry on solar cell performance, the different double perovskite thin films were used as absorber layers in devices with an architecture of FTO/TiO_2/$Cs_2AgBiBr_6$/P3HT/Au. The film thickness was fixed to 150 nm in order to exclude variations of absorption for all samples. Furthermore, the following statistics will only include working devices to gain more reliability.
The best I-V curves for solar cells with the stoichiometry of (1.15 : 0.85) as well as the stoichiometric reference are presented in Figure 5.32. Additionally, the obtained parameters of the solar cells such as open-circuit voltage (V_{OC}), short-circuit current

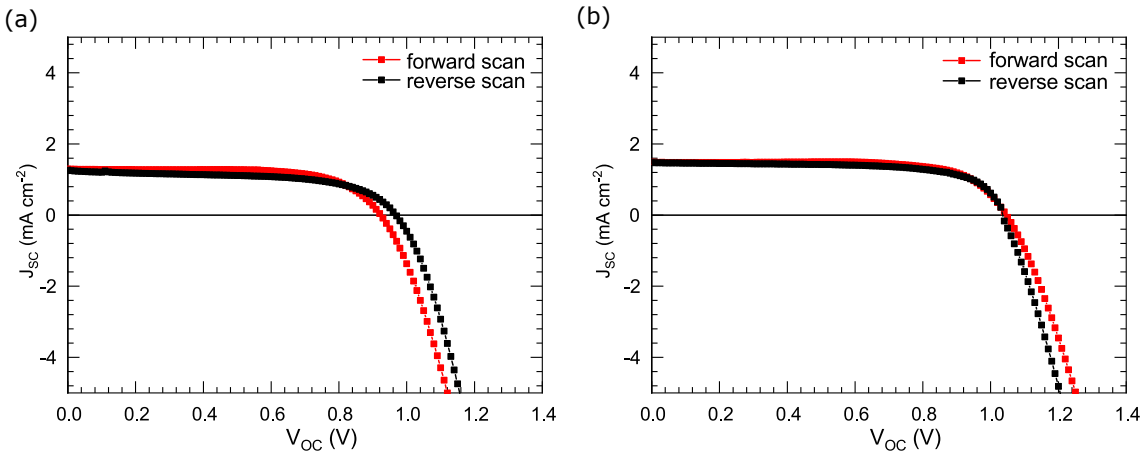

Figure 5.32: J/V-curves of the best solar cells of the a) stoichiometric reference and b) the (1.15 : 0.85) device. Reprinted with permission from [144]. Copyright 2020 American Chemical Society.

(J_{SC}), fillfactor (FF) and power conversion efficiency (PCE) are depicted in Figure 5.33.

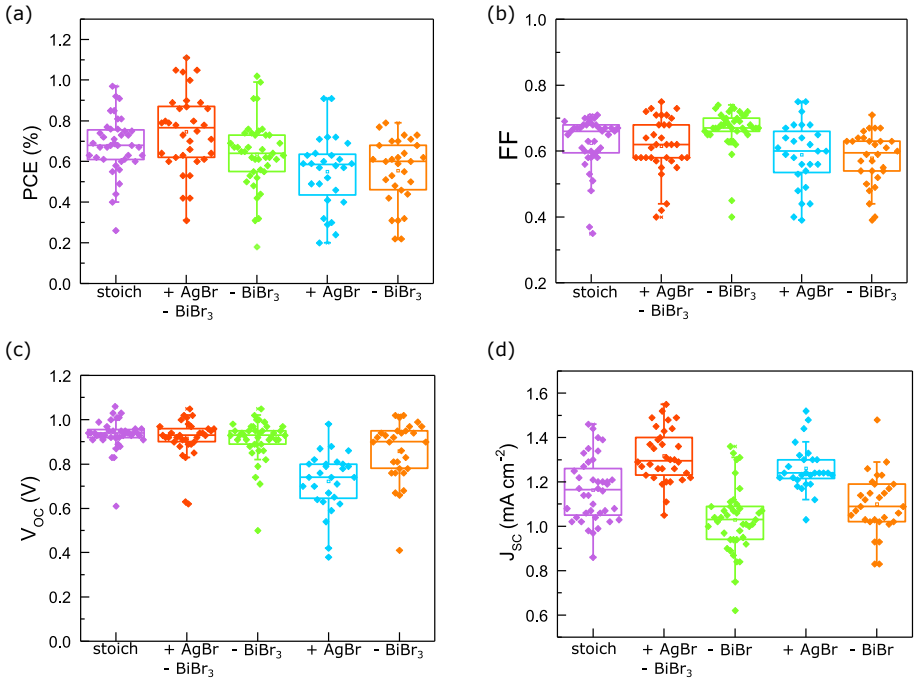

Figure 5.33: Characteristic parameters of the fabricated solar cells, with 15 mol% excess, deficiency or a combination of both. Panel a) shows the achieved power conversion efficiency (PCE), b) the fill factor, c) the reached V_{OC} values and c) the J_{SC} values for the devices. Reprinted with permission from [144]. Copyright 2020 American Chemical Society.

As can be seen in Figure 5.33a, the cells fabricated with a (1.15 : 0.85) stoichiometry reached efficiencies of 1.11 %. This was the highest average PCE amongst all prepared

solar cells. The stoichiometric films however reached efficiencies of only 0.97 %. Furthermore, other prepared stoichiometries such as (1.15 : 1), (1 : 0.85) as well as (1 : 1.15) show additional decrease in PCE compared to the stoichiometric reference. This once again confirms the trends observed in PL and TRMC measurements shown previously. The origin of the difference in PCE of the (1.15 : 0.85) device compared to the stoichiometric solar cell can be found in an increased J_{SC} and FF of the devices shown in Figure 5.33b and d. The increase in J_{SC} is caused by an improvement of the charge carrier dynamics, which was also suggested by TRMC and TCSPC experiments. Additionally, a better surface morphology can lead to improved solar cell parameters, which is further supported by the higher FF of the devices. Furthermore, for the champion device, the V_{OC} of the (1.15 : 0.85) films is increased as well, while the average value stays constant (Figure 5.33c). This is in agreement with the optoelectronic studies presented earlier.
The presented results show that changing the precursor stoichiometry of the films to an AgBr excess combined with a $BiBr_3$ deficiency by 15 mol% can improve the photovoltaic performance of devices. As a result, an increase in J_{SC} and FF can be obtained, suggesting that modifying the $Cs_2AgBiBr_6$ films allows for improved charge transport and charge carrier extraction, which was also suggested by TRMC and PL experiments. Consequently, the presented data for $Cs_2AgBiBr_6$ devices is consistent with findings for lead-based double perovskites, which indicates that an increased crystallite orientation along the (001) direction significantly improves the charge extraction. As a consequence, a rise in J_{SC} and therefore an overall increased performance of the devices can be observed as charge transport along the (001) direction is favored.[178]–[181]

5.2.7 Conclusion

In this section another way to further improve the optoelectronic properties of $Cs_2AgBiBr_6$ thin films was established. By tuning the stoichiometry of the precursor solution and working in an AgBr excess, $BiBr_3$ deficiency or a combination of both the domain orientation and crystallization could be controlled. Examination of the structural properties of the prepared films showed a strong increase in orientation along the (001) direction in (1.15 : 0.85) films. The conducted analysis also revealed the formation of a $CsAgBr_2$ sidephase, which however was found to not impact the structural and optoelectronic properties of the material.
Further investigation of the optoelectronic properties of the prepared films revealed an improvement of the PL lifetime for the (1.15 : 0.85) and (1 : 0.85) films from roughly 250 ns to 500 ns compared to the stoichiometric reference. In addition, TRMC studies disclosed an increase in mobility and conductivity, which in consequence lead to an enhancement of the photovoltaic properties of the material.

By studying solar cells with the architecture FTO/TiO_2/$Cs_2AgBiBr_6$/P3HT/Au PCEs of up to 1.11 % could be achieved by implementing the (1.15 : 0.85) stoichiometric ratio. Using this alteration in stoichiometry also increased the J_{SC} of the devices by 13 % compared to the stoichiometric reference. This could be assigned to a controlled crystal domain orientation, which is consistent with literature reports concerning lead-based perovskite solar cells.

This section introduced a way to easily tune the properties of $Cs_2AgBiBr_6$ by changing the stoichiometry of the AgBr and $BiBr_3$ precursors used in thin film fabrication. As a result, the here presented optimized crystallite orientation opens possibilities to further enhance charge transport as well as improve charge extraction and therefore can be seen as an important tool to further improve the performance of lead-free double perovskite solar cells.

6 Optoelectronic properties of $Cs_2NaFeCl_6$ single crystals

Lead-free double perovskites have attracted great attention as possible alternative to the lead-halide based perovskites in photovoltaic applications.[17], [46], [193], [194] However, up to now only few double perovskites such as $Cs_2AgBiBr_6$ have been successfully employed in devices.[194]–[196] In addition, as shown in the previous chapter, challenges such as tailstates, correct stoichiometry and optimization of the fabrication conditions are still to be overcome. Therefore, the search for other stable and lead-free materials is ongoing. In this chapter, the successful growth of high-quality $Cs_2NaFeCl_6$ single crystals and its temperature dependent structural, optical and magnetic properties are presented. By combining electron paramagnetic resonance (EPR), crystal structure analysis and density functional theory (DFT) a cubic crystal structure with a spin of 5/2 could be determined. Additionally, DFT calculations suggest a spin-polarized electronic character with an indirect semiconducting bandgap, which shows a direct transition located only 30 meV below the valence band maximum. Furthermore, connecting photoluminescence (PL) and absorption measurements, one finds a bandgap of approximately 2.1 eV at room temperature as well as the presence of excitonic states. Using Elliot's formula, it was possible to estimate the temperature-dependent behavior of the bandgap as well as an estimated exciton binding energy of only 20 meV at 80 K.

The presented work of this section is based on the paper: "Low Temperature optical properties of novel lead-free $Cs_2NaFeCl_6$ single crystals" by **Melina Armer**, Patrick Dörflinger, Andreas Weis, Carsten Büchner, Andreas Gottscholl, Julian Höcker, Kilian Frank, Lukas Nusser, Maximilian T. Sirtl, Bert Nickel, Thomas Bein and Vladimir Dyakonov published in Adv. Photonics. Res. in 2023, volume 4, article number 2300017 pages 1-9.

6.1 Earth abundancy of lead-free double perovskites

Lead-free double perovskites are becoming more and more popular due to their promising properties, such as long photoluminescence lifetimes, high crystallinity and high stability to oxygen and humidity.[42], [46], [197] Nevertheless, the usage of lead-free double perovskites in electronic devices is an ongoing and challenging project, although it is possible to manufacture prototypes of X-ray detectors, photodetectors and light emitting diodes.[64], [90], [142], [146], [195], [198] Furthermore, it was recently shown that double perovskite solar cells are strongly limited by their indirect bandgaps, high trap densities, low charge carrier diffusion lengths, unfavorable energy level alignment in the commonly used solar cell architectures and poor contact selectivity in the device.[69], [199] Although $Cs_2AgBiBr_6$ is the most promising stable lead-free double perovskite up to now, the rare earth metal Ag is needed for its synthesis. However, Ag only makes up about $7 \cdot 10^{-6}$wt% of the earth's crust.[200] This means, that although $Cs_2AgBiBr_6$ is non-toxic, the use of Ag in the perovskite does not make it earth abundant. Therefore, the search for other lead-free double perovskite structures and the investigation of their characteristic physical properties as well as their possible limitations is ongoing.

Recently, cesium sodium iron chloride ($Cs_2NaFeCl_6$) single crystals were introduced as new promising lead-free double perovskite material for thermochromic applications. It has been shown that this material has a bandgap of 2.07 eV and exhibits promising absorption in the visible region.[89] Furthermore, by doping $Cs_2NaFeCl_6$ with small amounts of Ag, the structure property relation has been studied.[89] It was found that incorporating Ag into the crystal structure leads to a decrease of the lattice constant.[89] As a result, it was also possible to significantly modify the bandgaps of crystals with a stoichiometry of $Cs_2Ag_xNa_{1-x}FeCl_6$ ($0 \leq x \leq 1$) from 2.07 eV for the pure $Cs_2NaFeCl_6$ to 1.55 eV for $Cs_2AgFeCl_6$.[89]

Although Ag-doped $Cs_2NaFeCl_6$ shows promising properties for the application in photovoltaic devices such as a tuneable bandgap and improved charge carrier mobilities [89], only little is known about the fundamental physical properties of the pure $Cs_2NaFeCl_6$. Latest studies proposed a fundamental change of the optical properties from low to high temperatures, due to an order-disorder transition in the material.[201] The observed order-disorder transition is caused by the expansion of the lattice constant of $Cs_2NaFeCl_6$, which results in slight variations of bond lengths and bond angles with rising temperature. As a result, a reversible color change of the crystal was observed going from yellow at 80 K to red at 300 K and to black at 500 K. It was concluded

that the color change of the crystal and the temperature-dependent bandgap variation make $Cs_2NaFeCl_6$ a promising candidate for thermochromic applications.[201] Although a significant temperature dependence of the bandgap was reported, nothing is known about the emission properties of $Cs_2NaFeCl_6$. However, a material's emission is an important key factor in whether it can be used as an absorber layer in photovoltaic devices.[111]
In this chapter, the growth of high-quality $Cs_2NaFeCl_6$ single crystals by the established controlled cooling method is described.[17], [83], [89], [201], [202] Moreover, detailed qualitative, quantitative and structural measurements by applying XRF, EDX and XRD are conducted to confirm the growth of high-quality single crystals with the specified stoichiometry. In addition, the temperature dependence of the crystal structure by means of electron paramagnetic resonance (EPR) is investigated to identify a possible structural phase transition of $Cs_2NaFeCl_6$ at low temperatures. Moreover, DFT calculations were conducted to elucidate the electronic structure and possible spin states as Fe(III) exhibits unpaired spins in the d-orbital. In the last step, the color change of the crystal was studied extensively by means of temperature-dependent photoluminescence and absorptance. The applied measurement techniques provided a deeper understanding of the fundamental properties of $Cs_2NaFeCl_6$.

6.2 Crystal growth and material characterization

6.2.1 Materials and solvents

Cesium chloride (CsCl, 99.9 %) and sodium chloride (NaCl, anhydrous ≥ 99%) were purchased from Sigma Aldrich. Iron(III)chloride ($FeCl_3$, anhydrous, 98 %) was purchased from Alfa Aesar. Hydrochloric acid (HCl, 37 wt%) was purchased from our in-house chemical supply of the Faculty of Chemistry and Pharmacy of the University of Würzburg. All chemicals were used as received and without further purification.

6.2.2 Solubility curves of $Cs_2NaFeCl_6$

CsCl (2 mmol), NaCl (1 mmol) and $FeCl_3$ (1 mmol) were weighed in stoichiometric amounts into a 3 ml glass vial in a nitrogen filled glovebox (water and oxygen compound below 1 ppm). The solubility curve was achieved by adding small amounts of HCl (200 μl) every hour under constant stirring of the solution, until the precursor salts were completely dissolved. This was done for solution temperatures from 25 °C to 100 °C, in order to obtain an exact solubility curve for $Cs_2NaFeCl_6$ in HCl.

6.2.3 Crystal growth of $Cs_2NaFeCl_6$

In order to obtain $Cs_2NaFeCl_6$ crystals from HCl, the commonly known crystal growth protocol for $Cs_2AgBiBr_6$ was followed.[17] A 0.3 molar solution of CsCl (2 mmol, 252.54 mg), NaCl
(1 mmol, 43.83 mg) and $FeCl_3$ (1 mmol, 121.65 mg) was prepared with 10 ml of 37 wt% HCl. The solution was placed on a hotplate in an oil bath and heated to 100 °C for 2 h, in order to obtain a completely dissolved precursor solution. To promote crystal growth, the solution was cooled down at a rate of 1 °C/h to RT. The crystals were then washed and dried with DCM in order to avoid any precursor precipitates remaining on the surface.

6.2.4 Structural and optical characterization of the crystals

Characterization of stoichiometry and crystal structure

EDX, XRF, XRD and crystal structure analysis were performed in order to evaluate the obtained stoichiometry as well as the crystal structure of the grown crystals.
EDX characterization of the crystal surface was performed in high vacuum using a scanning electron microscope (SEM) Carl Zeiss Ultra 55+ and an INCAPentaFET-x3 Si(Li) detector to obtain the elemental distribution of Cs, Na, Fe and Cl. At least four working areas on the crystals were measured. The obtained data was then normalized and averaged to obtain an average stoichiometry and elemental distribution over the whole crystal. EDX measurements were performed by Stefan Braxmeier at the ZAE Bayern.
Powder and single crystal XRD measurements as well as XRF measurements of the crystal powders were performed using a General Electric XRD 3003 TT with a monochromatic Cu-K_α radiation source (V = 40kV, I = 40mA) with wavelength λ of 1.5406 Å. Further XRF measurements were recorded with an XR-100T detector from Amptek and an X-ray machine from PHYWE. For the measurements, an unfiltered Molybdenum (Mo) - K_α radiation source (V = 35kV, I = 0.1mA) was used. All measurements were performed at RT.
The crystal surface facets were determined by reflectometry with a Mo-K_α radiation source (λ = 0.71073Å, V = 50kV, I = 1mA). The crystals were placed on an adhesive tape to carry out the measurements. The recorded XRD patterns were plotted against the scattering vector $q_z = \frac{4\pi}{\lambda} \cdot \sin(\theta)$, where θ is the scattering angle.[203] The measurements of the crystal facets as well as the XRD measurements performed with a Mo source were conducted by Julian Höcker and Kilian Frank, in the group of Bert Nickel at LMU Munich.

For crystal structure analysis, a specimen of $Cs_2NaFeCl_6$ with approximate dimensions of 0.020 mm·0.020 mm·0.030 mm was used for the X-ray crystallographic analysis. The X-ray intensity data was measured on a Bruker D8 Quest system equipped with a multilayer mirror optics monochromator and a Mo K_α rotating-anode X-ray tube($\lambda = 0.71073$Å). The measurements were performed at 297 K by Lukas Nusser at LMU Munich.

Characterization of spin properties

Continuous wave EPR measurements were performed with a Magnettech MS 5000 X. In order to reach cryogenic temperatures, the setup was extended with an oxford flow-type cryostat. The $Cs_2NaFeCl_6$ crystal was placed on a quartz rod sample holder and positioned in the center of the EPR resonator. The lowest applicable microwave power ($P_{MW} = 1\mu$W) was chosen to exclude saturation effects. A modulation amplitude of $B_{mod} = 0.5$mT was used to gain a sufficiently high signal-to-noise ratio without broadening the line shape of the observed EPR signature. EPR experiments were done by Andreas Gottscholl from the Dyakonov group in Würzburg.
Furthermore, DFT calculations were performed using the Quantum ESPRESSO package based on plane wave basis sets, employing the Perdew-Burke-Ernzerhof (PBE) parameterization of the generalized gradient approximation (GGA) for solids (PBEsol) to describe exchange correlation interactions.[204], [205] The GBRV high-throughput ultrasoft pseudopotential library was utilized to describe the interactions between valence electrons and atomic cores.[206] Additionally, the simplified Hubbard correction of Cococcioni and de Gironcoli was included.[207]–[209] A kinetic energy cutoff of 60 Ry for the wavefunctions and 500 Ry for the charge density was used. Self-consistent field (SCF) and geometry relax calculations were carried out on a fully converged 4·4·4 Monkhorst-Pack grid, while a larger mesh was utilized for the density of states calculations. The calculations presented in this chapter were done by Andreas Weis from LMU Munich.

6.2.5 Photoluminescence and absorptance

In order to investigate the emission properties of the grown crystals, temperature-dependent photoluminescence was measured using a FLS980 spectrometer from Edinburgh Instruments as described in section 4.1. The sample was placed in a cryostat and was cooled down using liquid nitrogen. PL was measured in reflection geometry. A Xenon lamp with tunable wavelength from Edinburgh Instruments was used as excitation source. The excitation wavelength was set to 336 nm.
Additionally, temperature dependent transmission was measured in a cryostat under

vacuum conditions. The sample was excited with a white light LED and transmission was detected as described in subsection 4.3.2.

6.3 $Cs_2NaFeCl_6$ crystal growth and structural characterization

In order to improve the growth process and obtain reproducible, phase-pure and large sized crystals, temperature dependent solubility diagrams were prepared in a first step. To achieve the correct stoichiometry, the precursor salts CsCl (2 eq), NaCl (1 eq) and $FeCl_3$ (1 eq) were dissolved in HCl (37 wt%).

Figure 6.1a shows that the solubility of the perovskite is approximately nine times higher at a temperature of 100 °C compared to RT. By slowly cooling down the solution at a rate of 1 °C/h, the solubility decreases. A reduced solubility with decreasing temperature has also been observed for the more common double perovskite $Cs_2AgBiBr_6$ in the past, when acids were used as solvents.[81], [88]

By slowly reducing the temperature, supersaturation of the perovskite solution was achieved at around 70 °C, followed by the formation of small nuclei. By further cooling the solution, the small crystal nuclei started to grow into larger red crystals. After successful growth, the crystals showed defined facets and a clear octahedral shape, typically observed for lead-free double perovskites.[64], [146], [201]

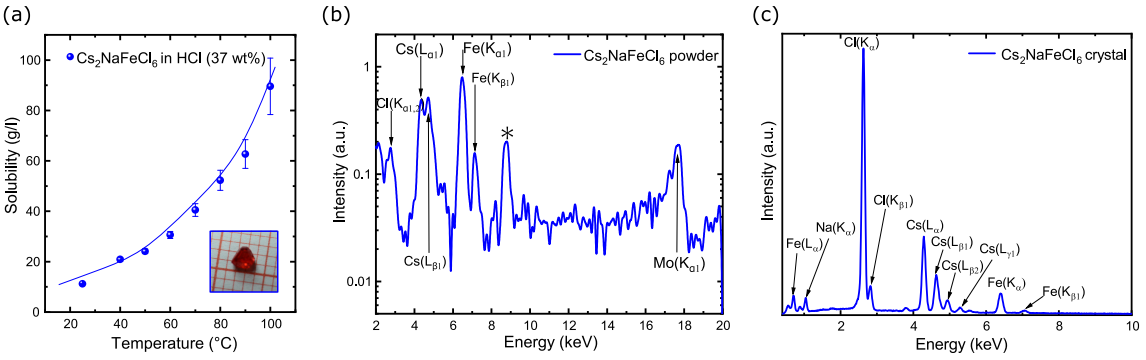

Figure 6.1: a) Temperature-dependent solubility of $Cs_2NaFeCl_6$ precursor salts with a photograph of a millimeter sized crystal as inset. b) XRF spectrum of a ground $Cs_2NaFeCl_6$ crystal with the assigned peaks for the elements Cs, Fe and Cl. The peak marked with an asterisk originates from the sample holder. c) EDX spectra of the crystal surface to verify the correct crystal composition and stoichiometry of $Cs_2NaFeCl_6$. Reproduced from [210] with permission from Wiley VCH GmbH.

Element	Expected atom fraction [%]	Crystal Surface atom fraction [%]	Crystal Powder atom fraction [%]
Cs	20	18.76	20.97
Na	10	11.25	9.22
Fe	10	8.44	9.97
Cl	60	61.55	59.84

Table 6.1: Quantitative analysis of the $Cs_2NaFeCl_6$ crystal surface and the crystal powder by EDX.

Afterwards, the crystals were analyzed by means of XRF and EDX in order to confirm the incorporation of the elements cesium (Cs), sodium (Na), iron (Fe) and chloride (Cl) by their corresponding photon energies determining their stoichiometry. For XRF measurements the crystals were ground into a fine powder. Figure 6.1b clearly identifies the $L_{\alpha 1}$ and $L_{\beta 1}$ X-ray emission lines of Cs at 4.34 keV and 4.72 keV, respectively. Moreover, the K_α and $K_{\beta 1}$ lines of Fe and Cl at the photon energies 6.51 keV, 7.10 keV and 2.79 keV could be assigned. However, no emission lines for Na were observed, due to the very low photon energies of the Na shells.[211]
By measuring EDX, it was possible to detect the elemental composition of the crystal surface. Figure 6.1c depicts the obtained EDX spectrum, clearly showing the K-shell emission line of Na at 1.04 keV. Additionally, the emission lines for Cs ($L_{\alpha 1}$ = 4.29keV, $L_{\beta 1}$ = 4.63keV, $L_{\beta 2}$ = 4.95keV, $L_{\gamma 1}$ = 5.3keV), Fe (L_α = 0.71keV, $K_{\alpha 1}$ = 6.4keV, $K_{\beta 1}$ = 7.05keV) and Cl (K_α = 2.62keV, K_β = 2.82keV) were identified. Therefore, the obtained XRF and EDX results already hint towards a successful growth of $Cs_2NaFeCl$ crystals via the controlled cooling method. In order to determine the exact stoichiometry of the grown crystals, quantitative EDX measurements were additionally performed yielding information about the atom fractions of each element of the crystal surface. Additionally, EDX measurements performed on $Cs_2NaFeCl_6$ powder confirmed the correct stoichiometry in the crystal bulk as well. Table 6.1 shows a nearly perfect experimentally determined stoichiometry of $Cs_2NaFeCl_6$ crystals and powder.
To further confirm the crystal structure, XRD measurements of the crystal powder were conducted. The XRD pattern in Figure 6.2 suggests a phase-pure growth of $Cs_2NaFeCl_6$ when compared to the crystal structure analysis data from literature.[212] By fitting the peaks of the obtained XRD pattern, it was possible to determine the Miller Indices and compare the identified reflexes with the simulated scan, shown in Figure 6.2. Hence, a simple cubic (sc) crystal structure with a lattice constant of $a = (10.35 \pm 0.03)$Å at RT could be determined, which is in perfect agreement with results published recently.[201], [212]

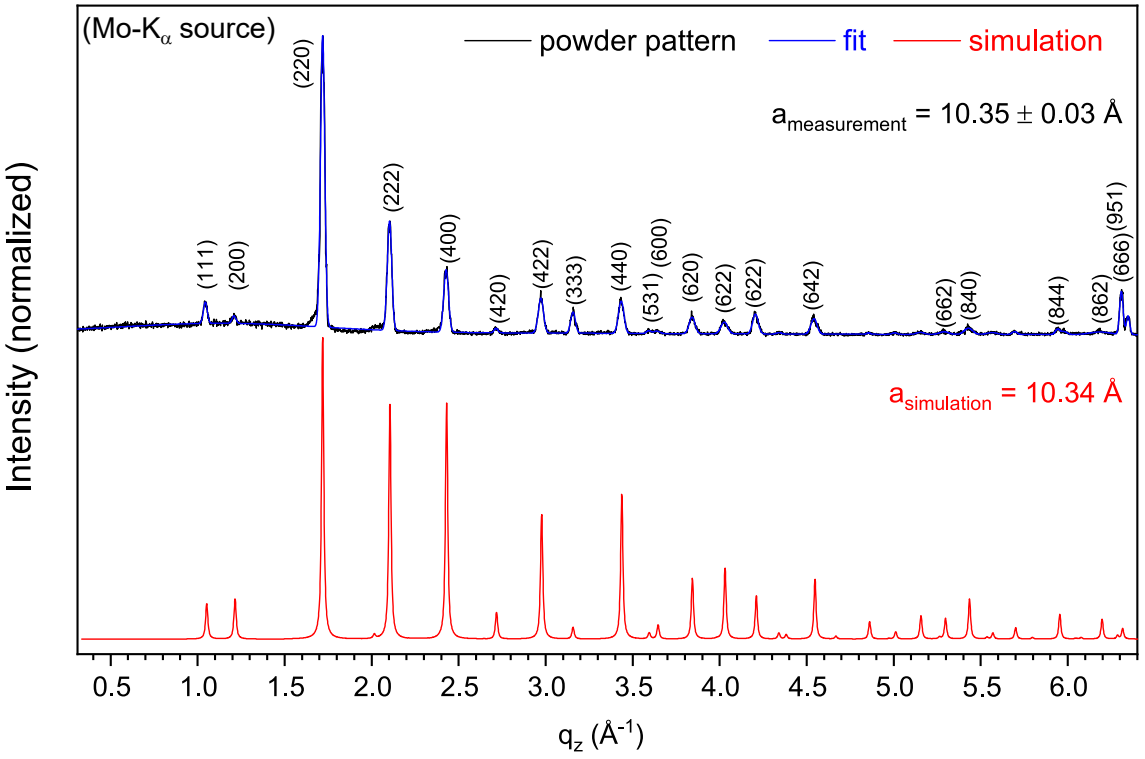

Figure 6.2: Powder, fitted and simulated XRD pattern for $Cs_2NaFeCl_6$ showing a phase-pure growth of $Cs_2NaFeCl_6$ crystals and good agreement of the lattice constant with the simulated XRD pattern. Reproduced from [210] with permission from Wiley VCH GmbH.

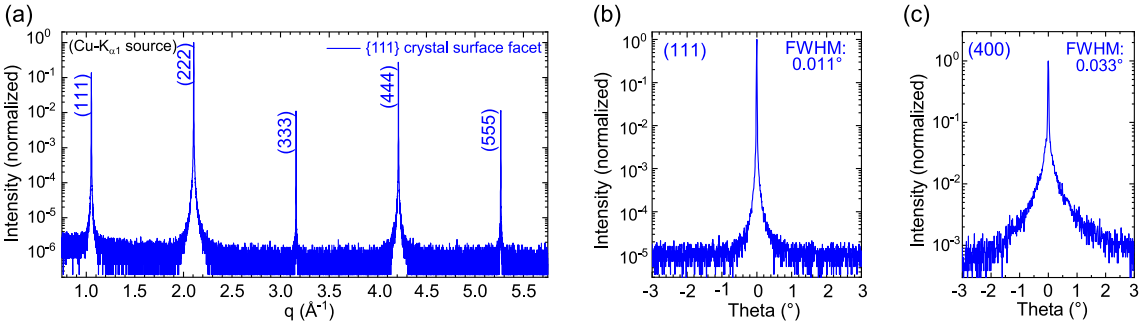

Figure 6.3: a) Out-of-plane XRD measurement on {111} crystal surface facet and b) corresponding rocking scan of the (111) direction and c) rocking scan of the (400) direction of a $Cs_2NaFeCl_6$ single crystal. Reproduced from [210] with permission from Wiley VCH GmbH.

In addition to the powder XRD, crystal structure analysis performed at RT verifies the single crystallinity of the grown crystals and the obtained lattice constant of 10.39 Å. Furthermore, out-of-plane XRD and rocking scans were conducted to gain more information about the quality of the grown crystals, which are shown in Figure 6.3a. From the out-of-plane XRD pattern, it is clear that the crystal only shows Bragg reflexes belonging to the {111} peak series, proving that no other Bragg reflexes can be found on

the crystal surface. Moreover, the {111} peak series shows narrow peaks observable up to the fifth order. Those results allow the conclusion of crystal growth along the [111] direction of the unit cell and indicate a single crystalline growth. To verify the quality of the crystal in more detail, rocking scans of the (111) and (400) reflexes were conducted, which are shown in Figure 6.3b and c. The rocking scans revealed single, narrow and very sharp peaks with full width at half maximums below 0.04 °. Therefore, a low mosaicity is suggested and one can finally conclude that the controlled cooling technique results in high-quality and phase-pure $Cs_2NaFeCl_6$ crystals.
To gain an understanding of the crystal morphology, the next step was to draw a 3D model of a $Cs_2NaFeCl_6$ crystal. The model served as an orientation to assign the crystal surface facets, which were determined in reflectometry. A total of four different facets were measured which are shown in Figure 6.4.

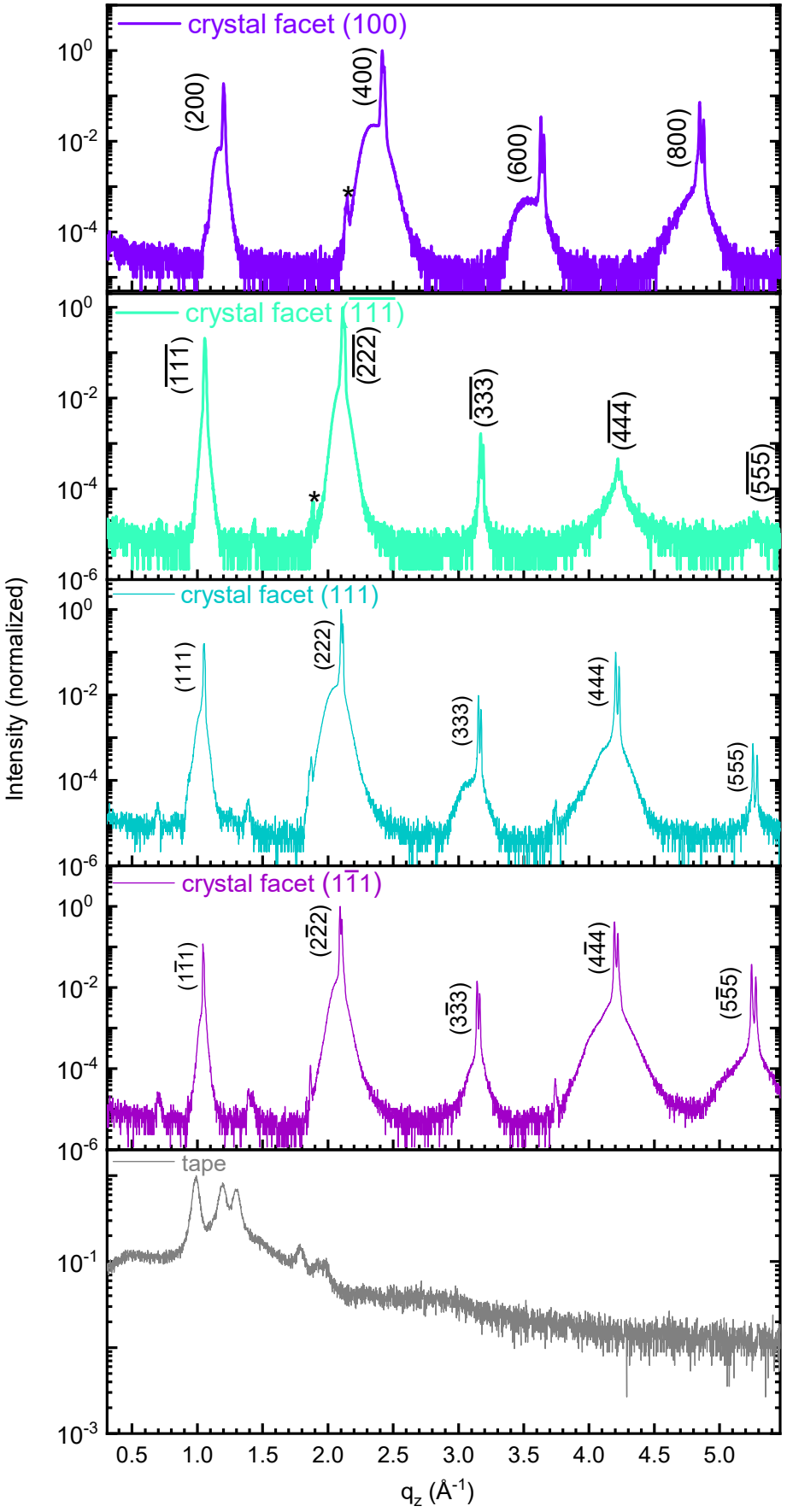

Figure 6.4: XRD patterns of the different crystal surface facets. The asterisks mark the peaks that can be assigned to the adhesive tape of the sample holder. Reproduced from [210] with permission from Wiley VCH GmbH.

The facets of the contact surface in the growth vessel as well as the "free" surfaces grew along the [111] direction and showed the shape of hexagons of different size ratios. The measurement of another crystal surface showed the shape of a rectangle grown in the [100] direction. Using these results and counting the total of 14 crystal surfaces, the eight hexagonal surfaces were assigned to the [111] direction and the six rectangular surfaces to the [100] direction.

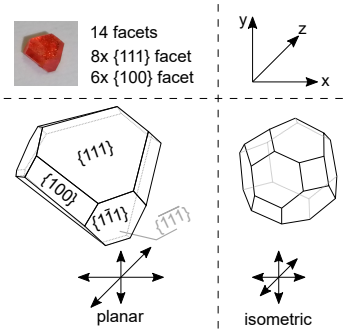

Figure 6.5: 3D illustration of a $Cs_2NaFeCl_6$ truncated octahedron with determined crystal surface facets. Reproduced from [210] with permission from Wiley VCH GmbH.

Concerning the crystal habit, the examined $Cs_2NaFeCl_6$ crystal agrees with that of a regular truncated octahedron (Figure 6.5). Comparing both crystal models in terms of habit, one can assume an isometric one for the regular model since the growth velocity is constant in all three spatial directions x, y and z, symbolized by the arrows in Figure 6.5. However, this is not the case for $Cs_2NaFeCl_6$. Here, a planar growth is assumed, since the growth in x and z directions seems to be preferred over the y-direction. This is an interesting aspect which seems to be independent of the perovskite crystal growth technique and has also been observed for lead-halide perovskite crystals such as $MAPbI_3$. [203]

6.4 Phase transition, spin properties and bandstructure of $Cs_2NaFeCl_6$

To further investigate temperature-dependent changes of the crystal structure caused by phase transitions in the material, EPR measurements were performed as the next step. EPR allows to directly address the spin of the Fe^{3+} and thus predict their environment.[213] An EPR spectrum of $Cs_2NaFeCl_6$ at RT is depicted in Figure 6.6a. Note that the signal drawn in red shows no significant features and can thus be described by the derivative of a simple Lorentzian (dashed line). This is consistent with a spin $S = \frac{1}{2}$ or $S = \frac{5}{2}$ with a zero-field splitting (ZFS) of $D = 0$, which are both appropriate candidates for Fe^{3+}.[202] It was already demonstrated for $Cs_2AgBiBr_6$ that the environment, given by the lattice structure, has a direct influence on ZFS.[213] Thus, for a $ZFS = 0$ a cubic and for a $ZFS > 0$ a tetragonal crystal structure is present. Since the stoichiometry and the crystal structure of $Cs_2NaFeCl_6$ is identical to $Cs_2AgBiBr_6$, one can apply the

same approach to investigate possible phase transitions of $Cs_2NaFeCl_6$ at low temperatures. Assuming a spin of $S = \frac{5}{2}$, as will later be confirmed by DFT calculations, the RT measurement suggest the cubic crystal structure of the previously shown XRD data. In order to identify potential phase transitions, the sample was cooled down to 4 K, as shown in Figure 6.6b. In the entire temperature range, the EPR signal can always be fitted with the derivative of a simple Lorentzian, which consistently gives strong indications for a cubic structure of the crystal. In contrast to $Cs_2AgBiBr_6$, no phase transition can be identified when a spin $S = \frac{5}{2}$ is assumed. DFT calculations within the localized

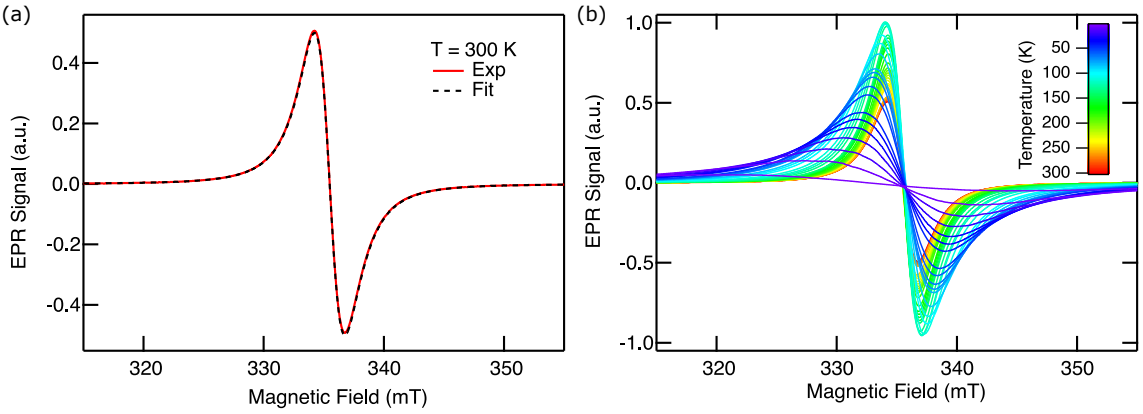

Figure 6.6: a) EPR spectrum of $Cs_2NaFeCl_6$ at RT consistent with a spin of $S = \frac{1}{2}$ or $S = \frac{5}{2}$ (with $D = 0$). b) EPR spectra in the temperature range from 4 K-300 K show a cubic structure without any phase transitions, if $S = \frac{5}{2}$ is assumed. Reproduced from [210] with permission from Wiley VCH GmbH.

spin-density approximation (LSDA) were conducted in order to verify the most stable spin configuration and to elucidate the electronic structure.[204] As the EPR results hint at indistinguishable total spin states of either $\frac{1}{2}$ or $\frac{5}{2}$, both phases were optimized and relaxed with respect to atomic positions and cell parameters. The relaxation calculations reveal a significantly better estimation of the $[FeCl_6]^{3-}$ octahedral geometry for the high spin state compared to the experimental single crystal data and a lower ground state energy, as shown in Table 6.2, hinting at the fivefold unpaired electrons in the d-orbital of Fe (spin state $\frac{5}{2}$) being the more favourable configuration. Furthermore, Hubbard correction U was employed to correctly describe the localized d-subshell orbitals in Fe^{3+}, employing a factor of U =4 eV as shown in Table 6.2.[208]

	Exp. (RT)	**Low Spin** $U = 0$eV	**Low Spin** $U = 4$eV	**High Spin** $U = 0$eV	**High Spin** $U = 3$eV	**High Spin** $U = 4$eV	**High Spin** $U = 5$eV
Fe-Cl Å	2.392	2.321	2.422	2.430	2.439	2.445	
Cs-Cl Å	3.661	3.637	3.670	3.773	3.727	3.732	3.736
Na-Cl Å	2.778	2.812	2.855	2.835	2.833	2.832	2.831
Unit cell Å	7.311	7.321	7.321	7.434	7.443	7.454	7.462
Energy [Ry]	-	-749.260	-749.034	-749.331	-749.152	-749.207	-749.178

Table 6.2: Unit cell parameters and ground state energy of $Cs_2NaFeCl_6$ obtained by DFT-PBE (+U) depending on the spin state and U value

The PBE+U band structures for the spin-up and spin-down cases for the suggested high-spin conformation are shown in Figure 6.7a and b, respectively. It can be seen that the electronic structure is completely spin-polarized around the Fermi-level.
The spin-up band structure exhibits a direct and insulating band gap of 4.5 eV located

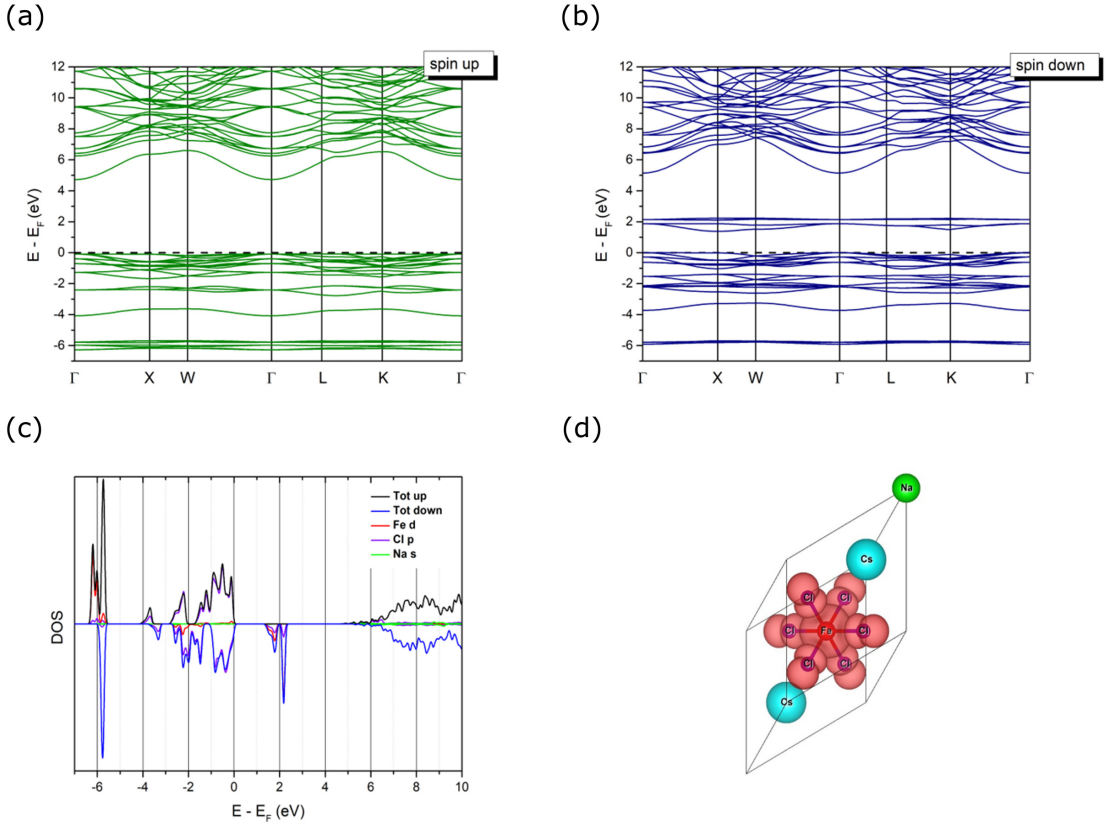

Figure 6.7: a) Spin-up and b) spin-down polarized band structures of $Cs_2NaFeCl_6$ (spin state = $\frac{5}{2}$), with the Fermi energy set to zero, calculated with DFT-PBE (+U) (= 4 eV). c) Total and projected density of states for spin-up (positive) and -down (negative) with orbital contributions of Cl-p/Fe-d/Na-s. d) Visualization of the spin density in the primitive unit cell (red: spin-up, iso value: 0.0011823). Reproduced from [210] with permission from Wiley VCH GmbH.

at the Γ point in the center of the Brillouin zone. Note that the estimation of the band

gap magnitude by DFT-PBE is known to be flawed and therefore should only be treated as a rough estimate. The valence band maximum (VBM) is flat and degenerate, hinting at high effective masses for the holes, whereas the conduction band maximum is more dispersed, suggesting smaller values for the electrons. The orbital contributions for the frontier bands are depicted in Figure 6.7c, showing that the character of the VBM is dominated by Fe-d and Cl-p orbitals. The CBM consists mostly of Na-s and Cl-p contributions. This transition is opposed to common $A_2B(I)B(III)X_6$ double perovskites like $Cs_2AgBiBr_6$, where the trivalent bismuth and halide atoms form the conduction band (CB) and the monovalent silver-halide bonds govern the CB character.[214] The band structures and density of states (DOS) for both spin cases without Hubbard correction are further depicted in Figure 6.8 and Figure 6.9.

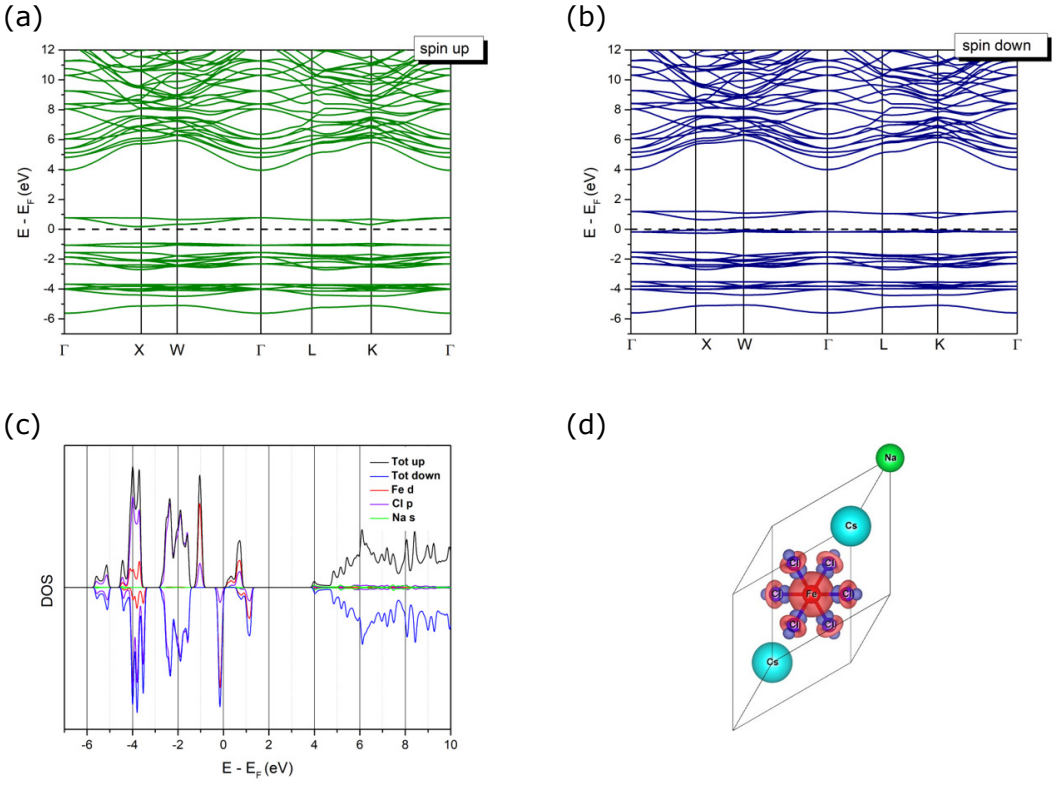

Figure 6.8: a) Spin-up and b) spin-down polarized band structures of $Cs_2NaFeCl_6$ (spin state $\frac{1}{2}$ with the Fermi energy set to zero, calculated with DFT-PBE. c) Total and projected density of states for spin-up (positive) and down (negative) with orbital contributions of Cl-p/Fe-d/Na-s. d) Visualization of the spin density in the primitive unit cell (red: spin up, blue: spin down, iso-value: 0.0011823). Reproduced from [210] with permission from Wiley VCH GmbH.

As expected, the electronic structure is drastically influenced by the different spin configurations as seen in Figure 6.8 (low spin) and Figure 6.9 (high spin). For the low spin configuration in Figure 6.8, both spin-up and spin-down band structures exhibit

semiconducting character, while the high-spin calculations yield the same results as with the PBE+U approach, showcasing insulating character for spin-up and semiconducting for spin-down. Interestingly, the VBM demonstrates partial Fe-d character for the band structures without Hubbard correction. Furthermore, the states for the high-spin spin-down case shift under the Fermi level when treated with the PBE approach, in contrast to the Hubbard-corrected band structure. The unoccupied states over the Fermi level for PBE+U also demonstrate favored electronic localization, which is expected because of the better treated on-site electron-electron interaction.

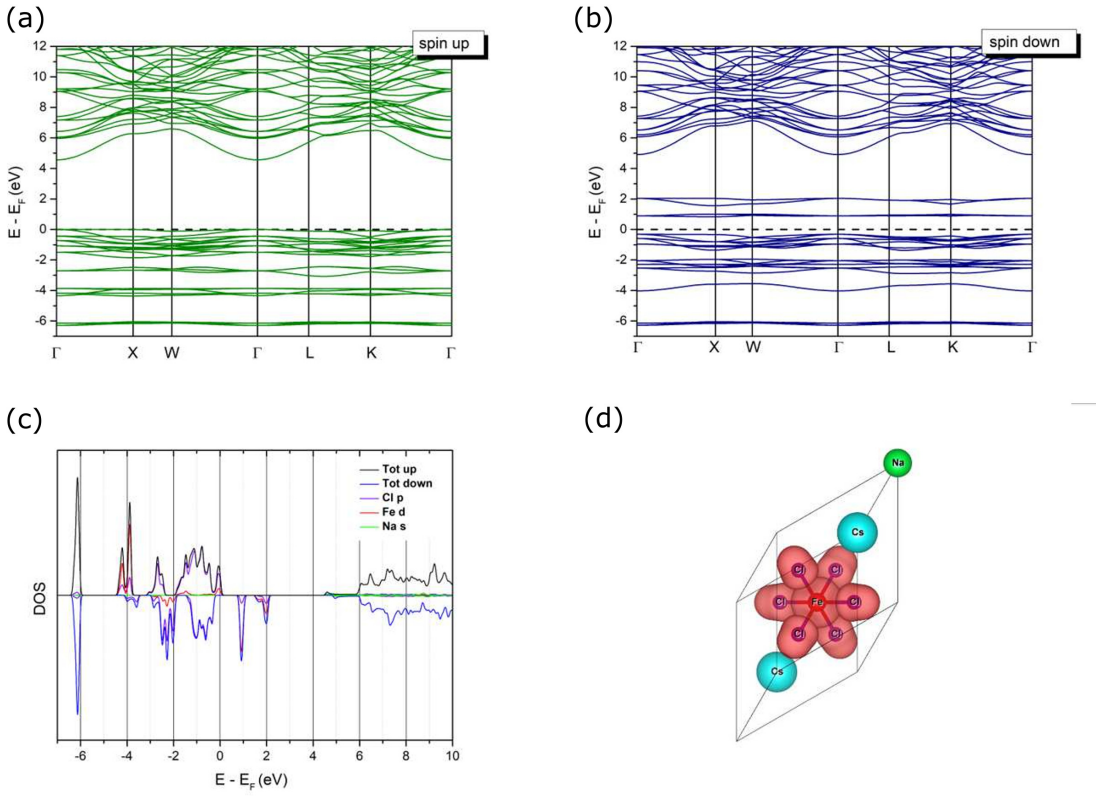

Figure 6.9: a) Spin-up and b) spin-down polarized band structures of $Cs_2NaFeCl_6$ (spin state $\frac{5}{2}$ with the Fermi energy set to zero, calculated with DFT-PBE. c) Total and projected density of states for spin up (positive) and down (negative) with orbital contributions of Cl-p/Fe-d/Na-s. d) Visualization of the spin density in the primitive unit cell (red: spin up, iso-value: 0.0011823)Reproduced from [210] with permission from Wiley VCH GmbH.

The spin-down band structure has semiconducting character with an indirect band gap of around 1.4 eV with the VBM at the Γ point and the CBM at the X point in the Brillouin zone, together with a direct transition located only 30 meV under the VBM. For this case, the VB is mostly flat and highly degenerate, with the states above the Fermi

level consisting of Fe-d and Cl-p contributions and the VB made up of Cl-p states, similar to previously reported double perovskite oxides.[215]

6.5 Optical properties of $Cs_2NaFeCl_6$

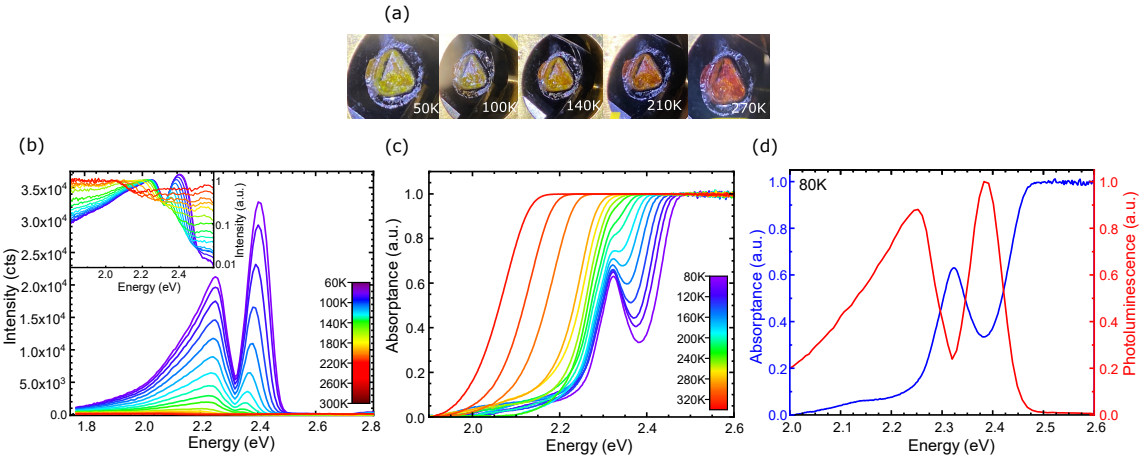

Figure 6.10: a) Photographs of the temperature-dependent color change from red (270 K) to yellow (50 K) of $Cs_2NaFeCl_6$ single crystals. b) Steady-state photoluminescence of the $Cs_2NaFeCl_6$ single crystal shows that photoluminescence of the crystals can only be observed at low temperatures. The inset shows the normalized PL on a logarithmic scale. c) Temperature-dependent absorptance shows an additional absorption peak for low temperatures. d) Absorption and emission spectra of $Cs_2NaFeCl_6$ crystal at 80 K. Reproduced from [210] with permission from Wiley VCH GmbH.

After gaining information about the structural properties and the band structure of $Cs_2NaFeCl_6$, the optical properties of the material were studied in the following section. Therefore, temperature-dependent photoluminescence and transmission studies were performed on the $Cs_2NaFeCl_6$ crystal. By lowering the temperature, a continuous color change of the grown crystal from red at RT to yellow at 50 K could be observed, as shown in Figure 6.10a. This effect is reversible and has been reported for $Cs_2NaFeCl_6$ crystals recently, where this thermochromic behavior was ascribed to an order-disorder transition in the material.[201]

Additionally, temperature-dependent PL measurements were conducted, as surprisingly no photoluminescence has been reported for this material so far. Figure 6.10b shows hardly any luminescence at the bandgap of 2.07 eV when measured at RT. However, upon cooling the crystal, increasing luminescence shifting towards higher energy could be seen. Furthermore, the inset of Figure 6.10b shows a blue-shift and narrowing of the observed peak at around 2.1 eV when the temperature is reduced.

At about 140 K, it seems that either the PL peak splits into two individual peaks or a

second peak appears at 2.4 eV, which strongly increases its intensity by decreasing temperature. One can also notice that the dip between these two peaks is at around 2.32 eV and slightly blue shifting. The rise of additional PL peaks has also been reported for the lead halide perovskite $MAPbI_3$ and was related to a phase transition from a tetragonal phase to the orthorhombic phase.[216] However, the previously presented EPR measurements showed no evidence of a structural phase transition for this material and consequently a phase transition as the cause for the rise of the additional PL at 2.4 eV can be excluded.

In order to explain the blue-shift of the PL spectra as well as the rise of the second PL peak at higher energies, temperature-dependent absorption measurements were conducted, which can be found in Figure 6.10c. At RT, the absorption edge can be observed at around 2.05 eV, which is consistent with bandgap values reported in literature for $Cs_2NaFeCl_6$.[89], [201] When the temperature is decreased, a strong blue-shift of the absorption onset was found, suggesting an increase of the bandgap at low temperatures. This effect has also been previously reported for temperatures ranging from 450 K to 260 K.[201] Additionally, Figure 6.10c shows a second pronounced absorption peak at 2.32 eV for temperatures below 140 K.

For further evaluation, one can superimpose the two graphs for 80 K, as shown in Figure 6.10d. Consequently, one finds that the observed PL from the crystal seems to be partly reabsorbed by the peak visible at 2.32 eV in the absorption spectra. This indicates that reabsorption is leading to the visible dip in the PL at 2.32 eV shown in Figure 6.10b and ultimately leading to an apparent second PL peak at higher energies. Additionally, it can be seen in Figure 6.10d that PL and absorptance overlap, which leads to a strong decrease in PL intensity at energies greater than 2.4 eV.

The strong absorption at RT of $Cs_2NaFeCl_6$ in combination with the weak PL indicates that nonradiative recombination processes dominate even in a high-quality and phase-pure crystal. Since the PL increases with decreasing temperature, one can assume that recombination in the material is mainly first order (e.g. traps, defects) at RT, with these being "frozen" out at lower temperatures. A similar effect was observed for lead-halide perovskites, namely that lowering the temperature causes a decrease in the monomolecular recombination rate while simultaneously, the bimolecular recombination rate is increasing.[217], [218] Hence, the measured PL signal is increasing.[217], [218]

To further investigate the origin of the dip in PL as well as the additional absorption peak at 2.3 eV which arises at low temperatures, the excitonic properties of $Cs_2NaFeCl_6$ were investigated by means of Elliot's theory.[219] Although the peak in the absorption spectra only varies slightly when reducing the temperature, one can still treat this

peak as an excitonic feature as has been shown for $Cs_2AgBiBr_6$ in the past.[65] Wright et al. found that in $Cs_2AgBiBr_6$ the shift of the absorption peak is hardly visible. This is caused by a temperature-dependent change of the exciton binding energy in correlation with the bandgap of the material.[65]
As a consequence, the data was fitted according to the model of Elliot to analyze the measured absorption spectra and extract the band gap energy E_g, exciton binding energies E_B as well as broadening parameters of the absorption peak at 2.3 eV.[219] However, in order to account for the steep increase in the absorption after the excitonic contribution, another parameter for the direct interband transition described by a second bandgap E_{g2} was added.

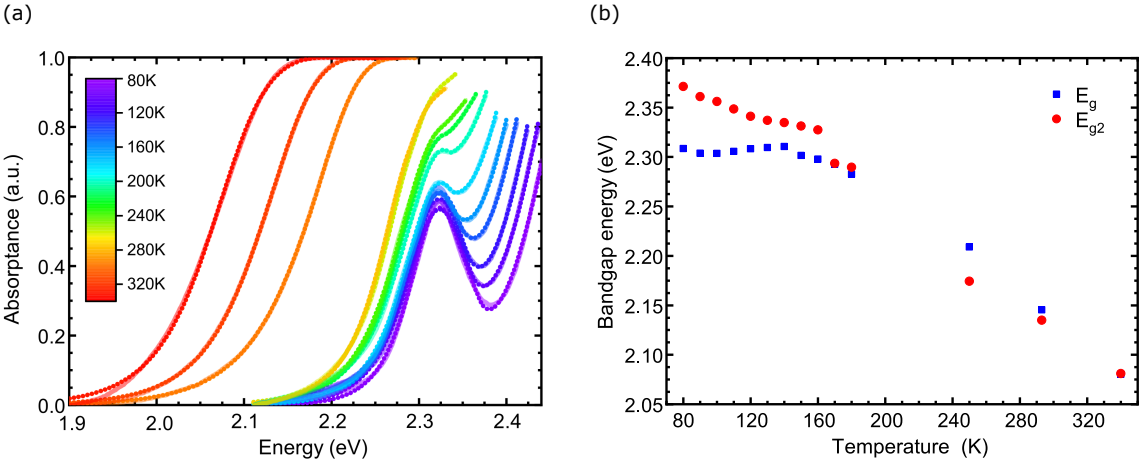

Figure 6.11: a) Measured absorptance (solid line) together with obtained Elliot fits (dotted lines) for temperatures between 80 K and 340 K. b) Extracted bandgap energies from the fits for the measured temperature range. Reproduced from [210] with permission from Wiley VCH GmbH.

Figure 6.11a shows the resulting Elliot fits together with the measured absorption data. Note that the fits for 190 K and 200 K are not included as they did not converge during the fitting routine. It is clear that the obtained fits match very well with the experimental results. Consequently, this allowed for a closer investigation of the temperature dependence of the bandgap of $Cs_2NaFeCl_6$ crystals as shown in Figure 6.11b. One then finds that within the Elliot model the bandgaps E_g and E_{g2} also shift towards higher energies as soon as the temperature decreases. This behavior is expected for semiconducting materials like Si, SiC, Ge, GaAs and InP and can be described by Varshni's empirical expression.[220] The obtained values for $\frac{dE}{dT}$ can be found in Table 6.3.

$$E_g(T) = E_g(0) - \frac{\alpha T^2}{T+\beta} \approx E_g(0) + \frac{dE_g}{dT} T \tag{6.1}$$

Temperature [K]	$\frac{dE_g}{dT}\left[\frac{\mu eV}{K}\right]$	$\frac{dE_g}{dT}\left[\frac{\mu eV}{K}\right]$
80 – 350K	-0.87	-1.17
250 – 350K	-1.43	-1.04
150 – 350K	-1.18	-1.35

Table 6.3: Temperature-dependent change of the bandgap energy $\frac{dE_g}{dT}$ calculated by Varshni's empirical expression for different temperature ranges

Additionally, the temperature dependence of the exciton binding energy for $Cs_2NaFeCl_6$ was extracted using the Elliot model. It was found that the exciton binding energy at 80 K can be estimated to be approximately 20 meV, whereas hardly any excitons are present at RT as is shown in Figure 6.12a. The very low exciton binding energy of $Cs_2NaFeCl_6$ is a major advantage compared to the conventional $Cs_2AgBiBr_6$, which has exciton binding energies of approximately 268 meV at RT.[70] A slight increase in the exciton binding energy with decreasing temperature has also been observed in the past for other perovskites like $MAPbI_3$ and triple-cation lead-based perovskites.[221] Due to the very low exciton binding energy at RT of <10 meV, excitons dissociate into free carriers just by the thermal energy $k_B T$ and therefore presumably only free carriers are present in $Cs_2NaFeCl_6$. However, the fact that no photoluminescence has been observed at RT strongly hints towards nonradiative recombination being the main recombination pathway of charge carriers in $Cs_2NaFeCl_6$ at RT.
Furthermore, the broadening parameter Γ of the excitonic contribution in the absorption spectra was analyzed and is shown in Figure 6.12.

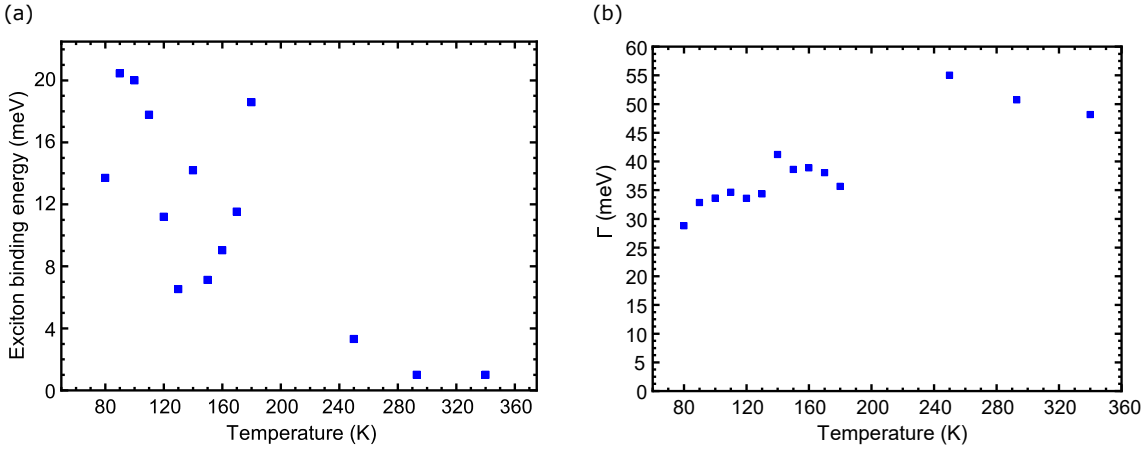

Figure 6.12: Evolution of a) exciton binding energy and b) broadening parameter Γ depending on temperature for $Cs_2NaFeCl_6$ crystals. Reproduced from [210] with permission from Wiley VCH GmbH.

One can observe that the broadening significantly increases when the temperature is increased from 80 K to 350 K. A linewidth broadening with increasing temperature is

expected and has also been observed previously for other perovskites such as $MAPbI_3$ and $Cs_2AgBiBr_6$.[216], [222]–[224] This broadening is usually associated with electron-phonon coupling in the material.[216], [222] Note that it is not possible to differentiate between the coupling of longitudinal optical phonons and acoustic phonons in the shown temperature range. However, the temperature dependence of the broadening parameter suggests that impurity scattering can be neglected in this material.[216] This is due to the fact that linewidth broadening caused by impurities should lead to a saturation of the linewidth at higher temperatures, which seems not to be the case for $Cs_2NaFeCl_6$.
[216]

6.6 Conclusion

In conclusion, this chapter presented a method to grow high-quality crystals of the new double perovskite $Cs_2NaFeCl_6$. XRF, EDX and ICP-OES have proven a nearly perfect stoichiometry whereas the successful growth of $Cs_2NaFeCl_6$ single crystals was verified by detailed X-ray studies. Furthermore, it was possible to assess the spin properties of the material and correlate them with their crystal structure by connecting DFT calculations with experimental data. It was found that the spin $\frac{5}{2}$ system $Cs_2NaFeCl_6$ has a cubic crystal structure and although the crystal changes its color from red to yellow upon cooling, no structural phase transition was observed. Additionally, optical measurements suggest that nonradiative recombination is dominant at RT. However, upon cooling, promising emission could be seen, together with reabsorption of emission by an additional excitonic state with low binding energy of only 20 meV. One can therefore conclude that although the emission of $Cs_2NaFeCl_6$ seems to be governed by nonradiative processes at RT, its low exciton binding energy, the promising emission at low temperatures and the reported high stability against thermal cycling[201] still indicate a potential application for thermochromic windows[201] or detectors and devices operating at low temperatures or in space.[225]

7 Summary

Although perovskite solar cells have reached very high efficiencies and are now able to compete with Si solar cells, the concerns regarding the toxicity of lead-halide based perovskites remain.[14], [45]–[48] Whilst studies have addressed leakage and degradation of lead-based devices and investigated different encapsulation techniques, the worries of applying materials, which are hazardous to the human health, could not be completely eliminated.[226]–[228] Additionally, it has been shown that lead is not only dangerous to humans but also endangers the ecosystem as even plants showed signs of lead-poisoning.[47], [48]

Furthermore, lead-halide based perovskites still suffer from rather poor stability, which also poses an additional threat when thinking about the commercialization of those perovskites.[42], [43] Hence, it is necessary to think about new lead-free perovskite materials in order to tackle the problems of stability as well as the toxicity of lead.

Therefore, lead-free double perovskites have been suggested as a possible material class to replace lead-halide perovskites in the future.[17] In order to investigate the physical properties of lead-free double perovskites, single crystal growth provides a good opportunity to study such materials under reproducible conditions.[17], [18], [20], [229] Although thin films are usually used for solar cells, it has been shown that only slight variations in the precursor stoichiometry or fabrication conditions can alter the properties of the thin film.[73]–[75] Crystal growth however is more unsusceptible against stoichiometric changes as it mostly depends on the binding enthalpy and free enthalpy of the respective material. Therefore, it can be used to understand the impact of different growth conditions on the physical properties of the perovskite without risking a stoichiometric alteration.[19]–[21]

This thesis aims towards understanding the physical properties of the lead-free double perovskites $Cs_2AgBiBr_6$ and $Cs_2NaFeCl_6$ by crystal growth and thin film synthesis. A special focus of this thesis was set on understanding the structure-property relationship of fabrication parameters such as growth temperature and growth methods for single crystals as well as stoichiometric alterations and their impact on solar cell performance. Hence, **Chapter 5** is divided into two parts. In the first part, $Cs_2AgBiBr_6$ single crystals are grown by controlled cooling and slow evaporation in order to study

the effects of growth temperature on the material properties. It was demonstrated that fast crystal growth from organic solvents leads to an increase in disorder, stemming from structural defects, which cause tailstates in the material. As tailstates have been shown to lead to additional nonradiative recombination losses in a device, slow crystal growth provides a solution to reduce tailstates in $Cs_2AgBiBr_6$. It was shown that low growth temperatures and hence slow crystallization of the double perovskite decreases the amount of tailstates in the material and can therefore also decrease the nonradiative losses when $Cs_2AgBiBr_6$ is applied as the absorber layer in a device.
Secondly, stoichiometric alterations of $Cs_2AgBiBr_6$ were investigated. However, as it is difficult to vary the composition of a single crystal, thin films were fabricated for this study. Consequently, thin films with slight variations of AgBr and $BiBr_3$ were fabricated and characterized using X-ray techniques as well as optical measurements such as PL and TRMC. Here, it was found that slight AgBr excess and $BiBr_3$ deficiency will improve the orientation of the thin film crystallites as well as increase steady-state PL and PLQY. Additionally, a longer TRPL decay hinted towards smaller trap densities in the thin films. Furthermore, TRMC studies showed that charge carrier mobilities can also be affected by the thin film composition. A combination of AgBr excess and $BiBr_3$ deficiency yielded the highest charge carrier mobilities. Due to the improvement of the optical properties (e.g. PLQY, TRPL and steady-state PL) together with increased charge carrier mobilities, direct consequences on the device performance were observed. Although the efficiencies reached by $Cs_2AgBiBr_6$ are still rather low, using a stoichiometric alteration led to improvement of the J_{sc} as well as FF and PCE of the device. Hence, it was shown in this chapter that the growth conditions significantly impact the recombination losses in $Cs_2AgBiBr_6$ and therefore have to be considered and optimized. It was also found that the transport properties of $Cs_2AgBiBr_6$ are improved along the (001) axis of the unit cell. In order to reach this improved crystallization, working in an AgBr excess and $BiBr_3$ deficient regime is necessary.
Although this thesis provided optimization techniques to control crystallization in thin films and reduce recombination losses by studying single crystals, $Cs_2AgBiBr_6$ still faces major challenges. Those challenges include the fast localization of charge carriers after optical excitation, poor charge carrier selectivity of the contact materials, disorder affecting the recombination, low charge carrier diffusion lengths and high amount of electron trap states as well as high exciton binding energies.[65], [69], [70], [81], [199] Additionally, the elements Ag, Bi, as well as Br do not exist in abundance on earth.[200] Accordingly, although $Cs_2AgBiBr_6$ is a lead-free and non-toxic material, new challenges can be expected in the future concerning the availability of the precursor materials.
Consequently, **Chapter 6** is proposing a new and earth-abundant lead-free double per-

ovskite: $Cs_2NaFeCl_6$. Single crystals were grown from this double perovskite in order to study its physical properties. It was demonstrated by single crystal XRD that $Cs_2NaFeCl_6$ crystals can be grown with very high quality. Although this material has an indirect bandgap of roughly 2 eV, an additional direct transition was found lying close to the VB maximum. Furthermore, EPR and DFT suggested a spin of S=$\frac{5}{2}$ for $Cs_2NaFeCl_6$. Using EPR, no structural phase transition could be identified for low temperatures although the material shows a thermochromic color change when the temperature is decreased. Optical studies then proposed that although nonradiative losses seem to be dominant at room temperature, a photoluminescence signal could be detected for low temperatures. Together with temperature dependent absorptance, it was possible to identify an excitonic contribution in the PL and absorption data. However, Elliot fits suggested that the exciton binding energy, even at low temperatures, is rather small. This makes $Cs_2NaFeCl_6$ a good candidate for low temperature and magnetic applications but also shows the possibility of using $Cs_2NaFeCl_6$ in solar cells for applications in space.

To sum up, the presented work in this thesis contributes to a deeper understanding of the interplay between fabrication and its impact on the physical properties of lead-free double perovskites. Additionally, it tackles the ongoing issues of $Cs_2AgBiBr_6$ by providing another lead-free double perovskite which is environmentally friendly and non-toxic as well as more earth-abundant compared to $Cs_2AgBiBr_6$. Besides, $Cs_2NaFeCl_6$ shows only low exciton binding energies and thereby solves one of the intrinsic issues of $Cs_2AgBiBr_6$.

Although both of the studied materials in this thesis are rather new and many of their properties are not yet understood, lead-free double perovskites are fascinating, yet complicated systems which enable researchers worldwide to design cheap, earth-abundant and environmentally friendly materials. Like this, it might be possible to combine the astonishing properties of lead-halide based perovskites and the remarkable stability of Si by designing new lead-free double perovskites. Although, $Cs_2AgBiBr_6$ might never reach efficiencies higher than 8 %[230], understanding its challenges as a reference material will lead to the possibility of more targeted material design in the future, as could be shown exemplary with $Cs_2NaFeCl_6$ and hence further opening the material space of non-toxic solar cells for commercialization in the future.

Zusammenfassung

In den letzten Jahren erreichten Perowskit Solarzellen sehr hohe Effizienzen, sodass Perowskite inzwischen mit Silizium Photovoltaik konkurrieren können.[14] Dennoch

bleiben Bedenken aufgrund der Bleitoxizität im Bereich der Perowskitforschung bestehen.[45]–[48] Obwohl verschiedene Studien das Austreten des giftigen Bleiiodids untersucht haben und versucht wurde, dafür unterschiedliche Verkapselungen zu entwickeln, konnten die anfänglichen Bedenken nicht komplett ausgeräumt werden.[226]–[228] Die Tatsache, dass giftige Materialien verwendet werden, welche nicht nur gesundheitsgefährdend für Menschen, sondern auch eine Bedrohung für das Ökosystem darstellen, ist nach wie vor ein erheblicher Kritikpunkt an bleihaltigen Perowskitmaterialien.[47], [48]
Hinzu kommt, dass bleihaltige Perowskite zwar hohe Effizienzen erreichen, jedoch bisher keine Langzeitstabilität erreicht werden konnte.[42], [43] Dies dürfte die Kommerzialisierung dieser Perowskitmaterialien erschweren.[42], [43]
Daher ist es umso wichtiger, die intrinsischen physikalischen Eigenschaften dieser Materialien zu erforschen. Um dies zu tun, können Einkristalle gezüchtet werden, da die Wachstumsbedingungen der Einkristalle sehr gut reproduzierbar sind. Somit können Veränderungen der physikalischen Eigenschaften aufgrund unbeabsichtigter Variationen der Stöchiometrie oder der Herstellungsparameter vermieden werden.[17], [18], [20], [73]–[75], [229] Da Kristallwachstum vor allem von der Bindungsenthalpie der einzelnen Ionen und der freien Enthalpie abhängt, sind unbeabsichtigte Änderungen der Stöchiometrie deutlich unwahrscheinlicher als in Dünnfilmen. Dadurch bieten sich Kristalle besonders gut an, um den Einfluss von Wachstumsparametern auf die physikalischen Eigenschaften von Kristallen zu untersuchen, ohne dabei eine Stöchiometrievariation befürchten zu müssen.[19]–[21]
Die hier vorgelegte Arbeit trägt dazu bei, die physikalischen Eigenschaften von $Cs_2AgBiBr_6$ und $Cs_2NaFeCl_6$ besser zu verstehen. Dafür wurden sowohl Einkristalle als auch Dünnfilme hergestellt und charakterisiert. Ein Fokus dieser Arbeit war es, das Zusammenspiel von veränderten Wachstumsbedingungen und den daraus resultierenden strukturellen und optischen Eigenschaften besser zu verstehen. Ebenso wurde der Einfluss von stöchiometrischen Veränderungen auf die Effizienzen von Solarzellen untersucht. **Kapitel 5** ist daher in zwei thematische Bereiche aufgeteilt. Zuerst wurden $Cs_2AgBiBr_6$ Einkristalle durch Verdampfen und kontrolliertes Abkühlen gewachsen. Durch die unterschiedlichen Wachstumstemperaturen der beiden Methoden konnte der Effekt von Temperatur auf die physikalischen Eigenschaften von $Cs_2AgBiBr_6$ untersucht werden. Es hat sich gezeigt, dass besonders schnelles Kristallwachstum aus organischen Lösungen die Unordnung im Materialsystem erhöht. Diese Unordnung stammt von strukturellen Defekten, welche zusätzliche Zustände innerhalb der Bandlücke verursachen. Diese sogenannten "tailstates"konnten in der Vergangenheit mit Rekombinationsverlusten in Solarzellen in Zusammenhang gebracht werden. Im ers-

ten Teil des fünften Kapitels konnte eine Lösungsstrategie angeboten werden um "tail-statesïn $Cs_2AgBiBr_6$ zu reduzieren, wenn dieses Doppelperowskit als Absorbermaterial in Solarzellen verwendet wird.
Anschließend wurden stöchiometrische Variationen in $Cs_2AgBiBr_6$ näher untersucht. Da die stöchiometrische Variation von Einkristallen nur schwer zu realisieren ist, wurden hierfür Dünnfilme herangezogen. Diese Dünnfilme wurden mit leichtem AgBr Überschuss und gleichzeitig leichtem $BiBr_3$ Defizit hergestellt und anschließend sowohl mittels Röntgenanalyse, als auch mittels optischer Methoden wie PL, PLQY und TRMC untersucht. Es stellte sich heraus, dass ein AgBr Überschuss und gleichzeitiges $BiBr_3$ Defizit zu einer verbesserten Orientierung und Kristallinität des Dünnfilms führt. Zusätzlich konnten die optischen Eigenschaften verbessert werden. Die beobachtete erhöhte PL und PLQY sowie ein längerer TRPL Zerfall deuteten auf eine verringerte Anzahl an Fallenzuständen im Material hin. Ebenso zeigte sich in TRMC eine erhöhte Ladungsträgermobilität. Die Verbesserung der optoelektronischen Eigenschaften durch die leichte Veränderung der Filmkomposition hatte ebenso Auswirkungen auf die Solarzellparameter. Es konnte gezeigt werden dass $Cs_2AgBiBr_6$ mit AgBr Überschuss und gleichzeitigem $BiBr_3$ Defizit in Solarzellen sowohl höhere Kurzschlussströme und Füllfaktoren als auch höhere Effizienzen erreicht. Demnach konnte nicht nur ein Zusammenhang der Wachstumparameter auf die Rekombinationsverluste sondern ebenfalls ein signifikanter Einfluss der Stöchiometrie auf die Transporteigenschaften in $Cs_2AgBiBr_6$ nachgewiesen werden. Es stellte sich heraus, dass die Transporteigenschaften bei einer Orientierung des Films entlang der (001) Richtung verbessert werden kann. Hierfür ist jedoch die Arbeit in einer Umgebung mit AgBr Überschuss und gleichzeitigem $BiBr_3$ Defizit zwingend notwendig.
Diese Arbeit leistet einen Beitrag zur Optimierung von $Cs_2AgBiBr_6$ mittels der kontrollierten Kristallisation und zeigt Lösungswege auf, um die Rekombinationsverluste in $Cs_2AgBiBr_6$ zu vermindern. Dennoch zeigt die Literatur, dass $Cs_2AgBiBr_6$ einige Eigenschaften besitzt, welche in Solarzellen unerwünscht sind. Dazu zählen eine schnelle Lokalisation von Ladungsträgern nach deren Anregung, geringe Selektivität der verwendeten Kontakte in Solarzellen, strukturelle Unordnung welche die Ladungsträgerrekombination negativ beeinflusst, niedrige Ladungsträgerdiffusionslängen, eine hohe Dichte an Fallenzuständen sowie hohe Exzitonenbindungsenergien.[65], [69], [70], [81], [199] Ebenfalls muss angemerkt werden, dass $Cs_2AgBiBr_6$ zwar ungiftig und bleifrei ist, jedoch die Elemente Ag, Bi und Br auf der Erde nicht im Überfluss vorhanden sind.[200] Dies kann bei der Anwendung von $Cs_2AgBiBr_6$ als Absorbermaterial in der Zukunft zu Problemen führen, falls die benötigten Materialien nicht ausreichend vorhanden sind.

In **Kapitel 6** wird mit $Cs_2NaFeCl_6$ ein neues Doppelperowskit vorgestellt. $Cs_2NaFeCl_6$ zeichnet sich vor allem dadurch aus, dass es nicht nur bleifrei und nicht toxisch ist, sondern außerdem alle notwendigen Materialien auf der Erde reichlich vorhanden sind. Im Rahmen dieser Arbeit wurden hochwertige Einkristalle aus $Cs_2NaFeCl_6$ gezüchtet und die physikalischen Eigenschaften dieses Materialsystems analysiert. Obwohl auch $Cs_2NaFeCl_6$ eine indirekte Bandlücke von etwa 2 eV aufweist, konnte ein direkter Übergang nur 30 meV unterhalb des VB gefunden werden. Zusätzlich konnte mit Hilfe von EPR und DFT ein Spin von S=$\frac{5}{2}$ für $Cs_2NaFeCl_6$ nachgewiesen werden. Bei der Untersuchung der temperaturabhängigen strukturellen Eigenschaften konnte außerdem kein Phasenübergang des Systems bei tiefen Temperaturen festgestellt werden, obwohl $Cs_2NaFeCl_6$ thermochrome Farbveränderungen mit sinkender Temperatur aufweist. Die Untersuchung der optischen Eigenschaften zeigte eine starke Dominanz von nichtstrahlenden Rekombinationsprozessen bei RT. Es konnte jedoch bei tiefen Temperaturen Photolumineszenz nachgewiesen werden. Zusammen mit Messungen der temperaturabhängigen Absorption konnte außerdem ein exzitonischer Beitrag in der Absorption und der Photolumineszenz dieses Materials nachgewiesen werden. Daraufhin konnte mit Hilfe von Elliot Fits gezeigt werden, dass die Exzitonenbindungsenergie in $Cs_2NaFeCl_6$ selbst bei geringen Temperaturen sehr klein ist. Dies macht $Cs_2NaFeCl_6$ zu einem weiteren Kandidaten für Tieftemperatur- und magnetische Anwendungen. Ebenso zeigen die vielversprechenden optischen Eigenschaften auch die Möglichkeit der Anwendung von $Cs_2NaFeCl_6$ als Material für Solarzellen im Weltraum auf.
Die in dieser Arbeit präsentierten Ergebnisse tragen zu einem tieferen Verständnis des Zusammenspiels zwischen Herstellungsparametern und den physikalischen Eigenschaften von bleifreien Doppelperowskiten bei. Außerdem können mit Hilfe der Entwicklung von $Cs_2NaFeCl_6$ einige Probleme von $Cs_2AgBiBr_6$ abgeschwächt werden. Besonders die niedrige Exzitonenbindungsenergie von $Cs_2NaFeCl_6$ löst ein vorherrschendes intrinsisches Problem der Anwendung von $Cs_2AgBiBr_6$ in Solarzellen.
Obwohl beide hier präsentierten Materialien im Vergleich zu bleihaltigen Perowskiten neu und ihre physikalischen Eigenschaften noch nicht vollständig verstanden sind, sind bleifreie Doppelperowskite vielversprechende Materialsysteme. Sie bieten Wissenschaftlern die Möglichkeit, günstige und umweltfreundliche Materialien für die Anwendung in der Photovoltaik zu entwickeln. Ebenso bietet sich so die Möglichkeit, bleifreie Doppelperowskite zu entwickeln, die die Eigenschaften der bleihaltigen Perowskite mit der guten Stabilität von Si kombinieren. Obwohl gezeigt wurde, dass $Cs_2AgBiBr_6$ nur Effizienzen von maximal 8 % [230] erreichen kann, ist es wichtig, die limitieren-

den Faktoren von Doppelperowskiten zu verstehen, um in der Zukunft Materialien mit besseren physikalischen Eigenschaften entwickeln zu können.

Bibliography

[1] acatech – Deutsche Akademie der Technikwissenschaften e. V., Nationale Akademie der Wissenschaften Leopoldina, and Union der deutschen Akademien der Wissenschaften e. V., *Welche Auswirkungen hat der Ukrainekrieg auf die Energiepreise und Versorgungssicherheit in Europa?*, 2022. DOI: 10.48669/esys_2022-5. [Online]. Available: https://www.leopoldina.org/publikationen/detailansicht/publication/welche-auswirkungen-hat-der-ukrainekrieg-auf-die-energiepreise-und-versorgungssicherheit-in-europa-2022/ (visited on 11/01/2022).

[2] *Energieerzeugung*, 2022. [Online]. Available: https://www.destatis.de/DE/Themen/Branchen-Unternehmen/Energie/Erzeugung/_inhalt.html (visited on 10/24/2022).

[3] *Erneuerbare Energien in Zahlen*, 2022. [Online]. Available: https://www.umweltbundesamt.de/themen/klima-energie/erneuerbare-energien/erneuerbare-energien-in-zahlen#strom (visited on 10/24/2022).

[4] Dr. Harry Wirth, *Recent Facts about Photovoltaics in Germany*, 2021. [Online]. Available: https://www.ise.fraunhofer.de/en/publications/studies/recent-facts-about-pv-in-germany.html (visited on 10/24/2022).

[5] S. Bhattacharya and S. John, "Beyond 30% Conversion Efficiency in Silicon Solar Cells: A Numerical Demonstration", *Scientific reports*, vol. 9, no. 1, p. 12 482, 2019. DOI: 10.1038/s41598-019-48981-w.

[6] A. M. Ganose, C. N. Savory, and D. O. Scanlon, "Beyond methylammonium lead iodide: prospects for the emergent field of ns2 containing solar absorbers", *Chemical Communications*, vol. 53, no. 1, pp. 20–44, 2016. DOI: 10.1039/c6cc06475b.

[7] *Index zur Entwicklung des Strompreises* für Haushalte in Deutschland in den Jahren 1998 bis 2022*, 2022. [Online]. Available: https://de.statista.com/statistik/daten/studie/234370/umfrage/entwicklung-der-haushaltsstrompreise-in-deutschland/ (visited on 10/24/2022).

[8] S. R. Wenham and M. A. Green, "Silicon solar cells", *Progress in Photovoltaics: Research and Applications*, vol. 4, no. 1, pp. 3–33, 1996, ISSN: 1062-7995. DOI: 10.1002/(SICI)1099-159X(199601/02)4:1<3::AID-PIP117>3.0.CO;2-S.

[9] K. C. Nwambaekwe, V. S. John-Denk, S. F. Douman, P. Mathumba, S. T. Yussuf, O. V. Uhuo, P. I. Ekwere, and E. I. Iwuoha, "Crystal engineering and thin-film deposition strategies towards improving the performance of kesterite photovoltaic cell", *Journal of Materials Research and Technology*, vol. 12, pp. 1252–1287, 2021, ISSN: 22387854. DOI: 10.1016/j.jmrt.2021.03.047.

[10] P. Gao, M. Grätzel, and M. K. Nazeeruddin, "Organohalide lead perovskites for photovoltaic applications", *Energy & Environmental Science*, vol. 7, no. 8, pp. 2448–2463, 2014. DOI: 10.1039/C4EE00942H.

[11] P. Billen, E. Leccisi, S. Dastidar, S. Li, L. Lobaton, S. Spatari, A. T. Fafarman, V. M. Fthenakis, and J. B. Baxter, "Comparative evaluation of lead emissions and toxicity potential in the life cycle of lead halide perovskite photovoltaics", *Energy*, vol. 166, pp. 1089–1096, 2019, ISSN: 03605442. DOI: 10.1016/j.energy.2018.10.141.

[12] A. Binek, M. L. Petrus, N. Huber, H. Bristow, Y. Hu, T. Bein, and P. Docampo, "Recycling Perovskite Solar Cells To Avoid Lead Waste", *ACS applied materials & interfaces*, vol. 8, no. 20, pp. 12 881–12 886, 2016. DOI: 10.1021/acsami.6b03767.

[13] U. Farooq, M. Ishaq, U. A. Shah, S. Chen, Z.-H. Zheng, M. Azam, Z.-H. Su, R. Tang, P. Fan, Y. Bai, and G.-X. Liang, "Bandgap engineering of lead-free ternary halide perovskites for photovoltaics and beyond: Recent progress and future prospects", *Nano Energy*, vol. 92, p. 106 710, 2022, ISSN: 22112855. DOI: 10.1016/j.nanoen.2021.106710.

[14] National Renewable Energy Laboratory, *Best Research-Cell Efficiency Chart*, Golden, CO, 2022. [Online]. Available: https://www.nrel.gov/pv/cell-efficiency.html.

[15] T. Bellakhdar, Z. Nabi, B. Bouabdallah, B. Benichou, and H. Saci, "Ab initio study of structural, electronic, mechanical and optical properties of the tetragonal Cs2AgBiBr6 halide double perovskite", *Applied Physics A*, vol. 128, no. 2, 2022. DOI: 10.1007/s00339-022-05276-8.

[16] M. Keshavarz, E. Debroye, M. Ottesen, C. Martin, H. Zhang, E. Fron, R. Küchler, J. A. Steele, M. Bremholm, J. van de Vondel, H. I. Wang, M. Bonn, M. B. J. Roeffaers, S. Wiedmann, and J. Hofkens, "Tuning the Structural and Opto-

electronic Properties of Cs2AgBiBr6 Double-Perovskite Single Crystals through Alkali-Metal Substitution", *Advanced Materials*, vol. 32, no. 40, e2001878, 2020. DOI: 10.1002/adma.202001878.

[17] A. H. Slavney, T. Hu, A. M. Lindenberg, and H. I. Karunadasa, "A Bismuth-Halide Double Perovskite with Long Carrier Recombination Lifetime for Photovoltaic Applications", *Journal of the American Chemical Society*, vol. 138, no. 7, pp. 2138–2141, 2016. DOI: 10.1021/jacs.5b13294.

[18] L. Schade, A. D. Wright, R. D. Johnson, M. Dollmann, B. Wenger, P. K. Nayak, D. Prabhakaran, L. M. Herz, R. Nicholas, H. J. Snaith, and P. G. Radaelli, "Structural and Optical Properties of Cs2AgBiBr6 Double Perovskite", *ACS energy letters*, vol. 4, no. 1, pp. 299–305, 2019, ISSN: 2380-8195. DOI: 10.1021/acsenergylett.8b02090.

[19] A. Prokofiev and S. Pasche, "Crystal Growth and Stoichiometry of Strongly Correlated Intermetallic Cerium Compounds", in *Crystal Growth and Stoichiometry of Strongly Correlated Intermetallic Cerium Compounds*, S. Paschen and A. Prokofiev, Eds., IntechOpen, 2012, ISBN: 978-953-307-610-2. DOI: 10.5772/29675.

[20] A. F. May, J. Yan, and M. A. McGuire, "A practical guide for crystal growth of van der Waals layered materials", *Journal of Applied Physics*, vol. 128, no. 5, p. 051 101, 2020, ISSN: 0021-8979. DOI: 10.1063/5.0015971.

[21] S. Dobberschütz, M. R. Nielsen, K. K. Sand, R. Civioc, N. Bovet, S. L. S. Stipp, and M. P. Andersson, "The mechanisms of crystal growth inhibition by organic and inorganic inhibitors", *Nature communications*, vol. 9, no. 1, p. 1578, 2018. DOI: 10.1038/s41467-018-04022-0.

[22] J. Bohm, "The history of crystal growth", *Acta Physica Hungarica*, vol. 57, no. 3-4, pp. 161–178, 1985, ISSN: 0231-4428. DOI: 10.1007/BF03158886.

[23] I. I. Shafranovskii, "14.10. Kepler's crystallographic ideas and his tract "The six-cornered snowflake"", *Vistas in Astronomy*, vol. 18, pp. 861–876, 1975, ISSN: 00836656. DOI: 10.1016/0083-6656(75)90181-6.

[24] R. Uecker, "The historical development of the Czochralski method", *Journal of Crystal Growth*, vol. 401, pp. 7–24, 2014, ISSN: 00220248. DOI: 10.1016/j.jcrysgro.2013.11.095.

[25] P. W. Bridgman, "Certain Physical Properties of Single Crystals of Tungsten, Antimony, Bismuth, Tellurium, Cadmium, Zinc, and Tin", *Proceedings of the American Academy of Arts and Sciences*, vol. 60, no. 6, p. 305, 1925, ISSN: 01999818. DOI: 10.2307/25130058.

[26] F. Giustino and H. J. Snaith, "Toward Lead-Free Perovskite Solar Cells", *ACS energy letters*, vol. 1, no. 6, pp. 1233–1240, 2016, ISSN: 2380-8195. DOI: 10.1021/acsenergylett.6b00499.

[27] M. Lyu, J.-H. Yun, P. Chen, M. Hao, and L. Wang, "Addressing Toxicity of Lead: Progress and Applications of Low-Toxic Metal Halide Perovskites and Their Derivatives", *Advanced Energy Materials*, vol. 7, no. 15, p. 1 602 512, 2017, ISSN: 1614-6832. DOI: 10.1002/aenm.201602512.

[28] M. I. Saidaminov, A. L. Abdelhady, G. Maculan, and O. M. Bakr, "Retrograde solubility of formamidinium and methylammonium lead halide perovskites enabling rapid single crystal growth", *Chemical communications (Cambridge, England)*, vol. 51, no. 100, pp. 17 658–17 661, 2015. DOI: 10.1039/c5cc06916e.

[29] T. Baikie, N. S. Barrow, Y. Fang, P. J. Keenan, P. R. Slater, R. O. Piltz, M. Gutmann, S. G. Mhaisalkar, and T. J. White, "A combined single crystal neutron/X-ray diffraction and solid-state nuclear magnetic resonance study of the hybrid perovskites CH3NH3PbX3 (X = I, Br and Cl)", *Journal of Materials Chemistry A*, vol. 3, no. 17, pp. 9298–9307, 2015. DOI: 10.1039/C5TA01125F.

[30] W. S. Yang, J. H. Noh, N. J. Jeon, Y. C. Kim, S. Ryu, J. Seo, and S. I. Seok, "SOLAR CELLS. High-performance photovoltaic perovskite layers fabricated through intramolecular exchange", *Science (New York, N.Y.)*, vol. 348, no. 6240, pp. 1234–1237, 2015. DOI: 10.1126/science.aaa9272.

[31] V. D'Innocenzo, G. Grancini, M. J. P. Alcocer, A. R. S. Kandada, S. D. Stranks, M. M. Lee, G. Lanzani, H. J. Snaith, and A. Petrozza, "Excitons versus free charges in organo-lead tri-halide perovskites", *Nature communications*, vol. 5, p. 3586, 2014. DOI: 10.1038/ncomms4586.

[32] D. Shi, V. Adinolfi, R. Comin, M. Yuan, E. Alarousu, A. Buin, Y. Chen, S. Hoogland, A. Rothenberger, K. Katsiev, Y. Losovyj, X. Zhang, P. A. Dowben, O. F. Mohammed, E. H. Sargent, and O. M. Bakr, "Solar cells. Low trap-state density and long carrier diffusion in organolead trihalide perovskite single crystals", *Science (New York, N.Y.)*, vol. 347, no. 6221, pp. 519–522, 2015. DOI: 10.1126/science.aaa2725.

[33] Y. Deng, E. Peng, Y. Shao, Z. Xiao, Q. Dong, and J. Huang, "Scalable fabrication of efficient organolead trihalide perovskite solar cells with doctor-bladed active layers", *Energy & Environmental Science*, vol. 8, no. 5, pp. 1544–1550, 2015. DOI: 10.1039/C4EE03907F.

[34] G. Xing, N. Mathews, S. Sun, S. S. Lim, Y. M. Lam, M. Grätzel, S. Mhaisalkar, and T. C. Sum, "Long-range balanced electron- and hole-transport lengths in organic-inorganic CH3NH3PbI3", *Science (New York, N.Y.)*, vol. 342, no. 6156, pp. 344–347, 2013. DOI: 10.1126/science.1243167.

[35] M. A. Green, A. Ho-Baillie, and H. J. Snaith, "The emergence of perovskite solar cells", *Nature Photonics*, vol. 8, no. 7, pp. 506–514, 2014, ISSN: 1749-4885. DOI: 10.1038/NPHOTON.2014.134.

[36] C. Wehrenfennig, G. E. Eperon, M. B. Johnston, H. J. Snaith, and L. M. Herz, "High charge carrier mobilities and lifetimes in organolead trihalide perovskites", *Advanced materials (Deerfield Beach, Fla.)*, vol. 26, no. 10, pp. 1584–1589, 2014. DOI: 10.1002/adma.201305172.

[37] Y. Hu, E. M. Hutter, P. Rieder, I. Grill, J. Hanisch, M. F. Aygüler, A. G. Hufnagel, M. Handloser, T. Bein, A. Hartschuh, K. Tvingstedt, V. Dyakonov, A. Baumann, T. J. Savenije, M. L. Petrus, and P. Docampo, "Understanding the Role of Cesium and Rubidium Additives in Perovskite Solar Cells: Trap States, Charge Transport, and Recombination", *Advanced Energy Materials*, vol. 8, no. 16, p. 1 703 057, 2018, ISSN: 1614-6832. DOI: 10.1002/aenm.201703057.

[38] H. Hempel, T. J. Savenjie, M. Stolterfoht, J. Neu, M. Failla, V. C. Paingad, P. Kužel, E. J. Heilweil, J. A. Spies, M. Schleuning, J. Zhao, D. Friedrich, K. Schwarzburg, L. D. Siebbeles, P. Dörflinger, V. Dyakonov, R. Katoh, M. J. Hong, J. G. Labram, M. Monti, E. Butler-Caddle, J. Lloyd-Hughes, M. M. Taheri, J. B. Baxter, T. J. Magnanelli, S. Luo, J. M. Cardon, S. Ardo, and T. Unold, "Predicting Solar Cell Performance from Terahertz and Microwave Spectroscopy", *Advanced Energy Materials*, vol. 12, no. 13, p. 2 102 776, 2022, ISSN: 1614-6832. DOI: 10.1002/aenm.202102776.

[39] D. S. Bhachu, D. O. Scanlon, E. J. Saban, H. Bronstein, I. P. Parkin, C. J. Carmalt, and R. G. Palgrave, "Scalable route to CH3NH3PbI3 perovskite thin films by aerosol assisted chemical vapour deposition", *Journal of Materials Chemistry A*, vol. 3, no. 17, pp. 9071–9073, 2015. DOI: 10.1039/C4TA05522E.

[40] A. T. Barrows, A. J. Pearson, C. K. Kwak, A. D. F. Dunbar, A. R. Buckley, and D. G. Lidzey, "Efficient planar heterojunction mixed-halide perovskite solar cells deposited via spray-deposition", *Energy & Environmental Science*, vol. 7, no. 9, pp. 2944–2950, 2014. DOI: 10.1039/C4EE01546K.

[41] H. Min, D. Y. Lee, J. Kim, G. Kim, K. S. Lee, J. Kim, M. J. Paik, Y. K. Kim, K. S. Kim, M. G. Kim, T. J. Shin, and S. Il Seok, "Perovskite solar cells with atomically coherent interlayers on SnO2 electrodes", *Nature*, vol. 598, no. 7881, pp. 444–450, 2021. DOI: 10.1038/s41586-021-03964-8. [Online]. Available: https://www.nature.com/articles/s41586-021-03964-8.

[42] L. Liang and P. Gao, "Lead-Free Hybrid Perovskite Absorbers for Viable Application: Can We Eat the Cake and Have It too?", *Advanced science (Weinheim, Baden-Wurttemberg, Germany)*, vol. 5, no. 2, p. 1 700 331, 2018, ISSN: 2198-3844. DOI: 10.1002/advs.201700331.

[43] E. Meyer, D. Mutukwa, N. Zingwe, and R. Taziwa, "Lead-Free Halide Double Perovskites: A Review of the Structural, Optical, and Stability Properties as Well as Their Viability to Replace Lead Halide Perovskites", *Metals*, vol. 8, no. 9, p. 667, 2018. DOI: 10.3390/met8090667.

[44] L. Serrano-Lujan, N. Espinosa, T. T. Larsen-Olsen, J. Abad, A. Urbina, and F. C. Krebs, "Tin- and Lead-Based Perovskite Solar Cells under Scrutiny: An Environmental Perspective", *Advanced Energy Materials*, vol. 5, no. 20, p. 1 501 119, 2015, ISSN: 1614-6832. DOI: 10.1002/aenm.201501119.

[45] B. V. Lotsch, "New light on an old story: perovskites go solar", *Angewandte Chemie (International ed. in English)*, vol. 53, no. 3, pp. 635–637, 2014. DOI: 10.1002/anie.201309368.

[46] L. Chu, W. Ahmad, W. Liu, J. Yang, R. Zhang, Y. Sun, J. Yang, and X. Li, "Lead-Free Halide Double Perovskite Materials: A New Superstar Toward Green and Stable Optoelectronic Applications", *Nano-Micro Letters*, vol. 11, no. 1, p. 6050, 2019. DOI: 10.1007/s40820-019-0244-6.

[47] G. Flora, D. Gupta, and A. Tiwari, "Toxicity of lead: A review with recent updates", *Interdisciplinary toxicology*, vol. 5, no. 2, pp. 47–58, 2012. DOI: 10.2478/v10102-012-0009-2.

[48] J. Li, H.-L. Cao, W.-B. Jiao, Q. Wang, M. Wei, I. Cantone, J. Lü, and A. Abate, "Biological impact of lead from halide perovskites reveals the risk of introducing a safe threshold", *Nature communications*, vol. 11, no. 1, p. 310, 2020. DOI: 10.1038/s41467-019-13910-y.

[49] Europäisches Parlament, *Richtlinie 2001/65/Eu Des Europäischen Parlaments und des Rates vom 8. Juni 2011 zur Beschränkung der Verwendung bestimmter gefährlicher Stoffe in Elektro- und Elektronikgeräten*, 2011.

[50] X. Wang, T. Zhang, Y. Lou, and Y. Zhao, "All-inorganic lead-free perovskites for optoelectronic applications", *Materials Chemistry Frontiers*, vol. 3, no. 3, pp. 365–375, 2019. DOI: 10.1039/C8QM00611C.

[51] R. E. Brandt, V. Stevanović, D. S. Ginley, and T. Buonassisi, *Identifying defect-tolerant semiconductors with high minority-carrier lifetimes: beyond hybrid lead halide perovskites*, 2015. DOI: 10.1557/mrc.2015.26. [Online]. Available: https://arxiv.org/pdf/1504.02144.

[52] W. Shockley and H. J. Queisser, "Detailed Balance Limit of Efficiency of p–n Junction Solar Cells", *Journal of Applied Physics*, vol. 32, no. 3, pp. 510–519, 1961, ISSN: 0021-8979. DOI: 10.1063/1.1736034.

[53] A. Zakutayev, C. M. Caskey, A. N. Fioretti, D. S. Ginley, J. Vidal, V. Stevanovic, E. Tea, and S. Lany, "Defect Tolerant Semiconductors for Solar Energy Conversion", *The journal of physical chemistry letters*, vol. 5, no. 7, pp. 1117–1125, 2014. DOI: 10.1021/jz5001787.

[54] V. M. Goldschmidt, "Die Gesetze der Krystallochemie", *Die Naturwissenschaften*, vol. 14, no. 21, pp. 477–485, 1926, ISSN: 0028-1042. DOI: 10.1007/BF01507527.

[55] G. Kieslich, S. Sun, and A. K. Cheetham, "Solid-state principles applied to organic–inorganic perovskites: new tricks for an old dog", *Chem. Sci.*, vol. 5, no. 12, pp. 4712–4715, 2014, ISSN: 2041-6520. DOI: 10.1039/C4SC02211D.

[56] T. J. Jacobsson, M. Pazoki, A. Hagfeldt, and T. Edvinsson, "Goldschmidt's Rules and Strontium Replacement in Lead Halogen Perovskite Solar Cells: Theory and Preliminary Experiments on CH3NH3SrI3", *The Journal of Physical Chemistry C*, vol. 119, no. 46, pp. 25 673–25 683, 2015. DOI: 10.1021/acs.jpcc.5b06436.

[57] B.-B. Yu, Z. Chen, Y. Zhu, Y. Wang, B. Han, G. Chen, X. Zhang, Z. Du, and Z. He, "Heterogeneous 2D/3D Tin-Halides Perovskite Solar Cells with Certified Conversion Efficiency Breaking 14", *Advanced materials (Deerfield Beach, Fla.)*, vol. 33, no. 36, e2102055, 2021. DOI: 10.1002/adma.202102055.

[58] H. Dong, C. Ran, W. Gao, N. Sun, X. Liu, Y. Xia, Y. Chen, and W. Huang, "Crystallization Dynamics of Sn–Based Perovskite Thin Films: Toward Efficient and Stable Photovoltaic Devices", *Advanced Energy Materials*, vol. 12, no. 1, p. 2 102 213, 2022, ISSN: 1614-6832. DOI: 10.1002/aenm.202102213.

[59] A. W. Azhari, F. S. X. Then, D. S. C. Halin, S. Sepeai, and N. A. Ludin, "Tin and germanium substitution in lead free perovskite solar cell: current status and future trends", *IOP Conference Series: Materials Science and Engineering*, vol. 957, no. 1, p. 012 057, 2020, ISSN: 1757-8981. DOI: 10.1088/1757-899X/957/1/012057.

[60] A. K. Baranwal, H. Masutani, H. Sugita, H. Kanda, S. Kanaya, N. Shibayama, Y. Sanehira, M. Ikegami, Y. Numata, K. Yamada, T. Miyasaka, T. Umeyama, H. Imahori, and S. Ito, "Lead-free perovskite solar cells using Sb and Bi-based A3B2X9 and A3BX6 crystals with normal and inverse cell structures", *Nano convergence*, vol. 4, no. 1, p. 26, 2017, ISSN: 2196-5404. DOI: 10.1186/s40580-017-0120-3.

[61] A. Jodlowski, D. Rodríguez-Padrón, R. Luque, and G. de Miguel, "Alternative Perovskites for Photovoltaics", *Advanced Energy Materials*, vol. 8, no. 21, p. 1 703 120, 2018, ISSN: 1614-6832. DOI: 10.1002/aenm.201703120.

[62] A. Singh and S. Satapathi, "Reversible Thermochromism in All–Inorganic Lead–Free Cs3Sb2I9 Perovskite Single Crystals", *Advanced Optical Materials*, vol. 9, no. 22, p. 2 101 062, 2021, ISSN: 2195-1071. DOI: 10.1002/adom.202101062.

[63] W. Ke and M. G. Kanatzidis, "Prospects for low-toxicity lead-free perovskite solar cells", *Nature communications*, vol. 10, no. 1, p. 965, 2019. DOI: 10.1038/s41467-019-08918-3. [Online]. Available: https://www.nature.com/articles/s41467-019-08918-3.

[64] J. Luo, S. Li, H. Wu, Y. Zhou, Y. Li, J. Liu, J. Li, K. Li, F. Yi, G. Niu, and J. Tang, "Cs2AgInCl6 Double Perovskite Single Crystals: Parity Forbidden Transitions and Their Application For Sensitive and Fast UV Photodetectors", *ACS Photonics*, vol. 5, no. 2, pp. 398–405, 2018, ISSN: 2330-4022. DOI: 10.1021/acsphotonics.7b00837.

[65] A. D. Wright, L. R. V. Buizza, K. J. Savill, G. Longo, H. J. Snaith, M. B. Johnston, and L. M. Herz, "Ultrafast Excited-State Localization in Cs2AgBiBr6 Double Perovskite", *The journal of physical chemistry letters*, vol. 12, no. 13, pp. 3352–3360, 2021. DOI: 10.1021/acs.jpclett.1c00653.

[66] S. Khalfin and Y. Bekenstein, "Advances in lead-free double perovskite nanocrystals, engineering band-gaps and enhancing stability through composition tunability", *Nanoscale*, vol. 11, no. 18, pp. 8665–8679, 2019. DOI: 10.1039/C9NR01031A..

[67] C. J. Bartel, C. Sutton, B. R. Goldsmith, R. Ouyang, C. B. Musgrave, L. M. Ghiringhelli, and M. Scheffler, "New tolerance factor to predict the stability of perovskite oxides and halides", *Science advances*, vol. 5, no. 2, eaav0693, 2019. DOI: 10.1126/sciadv.aav0693.

[68] E. T. McClure, M. R. Ball, W. Windl, and P. M. Woodward, "Cs2AgBiX6 (X = Br, Cl): New Visible Light Absorbing, Lead-Free Halide Perovskite Semiconductors", *Chemistry of Materials*, vol. 28, no. 5, pp. 1348–1354, 2016. DOI: 10.1021/acs.chemmater.5b04231.

[69] G. Longo, S. Mahesh, L. R. V. Buizza, A. D. Wright, A. J. Ramadan, M. Abdi-Jalebi, P. K. Nayak, L. M. Herz, and H. J. Snaith, "Understanding the Performance-Limiting Factors of Cs2AgBiBr6 Double-Perovskite Solar Cells", *ACS energy letters*, pp. 2200–2207, 2020, ISSN: 2380-8195. DOI: 10.1021/acsenergylett.0c01020.

[70] R. Kentsch, M. Scholz, J. Horn, D. Schlettwein, K. Oum, and T. Lenzer, "Exciton Dynamics and Electron–Phonon Coupling Affect the Photovoltaic Performance of the Cs2AgBiBr6 Double Perovskite", *The Journal of Physical Chemistry C*, vol. 122, no. 45, pp. 25 940–25 947, 2018. DOI: 10.1021/acs.jpcc.8b09911.

[71] B. Wang, N. Li, L. Yang, C. Dall'Agnese, A. K. Jena, T. Miyasaka, and X.-F. Wang, "Organic Dye/Cs2AgBiBr6 Double Perovskite Heterojunction Solar Cells", *Journal of the American Chemical Society*, vol. 143, no. 36, pp. 14 877–14 883, 2021. DOI: 10.1021/jacs.1c07200.

[72] G. Dhanaraj, K. Byrappa, V. Prasad, and M. Dudley, *Springer Handbook of Crystal Growth*. Berlin, Heidelberg: Springer Berlin Heidelberg, 2010. DOI: 10.1007/978-3-540-74761-1.

[73] P. Fassl, V. Lami, A. Bausch, Z. Wang, M. T. Klug, H. J. Snaith, and Y. Vaynzof, "Fractional deviations in precursor stoichiometry dictate the properties, performance and stability of perovskite photovoltaic devices", *Energy & Environmental Science*, vol. 11, no. 12, pp. 3380–3391, 2018. DOI: 10.1039/c8ee01136b.

[74] Y. Vaynzof, "The Future of Perovskite Photovoltaics—Thermal Evaporation or Solution Processing?", *Advanced Energy Materials*, vol. 10, no. 48, p. 2 003 073, 2020, ISSN: 1614-6832. DOI: 10.1002/aenm.202003073.

[75] L. M. Falk, K. P. Goetz, V. Lami, Q. An, P. Fassl, J. Herkel, F. Thome, A. D. Taylor, F. Paulus, and Y. Vaynzof, "Effect of Precursor Stoichiometry on the Performance and Stability of MAPbBr3 Photovoltaic Devices", *Energy technology (Weinheim,*

Germany), vol. 8, no. 4, p. 1 900 737, 2020, ISSN: 2194-4288. DOI: 10.1002/ente.201900737.

[76] J. Bohm, Ed., *Kristallzüchtung*, 1. Aufl. Berlin: Dt. Verl. d. Wiss, 1989, ISBN: 3326000928.

[77] W. Kossel, "Zur Theorie des Kristallwachstums", *Nachrichten von der Gesellschaft der Wissenschaften zu Göttingen, Mathematisch-Physikalische Klasse 1927*, pp. 135–143, 1927. [Online]. Available: http://eudml.org/doc/59220>.

[78] S. Hammer, "Influence of Crystal Structure on Excited States in Crystalline Organic Semiconductors", PhD, Julius-Maximilians-Universität Würzburg, Würzburg, 2021-08-25. (visited on 10/05/2022).

[79] W. Kleber, D. Klimm, J. Bohm, and H.-J. Bautsch, *Einführung in die Kristallographie*, 19., verb. Aufl. München: Oldenbourg, 2012, ISBN: 978-3-486-59075-3. DOI: 10.1515/9783486598858.

[80] J. H. Höcker, "High-quality Organolead Trihalide Perovskite Crystals: Growth, Characterisation, and Photovoltaic Applications", Ph.D. dissertation, Universität Würzburg, 2022. DOI: 10.25972/OPUS-25859.

[81] M. Armer, J. Höcker, C. Büchner, S. Häfele, P. Dörflinger, M. T. Sirtl, K. Tvingstedt, T. Bein, and V. Dyakonov, "Influence of crystallisation on the structural and optical properties of lead-free Cs2AgBiBr6 perovskite crystals", *CrystEngComm*, vol. 23, no. 39, pp. 6848–6854, 2021. DOI: 10.1039/D1CE00844G.

[82] P. Crafts, "The Role of Solubility Modeling and Crystallization in the Design of Active Pharmaceutical Ingredients", in *Chemical Product Design: Toward a Perspective Through Case Studies*, ser. Computer Aided Chemical Engineering, vol. 23, Elsevier, 2007, pp. 23–85, ISBN: 9780444522177. DOI: 10.1016/S1570-7946(07)80005-8.

[83] R. Babu, L. Giribabu, and S. P. Singh, "Recent Advances in Halide-Based Perovskite Crystals and Their Optoelectronic Applications", *Crystal Growth & Design*, vol. 18, no. 4, pp. 2645–2664, 2018, ISSN: 1528-7483. DOI: 10.1021/acs.cgd.7b01767.

[84] N. K. Tailor, S. Kar, P. Mishra, A. These, C. Kupfer, H. Hu, M. Awais, M. Saidaminov, M. I. Dar, C. Brabec, and S. Satapathi, "Advances in Lead-Free Perovskite Single Crystals: Fundamentals and Applications", *ACS Materials Letters*, pp. 1025–1080, 2021. DOI: 10.1021/acsmaterialslett.1c00242.

[85] M. I. Saidaminov, A. L. Abdelhady, B. Murali, E. Alarousu, V. M. Burlakov, W. Peng, I. Dursun, L. Wang, Y. He, G. Maculan, A. Goriely, T. Wu, O. F. Mohammed, and O. M. Bakr, "High-quality bulk hybrid perovskite single crystals within minutes by inverse temperature crystallization", *Nature communications*, vol. 6, p. 7586, 2015. DOI: 10.1038/ncomms8586.

[86] J. Höcker, F. Brust, M. Armer, and V. Dyakonov, "A temperature-reduced method for the rapid growth of hybrid perovskite single crystals with primary alcohols", *CrystEngComm*, vol. 23, no. 11, pp. 2202–2207, 2021. DOI: 10.1039/D0CE01759K.

[87] Y. Dang, D. Ju, L. Wang, and X. Tao, "Recent progress in the synthesis of hybrid halide perovskite single crystals", *CrystEngComm*, vol. 18, no. 24, pp. 4476–4484, 2016. DOI: 10.1039/C6CE00655H.

[88] L. Yin, H. Wu, W. Pan, B. Yang, P. Li, J. Luo, G. Niu, and J. Tang, "Controlled Cooling for Synthesis of Cs2AgBiBr6 Single Crystals and Its Application for X–Ray Detection", *Advanced Optical Materials*, vol. 7, no. 19, p. 1 900 491, 2019, ISSN: 2195-1071. DOI: 10.1002/adom.201900491.

[89] Y. Xian, H. Yin, Y. Bao, Y. Xiao, S. Yuan, N. U. Rahman, Y. Yuan, Y. Zhang, X. Meng, S. Jin, W. Li, and J. Fan, "Engineered Electronic Structure and Carrier Dynamics in Emerging Cs2AgxNa1-xFeCl6 Perovskite Single Crystals", *The journal of physical chemistry letters*, vol. 11, no. 22, pp. 9535–9542, 2020. DOI: 10.1021/acs.jpclett.0c02963.

[90] Z. Zhang, C.-C. Chung, Z. Huang, E. Vetter, D. Seyitliyev, D. Sun, K. Gundogdu, F. N. Castellano, E. O. Danilov, and G. Yang, "Towards radiation detection using Cs2AgBiBr6 double perovskite single crystals", *Materials Letters*, vol. 269, p. 127 667, 2020, ISSN: 0167577X. DOI: 10.1016/j.matlet.2020.127667.

[91] R. L. Z. Hoye, L. Eyre, F. Wei, F. Brivio, A. Sadhanala, S. Sun, W. Li, K. H. L. Zhang, J. L. MacManus-Driscoll, P. D. Bristowe, R. H. Friend, A. K. Cheetham, and F. Deschler, "Fundamental Carrier Lifetime Exceeding 1 µs in Cs2AgBiBr6 Double Perovskite", *Advanced Materials Interfaces*, vol. 5, no. 15, p. 1 800 464, 2018. DOI: 10.1002/admi.201800464.

[92] H. Wang and D. H. Kim, "Perovskite-based photodetectors: materials and devices", *Chemical Society reviews*, vol. 46, no. 17, pp. 5204–5236, 2017. DOI: 10.1039/c6cs00896h.

[93] Z. Tan, Y. Wu, H. Hong, J. Yin, J. Zhang, L. Lin, M. Wang, X. Sun, L. Sun, Y. Huang, K. Liu, Z. Liu, and H. Peng, "Two-Dimensional (C4H9NH3)2PbBr4 Perovskite Crystals for High-Performance Photodetector", *Journal of the American Chemical Society*, vol. 138, no. 51, pp. 16 612–16 615, 2016. DOI: 10.1021/jacs.6b11683.

[94] J. Miao and F. Zhang, "Recent progress on highly sensitive perovskite photodetectors", *Journal of Materials Chemistry C*, vol. 7, no. 7, pp. 1741–1791, 2019. DOI: 10.1039/C8TC06089D.

[95] Y. Lei, S. Wang, J. Xing, H. Xu, J. Han, and W. Liu, "High-Performance UV-Vis Photodetectors Based on a Lead-Free Hybrid Perovskite Crystal (MV)SbI3Cl2", *Inorganic chemistry*, vol. 59, no. 7, pp. 4349–4356, 2020. DOI: 10.1021/acs.inorgchem.9b03277.

[96] M. I. Saidaminov, V. Adinolfi, R. Comin, A. L. Abdelhady, W. Peng, I. Dursun, M. Yuan, S. Hoogland, E. H. Sargent, and O. M. Bakr, "Planar-integrated single-crystalline perovskite photodetectors", *Nature communications*, vol. 6, p. 8724, 2015. DOI: 10.1038/ncomms9724.

[97] M. S. Shackley, "An Introduction to X-Ray Fluorescence (XRF) Analysis in Archaeology", in *X-Ray Fluorescence Spectrometry (XRF) in Geoarchaeology*, M. S. Shackley, Ed., New York, NY: Springer New York, 2011, pp. 7–44, ISBN: 978-1-4419-6885-2. DOI: 10.1007/978-1-4419-6886-9_2.

[98] D. Shindo and T. Oikawa, "Energy Dispersive X-ray Spectroscopy", in *Analytical electron microscopy for materials science*, D. Shindō and T. Oikawa, Eds., Tokyo and London: Springer, 2002, pp. 81–102, ISBN: 978-4-431-70336-5. DOI: 10.1007/978-4-431-66988-3_4.

[99] V. Podzorov, E. Menard, A. Borissov, V. Kiryukhin, J. A. Rogers, and M. E. Gershenson, "Intrinsic charge transport on the surface of organic semiconductors", *Physical review letters*, vol. 93, no. 8, p. 086 602, 2004, ISSN: 0031-9007. DOI: 10.1103/PhysRevLett.93.086602.

[100] B. K. Vainsthein, *Fundamentals of crystals: Symmetry, and methods of structural crystallography*. Berlin, Heidelberg, Germany: Springer, 1994, ISBN: 9783662029756. [Online]. Available: https://ebookcentral.proquest.com/lib/kxp/detail.action?docID=3097143.

[101] H. Haken, *Atom- und Quantenphysik: Eine Einführung in Die Experimentellen und Theoretischen Grundlagen*, 3rd ed. Berlin, Heidelberg: Springer Berlin

/ Heidelberg, 1987, ISBN: 9783642970252. [Online]. Available: https://ebookcentral.proquest.com/lib/kxp/detail.action?docID=6593434.

[102] L. Spieß, R. Schwarzer, H. Behnken, and G. Teichert, *Moderne Röntgenbeugung: Röntgendiffraktometrie für Materialwissenschaftler, Physiker und Chemiker* (Springer eBook Collection Life Science and Basic Disciplines). Wiesbaden: Vieweg+Teubner Verlag, 2005, ISBN: 9783663108313. DOI: 10.1007/978-3-663-10831-3.

[103] M. Fox, *Optical properties of solids* (Oxford master series in condensed matter physics), 2nd ed. Oxford: Oxford University Press, 2010, vol. v. 3, ISBN: 9780199573363.

[104] T. Kirchartz, J. A. Márquez, M. Stolterfoht, and T. Unold, "Photoluminescence–Based Characterization of Halide Perovskites for Photovoltaics", *Advanced Energy Materials*, p. 1 904 134, 2020, ISSN: 1614-6832. DOI: 10.1002/aenm.201904134.

[105] P. Wurfel, "The chemical potential of radiation", *Journal of Physics C: Solid State Physics*, vol. 15, no. 18, pp. 3967–3985, 1982, ISSN: 0022-3719. DOI: 10.1088/0022-3719/15/18/012.

[106] P. Würfel, S. Finkbeiner, and E. Daub, "Generalized Planck's radiation law for luminescence via indirect transitions", *Applied Physics A*, vol. 60, no. 1, pp. 67–70, 1995, ISSN: 0947-8396. DOI: 10.1007/BF01577615.

[107] K. Schick, E. Daub, S. Finkbeiner, and P. Wrfel, "Verification of a generalized Planck law for luminescence radiation from silicon solar cells", *Applied Physics A*, vol. 54, no. 2, pp. 109–114, 1992, ISSN: 0947-8396. DOI: 10.1007/BF00323895.

[108] W. van Roosbroeck and W. Shockley, "Photon-Radiative Recombination of Electrons and Holes in Germanium", *Physical Review*, vol. 94, no. 6, pp. 1558–1560, 1954. DOI: 10.1103/PhysRev.94.1558.

[109] U. Rau, "Reciprocity relation between photovoltaic quantum efficiency and electroluminescent emission of solar cells", *Physical Review B*, vol. 76, no. 8, 2007. DOI: 10.1103/PhysRevB.76.085303.

[110] J. Mooney and P. Kambhampati, "Get the Basics Right: Jacobian Conversion of Wavelength and Energy Scales for Quantitative Analysis of Emission Spectra", *The journal of physical chemistry letters*, vol. 4, no. 19, pp. 3316–3318, 2013. DOI: 10.1021/jz401508t.

[111] V. Sarritzu, N. Sestu, D. Marongiu, X. Chang, S. Masi, A. Rizzo, S. Colella, F. Quochi, M. Saba, A. Mura, and G. Bongiovanni, "Optical determination of Shockley-Read-Hall and interface recombination currents in hybrid perovskites", *Scientific reports*, vol. 7, p. 44 629, 2017. DOI: 10.1038/srep44629.

[112] Schmidt, Lischka, and Zulehner, "Excitation-power dependence of the near-band-edge photoluminescence of semiconductors", *Physical review. B, Condensed matter*, vol. 45, no. 16, pp. 8989–8994, 1992, ISSN: 0163-1829. DOI: 10.1103/physrevb.45.8989.

[113] D. Abou-Ras, T. Kirchartz, and U. Rau, *Advanced characterization techniques for thin film solar cells*. Weinheim: Wiley-VCH, 2011, ISBN: 9783527410033.

[114] F. Igbari, R. Wang, Z.-K. Wang, X.-J. Ma, Q. Wang, K.-L. Wang, Y. Zhang, L.-S. Liao, and Y. Yang, "Composition Stoichiometry of Cs2AgBiBr6 Films for Highly Efficient Lead-Free Perovskite Solar Cells", *Nano letters*, vol. 19, no. 3, pp. 2066–2073, 2019. DOI: 10.1021/acs.nanolett.9b00238.

[115] Y. Yin, W. Tian, J. Leng, J. Bian, and S. Jin, "Carrier Transport Limited by Trap State in Cs2AgBiBr6 Double Perovskites", *The journal of physical chemistry letters*, vol. 11, no. 17, pp. 6956–6963, 2020. DOI: 10.1021/acs.jpclett.0c01817.

[116] J. Li, F. Yan, P. Yang, Y. Duan, J. Duan, and Q. Tang, "Suppressing Interfacial Shunt Loss via Functional Polymer for Performance Improvement of Lead–Free Cs2AgBiBr6 Double Perovskite Solar Cells", *Solar RRL*, vol. 6, no. 4, p. 2 100 791, 2022. DOI: 10.1002/solr.202100791.

[117] J. A. Steele, W. Pan, C. Martin, M. Keshavarz, E. Debroye, H. Yuan, S. Banerjee, E. Fron, D. Jonckheere, C. W. Kim, W. Baekelant, G. Niu, J. Tang, J. Vanacken, M. van der Auweraer, J. Hofkens, and M. B. J. Roeffaers, "Photophysical Pathways in Highly Sensitive Cs2AgBiBr6 Double-Perovskite Single-Crystal X-Ray Detectors", *Advanced materials (Deerfield Beach, Fla.)*, vol. 30, no. 46, e1804450, 2018. DOI: 10.1002/adma.201804450..

[118] G. Volonakis, M. R. Filip, A. A. Haghighirad, N. Sakai, B. Wenger, H. J. Snaith, and F. Giustino, "Lead-Free Halide Double Perovskites via Heterovalent Substitution of Noble Metals", *The journal of physical chemistry letters*, vol. 7, no. 7, pp. 1254–1259, 2016. DOI: 10.1021/acs.jpclett.6b00376.

[119] E. V. Péan, S. Dimitrov, C. S. de Castro, and M. L. Davies, "Interpreting time-resolved photoluminescence of perovskite materials", *Physical chemistry chemical physics : PCCP*, vol. 22, no. 48, pp. 28 345–28 358, 2020. DOI: 10.1039/d0cp04950f.

[120] F. Staub, H. Hempel, J.-C. Hebig, J. Mock, U. W. Paetzold, U. Rau, T. Unold, and T. Kirchartz, "Beyond Bulk Lifetimes: Insights into Lead Halide Perovskite Films from Time-Resolved Photoluminescence", *Physical Review Applied*, vol. 6, no. 4, 2016. DOI: 10.1103/PhysRevApplied.6.044017.

[121] D. W. deQuilettes, K. Frohna, D. Emin, T. Kirchartz, V. Bulovic, D. S. Ginger, and S. D. Stranks, "Charge-Carrier Recombination in Halide Perovskites", *Chemical reviews*, vol. 119, no. 20, pp. 11 007–11 019, 2019. DOI: 10.1021/acs.chemrev.9b00169.

[122] J. C. de Mello, H. F. Wittmann, and R. H. Friend, "An improved experimental determination of external photoluminescence quantum efficiency", *Advanced Materials*, vol. 9, no. 3, pp. 230–232, 1997. DOI: 10.1002/adma.19970090308.

[123] L. Wang, M. T. Wilson, and N. M. Haegel, "Interpretation of photoluminescence excitation spectroscopy of porous Si layers", *Applied Physics Letters*, vol. 62, no. 10, pp. 1113–1115, 1993. DOI: 10.1063/1.108759.

[124] S. I. Vavilov, "XXIX. The dependence of the intensity of the fluorescence of dyes upon the wave-length of the exciting light", *The London, Edinburgh, and Dublin Philosophical Magazine and Journal of Science*, vol. 43, no. 254, pp. 307–320, 1922, ISSN: 1941-5982. DOI: 10.1080/14786442208565217.

[125] M. Kasha, "Characterization of electronic transitions in complex molecules", *Discussions of the Faraday Society*, vol. 9, p. 14, 1950. DOI: 10.1039/df9500900014.

[126] H. E. Jackson and L. M. Smith, "Optical Properties of Semiconductor Nanowires", in *Semiconductor nanowires. Volume 2, Properties and applications*, ser. Semiconductors and semimetals, 0080-8784, S. A. Dayeh, A. Fontcuberta i Morral, and C. Jagadish, Eds., vol. 94, Amsterdam: Academic Press, 2016, pp. 17–74, ISBN: 9780128040164. DOI: 10.1016/bs.semsem.2015.09.003.

[127] S. Siebentritt, U. Rau, S. Gharabeiki, T. P. Weiss, A. Prot, T. Wang, D. Adeleye, M. Drahem, and A. Singh, "Photoluminescence assessment of materials for solar cell absorbers", *Faraday discussions*, 2022. DOI: 10.1039/d2fd00057a.

[128] C. M. Sutter-Fella, D. W. Miller, Q. P. Ngo, E. T. Roe, F. M. Toma, I. D. Sharp, M. C. Lonergan, and A. Javey, "Band Tailing and Deep Defect States in CH3NH3Pb(I1–xBrx)3 Perovskites As Revealed by Sub-Bandgap Photocurrent", *ACS energy letters*, vol. 2, no. 3, pp. 709–715, 2017, ISSN: 2380-8195. DOI: 10.1021/acsenergylett.6b00727.

[129] G. D. Cody, T. Tiedje, B. Abeles, T. D. Moustakas, B. Brooks, and Y. Goldstein, "DISORDER AND THE OPTICAL ABSORPTION EDGE OF HYDROGENATED AMORPHOUS SILICON", *Le Journal de Physique Colloques*, vol. 42, no. C4, pp. C4–301–C4–304, 1981. DOI: 10.1051/jphyscol:1981463.

[130] M. H. Wolter, R. Carron, E. Avancini, B. Bissig, T. P. Weiss, S. Nishiwaki, T. Feurer, S. Buecheler, P. Jackson, W. Witte, and S. Siebentritt, "How band tail recombination influences the open–circuit voltage of solar cells", *Progress in Photovoltaics: Research and Applications*, vol. 30, no. 7, pp. 702–712, 2022, ISSN: 1062-7995. DOI: 10.1002/pip.3449.

[131] E. Ugur, M. Ledinský, T. G. Allen, J. Holovský, A. Vlk, and S. de Wolf, "Life on the Urbach Edge", *The journal of physical chemistry letters*, vol. 13, no. 33, pp. 7702–7711, 2022. DOI: 10.1021/acs.jpclett.2c01812.

[132] S. Siebentritt, E. Avancini, M. Bär, J. Bombsch, E. Bourgeois, S. Buecheler, R. Carron, C. Castro, S. Duguay, R. Félix, E. Handick, D. Hariskos, V. Havu, P. Jackson, H.-P. Komsa, T. Kunze, M. Malitckaya, R. Menozzi, M. Nesladek, N. Nicoara, M. Puska, M. Raghuwanshi, P. Pareige, S. Sadewasser, G. Sozzi, A. N. Tiwari, S. Ueda, A. Vilalta-Clemente, T. P. Weiss, F. Werner, R. G. Wilks, W. Witte, and M. H. Wolter, "Heavy Alkali Treatment of Cu(In,Ga)Se2 Solar Cells: Surface versus Bulk Effects", *Advanced Energy Materials*, vol. 10, no. 8, p. 1 903 752, 2020, ISSN: 1614-6832. DOI: 10.1002/aenm.201903752.

[133] S. D. Baranovskii, K. Kohary, and P. Thomas, "Urbach tail without bandtail", *Journal of Material Science: Materials in Electronics*, vol. 14, pp. 707–710, 2003.

[134] K. Tvingstedt, J. Benduhn, and K. Vandewal, "Temperature dependence of the spectral line-width of charge-transfer state emission in organic solar cells; static vs. dynamic disorder", *Materials Horizons*, vol. 7, no. 7, pp. 1888–1900, 2020. DOI: 10.1039/D0MH00385A.

[135] L.-Z. Lei, Z.-F. Shi, Y. Li, Z.-Z. Ma, F. Zhang, T.-T. Xu, Y.-T. Tian, Di Wu, X.-J. Li, and G.-T. Du, "High-efficiency and air-stable photodetectors based on lead-free double perovskite Cs2AgBiBr6 thin films", *Journal of Materials Chemistry C*, vol. 6, no. 30, pp. 7982–7988, 2018. DOI: 10.1039/C8TC02305K.

[136] T. Li, J. Wang, Z. Gao, P. Lv, Y. Yang, J. Wu, J. Hong, X. Wang, and Y. Zhou, "Local stress enhanced photocurrent of visible light photo-detection in Cs2AgBiBr6 single crystal", *Applied Physics Letters*, vol. 115, no. 13, p. 131 103, 2019. DOI: 10.1063/1.5116088.

[137] Y. Dang, G. Tong, W. Song, Z. Liu, L. Qiu, L. K. Ono, and Y. Qi, "Interface engineering strategies towards Cs2AgBiBr6 single-crystalline photodetectors with good Ohmic contact behaviours", *Journal of Materials Chemistry C*, vol. 8, no. 1, pp. 276–284, 2020. DOI: 10.1039/C9TC04780H.

[138] J. Luo, X. Wang, S. Li, J. Liu, Y. Guo, G. Niu, L. Yao, Y. Fu, L. Gao, Q. Dong, C. Zhao, M. Leng, F. Ma, W. Liang, L. Wang, S. Jin, J. Han, L. Zhang, J. Etheridge, J. Wang, Y. Yan, E. H. Sargent, and J. Tang, "Efficient and stable emission of warm-white light from lead-free halide double perovskites", *Nature*, vol. 563, no. 7732, pp. 541–545, 2018. DOI: 10.1038/s41586-018-0691-0.

[139] Z. Tan, J. Li, C. Zhang, Z. Li, Q. Hu, Z. Xiao, T. Kamiya, H. Hosono, G. Niu, E. Lifshitz, Y. Cheng, and J. Tang, "Highly Efficient Blue-Emitting Bi-Doped Cs2SnCl6 Perovskite Variant: Photoluminescence Induced by Impurity Doping", *Advanced Functional Materials*, vol. 28, no. 29, p. 1 801 131, 2018. DOI: 10.1002/adfm.201801131.

[140] P. Han, X. Zhang, C. Luo, W. Zhou, S. Yang, J. Zhao, W. Deng, and K. Han, "Manganese-Doped, Lead-Free Double Perovskite Nanocrystals for Bright Orange-Red Emission", *ACS Central Science*, 2020. DOI: 10.1021/acscentsci.0c00056.

[141] C. Wu, Q. Zhang, Y. Liu, W. Luo, X. Guo, Z. Huang, H. Ting, W. Sun, X. Zhong, S. Wei, S. Wang, Z. Chen, and L. Xiao, "The Dawn of Lead-Free Perovskite Solar Cell: Highly Stable Double Perovskite Cs2AgBiBr6 Film", *Advanced science (Weinheim, Baden-Wurttemberg, Germany)*, vol. 5, no. 3, p. 1 700 759, 2018, ISSN: 2198-3844. DOI: 10.1002/advs.201700759.

[142] E. Greul, M. L. Petrus, A. Binek, P. Docampo, and T. Bein, "Highly stable, phase pure Cs2AgBiBr6 double perovskite thin films for optoelectronic applications", *Journal of Materials Chemistry A*, vol. 5, no. 37, pp. 19 972–19 981, 2017. DOI: 10.1039/C7TA06816F.

[143] W. Gao, C. Ran, J. Xi, B. Jiao, W. Zhang, M. Wu, X. Hou, and Z. Wu, "High-Quality Cs2AgBiBr6 Double Perovskite Film for Lead-Free Inverted Planar Heterojunction Solar Cells with 2.2 % Efficiency", *Chemphyschem : a European journal of chemical physics and physical chemistry*, vol. 19, no. 14, pp. 1696–1700, 2018. DOI: 10.1002/cphc.201800346.

[144] M. T. Sirtl, M. Armer, L. K. Reb, R. Hooijer, P. Dörflinger, M. A. Scheel, K. Tvingstedt, P. Rieder, N. Glück, P. Pandit, S. V. Roth, P. Müller-Buschbaum, V. Dyakonov, and T. Bein, "Optoelectronic Properties of Cs2AgBiBr6 Thin Films: The Influ-

ence of Precursor Stoichiometry", *ACS Applied Energy Materials*, vol. 3, no. 12, pp. 11 597–11 609, 2020. DOI: 10.1021/acsaem.0c01308.

[145] X. Yang, W. Wang, R. Ran, W. Zhou, and Z. Shao, "Recent Advances in Cs2AgBiBr6 -Based Halide Double Perovskites as Lead-Free and Inorganic Light Absorbers for Perovskite Solar Cells", *Energy & Fuels*, vol. 34, no. 9, pp. 10 513–10 528, 2020. DOI: 10.1021/acs.energyfuels.0c02236.

[146] W. Pan, H. Wu, J. Luo, Z. Deng, C. Ge, C. Chen, X. Jiang, W.-J. Yin, G. Niu, L. Zhu, L. Yin, Y. Zhou, Q. Xie, X. Ke, M. Sui, and J. Tang, "Cs2AgBiBr6 single-crystal X-ray detectors with a low detection limit", *Nature Photonics*, vol. 11, no. 11, pp. 726–732, 2017. DOI: 10.1038/s41566-017-0012-4.

[147] S. J. Zelewski, J. M. Urban, A. Surrente, D. K. Maude, A. Kuc, L. Schade, R. D. Johnson, M. Dollmann, P. K. Nayak, H. J. Snaith, P. Radaelli, R. Kudrawiec, R. J. Nicholas, P. Plochocka, and M. Baranowski, "Revealing the nature of photoluminescence emission in the metal-halide double perovskite Cs2AgBiBr6", *Journal of Materials Chemistry C*, vol. 7, no. 27, pp. 8350–8356, 2019. DOI: 10.1039/c9tc02402f.

[148] A. Schmitz, L. L. Schaberg, S. Sirotinskaya, M. Pantaler, D. C. Lupascu, N. Benson, and G. Bacher, "Fine Structure of the Optical Absorption Resonance in Cs2AgBiBr6 Double Perovskite Thin Films", *ACS energy letters*, vol. 5, no. 2, pp. 559–565, 2020, ISSN: 2380-8195. DOI: 10.1021/acsenergylett.9b02781.

[149] J. Su, Y.-q. Huang, H. Chen, and J. Huang, "Solution Growth and Performance Study of Cs2AgBiBr6 Single Crystal", *Crystal Research and Technology*, vol. 55, no. 3, p. 1 900 222, 2020, ISSN: 02321300. DOI: 10.1002/crat.201900222.

[150] M. Daub and H. Hillebrecht, "Synthesis, single-crystal structure and characterization of (CH3NH3)2Pb(SCN)2I2", *Angewandte Chemie (International ed. in English)*, vol. 54, no. 38, pp. 11 016–11 017, 2015. DOI: 10.1002/anie.201506449.

[151] W.-Q. Liao, Y. Zhang, C.-L. Hu, J.-G. Mao, H.-Y. Ye, P.-F. Li, S. D. Huang, and R.-G. Xiong, "A lead-halide perovskite molecular ferroelectric semiconductor", *Nature communications*, vol. 6, p. 7338, 2015. DOI: 10.1038/ncomms8338.

[152] G. Bellussi, M. Bohnet, J. Bus, K. Drauz, H. Greim, K.-P. Jackel, U. Karst, G. Kreysa, T. Laird, W. Meier, E. Ottow, M. Roper, J. Scholtz, K. Sundmacher, R. Ulber, and U. Wietelmann, *Ullmann's encyclopedia of industrial chemistry*, 7th, completely rev. ed. Weinheim: Wiley-VCH, 2011, ISBN: 9783527329434.

[153] B. Spingler, S. Schnidrig, T. Todorova, and F. Wild, "Some thoughts about the single crystal growth of small molecules", *CrystEngComm*, vol. 14, no. 3, pp. 751–757, 2012. DOI: 10.1039/C1CE05624G.

[154] S. Hull and P. Berastegui, "Crystal structures and ionic conductivities of ternary derivatives of the silver and copper monohalides—II: ordered phases within the (AgX)x–(MX)1−x and (CuX)x–(MX)1−x (M=K, Rb and Cs; X=Cl, Br and I) systems", *Journal of Solid State Chemistry*, vol. 177, no. 9, pp. 3156–3173, 2004, ISSN: 00224596. DOI: 10.1016/j.jssc.2004.05.004.

[155] W. Zhang, Z. Gong, S. Pan, Y. Zhang, D. Chen, and J. Pan, "Growth and photodetection properties of Cs2AgBiBr6 crystals with large flat (111) plane grown from the solution by adding toluene", *Journal of Crystal Growth*, vol. 552, p. 125 922, 2020, ISSN: 00220248. DOI: 10.1016/j.jcrysgro.2020.125922.

[156] W. Yuan, G. Niu, Y. Xian, H. Wu, H. Wang, H. Yin, P. Liu, W. Li, and J. Fan, "In Situ Regulating the Order–Disorder Phase Transition in Cs2AgBiBr6 Single Crystal toward the Application in an X–Ray Detector", *Advanced Functional Materials*, vol. 29, no. 20, p. 1 900 234, 2019. DOI: 10.1002/adfm.201900234.

[157] A. Maiti, S. Chatterjee, L. Peedikakkandy, and A. J. Pal, "Defects and Their Passivation in Hybrid Halide Perovskites toward Solar Cell Applications", *Solar RRL*, vol. 4, no. 12, p. 2 000 505, 2020. DOI: 10.1002/solr.202000505.

[158] P. K. Nayak, D. T. Moore, B. Wenger, S. Nayak, A. A. Haghighirad, A. Fineberg, N. K. Noel, O. G. Reid, G. Rumbles, P. Kukura, K. A. Vincent, and H. J. Snaith, "Mechanism for rapid growth of organic-inorganic halide perovskite crystals", *Nature communications*, vol. 7, p. 13 303, 2016. DOI: 10.1038/ncomms13303.

[159] Y. Deng, S. Xu, S. Chen, X. Xiao, J. Zhao, and J. Huang, "Defect compensation in formamidinium–caesium perovskites for highly efficient solar mini-modules with improved photostability", *Nature Energy*, vol. 6, no. 6, pp. 633–641, 2021. DOI: 10.1038/s41560-021-00831-8.

[160] H. Duim, S. Adjokatse, S. Kahmann, G. H. ten Brink, and M. A. Loi, "The Impact of Stoichiometry on the Photophysical Properties of Ruddlesden–Popper Perovskites", *Advanced Functional Materials*, vol. 30, no. 5, p. 1 907 505, 2020. DOI: 10.1002/adfm.201907505.

[161] V. Kumar, J. Barbé, W. L. Schmidt, K. Tsevas, B. Ozkan, C. M. Handley, C. L. Freeman, D. C. Sinclair, I. M. Reaney, W. C. Tsoi, A. Dunbar, and C. Rodenburg, "Stoichiometry-dependent local instability in MAPbI 3 perovskite materials and

devices", *Journal of Materials Chemistry A*, vol. 6, no. 46, pp. 23 578–23 586, 2018. DOI: 10.1039/C8TA08231F.

[162] A. Kojima, K. Teshima, Y. Shirai, and T. Miyasaka, "Organometal halide perovskites as visible-light sensitizers for photovoltaic cells", *Journal of the American Chemical Society*, vol. 131, no. 17, pp. 6050–6051, 2009. DOI: 10.1021/ja809598r.

[163] E. H. Jung, N. J. Jeon, E. Y. Park, C. S. Moon, T. J. Shin, T.-Y. Yang, J. H. Noh, and J. Seo, "Efficient, stable and scalable perovskite solar cells using poly(3-hexylthiophene)", *Nature*, vol. 567, no. 7749, pp. 511–515, 2019. DOI: 10.1038/s41586-019-1036-3.

[164] A. M. A. Leguy, Y. Hu, M. Campoy-Quiles, M. I. Alonso, O. J. Weber, P. Azarhoosh, M. van Schilfgaarde, M. T. Weller, T. Bein, J. Nelson, P. Docampo, and P. R. F. Barnes, "Reversible Hydration of CH3NH3PbI3 in Films, Single Crystals, and Solar Cells", *Chemistry of Materials*, vol. 27, no. 9, pp. 3397–3407, 2015. DOI: 10.1021/acs.chemmater.5b00660.

[165] M. L. Petrus, Y. Hu, D. Moia, P. Calado, A. M. A. Leguy, P. R. F. Barnes, and P. Docampo, "The Influence of Water Vapor on the Stability and Processing of Hybrid Perovskite Solar Cells Made from Non-Stoichiometric Precursor Mixtures", *ChemSusChem*, vol. 9, no. 18, pp. 2699–2707, 2016. DOI: 10.1002/cssc.201600999.

[166] M. L. Petrus, J. Schlipf, C. Li, T. P. Gujar, N. Giesbrecht, P. Müller-Buschbaum, M. Thelakkat, T. Bein, S. Hüttner, and P. Docampo, "Capturing the Sun: A Review of the Challenges and Perspectives of Perovskite Solar Cells", *Advanced Energy Materials*, vol. 7, no. 16, p. 1 700 264, 2017, ISSN: 1614-6832. DOI: 10.1002/aenm.201700264.

[167] Z. Xiao, K.-Z. Du, W. Meng, J. Wang, D. B. Mitzi, and Y. Yan, "Intrinsic Instability of Cs2In(I)M(III)X6 (M = Bi, Sb; X = Halogen) Double Perovskites: A Combined Density Functional Theory and Experimental Study", *Journal of the American Chemical Society*, vol. 139, no. 17, pp. 6054–6057, 2017. DOI: 10.1021/jacs.7b02227.

[168] G. Volonakis, A. A. Haghighirad, H. J. Snaith, and F. Giustino, "Route to Stable Lead-Free Double Perovskites with the Electronic Structure of CH3NH3PbI3: A Case for Mixed-Cation Cs/CH3NH3/CH(NH2)22InBiBr6", *The journal of physical chemistry letters*, vol. 8, no. 16, pp. 3917–3924, 2017. DOI: 10.1021/acs.jpclett.7b01584.

[169] M. R. Filip, X. Liu, A. Miglio, G. Hautier, and F. Giustino, "Phase Diagrams and Stability of Lead-Free Halide Double Perovskites Cs2BB′X6: B = Sb and Bi, B′ = Cu, Ag, and Au, and X = Cl, Br, and I", *The Journal of Physical Chemistry C*, vol. 122, no. 1, pp. 158–170, 2018. DOI: 10.1021/acs.jpcc.7b10370.

[170] X.-G. Zhao, J.-H. Yang, Y. Fu, D. Yang, Q. Xu, L. Yu, S.-H. Wei, and L. Zhang, "Design of Lead-Free Inorganic Halide Perovskites for Solar Cells via Cation-Transmutation", *Journal of the American Chemical Society*, vol. 139, no. 7, pp. 2630–2638, 2017. DOI: 10.1021/jacs.6b09645.

[171] Z. Xiao, W. Meng, J. Wang, and Y. Yan, "Thermodynamic Stability and Defect Chemistry of Bismuth-Based Lead-Free Double Perovskites", *ChemSusChem*, vol. 9, no. 18, pp. 2628–2633, 2016. DOI: 10.1002/cssc.201600771.

[172] K.-Z. Du, W. Meng, X. Wang, Y. Yan, and D. B. Mitzi, "Bandgap Engineering of Lead-Free Double Perovskite Cs2 AgBiBr6 through Trivalent Metal Alloying", *Angewandte Chemie (International ed. in English)*, vol. 56, no. 28, pp. 8158–8162, 2017. DOI: 10.1002/anie.201703970.

[173] D. Bartesaghi, A. H. Slavney, M. C. Gélvez-Rueda, B. A. Connor, F. C. Grozema, H. I. Karunadasa, and T. J. Savenije, "Charge Carrier Dynamics in Cs2AgBiBr6 Double Perovskite", *The journal of physical chemistry. C, Nanomaterials and interfaces*, vol. 122, no. 9, pp. 4809–4816, 2018, ISSN: 1932-7447. DOI: 10.1021/acs.jpcc.8b00572.

[174] M. R. Filip, S. Hillman, A. A. Haghighirad, H. J. Snaith, and F. Giustino, "Band Gaps of the Lead-Free Halide Double Perovskites Cs2BiAgCl6 and Cs2BiAgBr6 from Theory and Experiment", *The journal of physical chemistry letters*, vol. 7, no. 13, pp. 2579–2585, 2016. DOI: 10.1021/acs.jpclett.6b01041.

[175] F. Wei, Z. Deng, S. Sun, F. Zhang, D. M. Evans, G. Kieslich, S. Tominaka, M. A. Carpenter, J. Zhang, P. D. Bristowe, and A. K. Cheetham, "Synthesis and Properties of a Lead-Free Hybrid Double Perovskite: (CH3NH3)2AgBiBr6", *Chemistry of Materials*, vol. 29, no. 3, pp. 1089–1094, 2017. DOI: 10.1021/acs.chemmater.6b03944.

[176] W. Ning, F. Wang, B. Wu, J. Lu, Z. Yan, X. Liu, Y. Tao, J.-M. Liu, W. Huang, M. Fahlman, L. Hultman, T. C. Sum, and F. Gao, "Long Electron-Hole Diffusion Length in High-Quality Lead-Free Double Perovskite Films", *Advanced materials (Deerfield Beach, Fla.)*, vol. 30, no. 20, e1706246, 2018. DOI: 10.1002/adma.201706246..

[177] A. E. Maughan, A. M. Ganose, D. O. Scanlon, and J. R. Neilson, "Perspectives and Design Principles of Vacancy-Ordered Double Perovskite Halide Semiconductors", *Chemistry of Materials*, vol. 31, no. 4, pp. 1184–1195, 2019. DOI: 10.1021/acs.chemmater.8b05036.

[178] R. Quintero-Bermudez, A. Gold-Parker, A. H. Proppe, R. Munir, Z. Yang, S. O. Kelley, A. Amassian, M. F. Toney, and E. H. Sargent, "Compositional and orientational control in metal halide perovskites of reduced dimensionality", *Nature materials*, vol. 17, no. 10, pp. 900–907, 2018, ISSN: 1476-1122. DOI: 10.1038/s41563-018-0154-x.

[179] Q. Liang, J. Liu, Z. Cheng, Y. Li, L. Chen, R. Zhang, J. Zhang, and Y. Han, "Enhancing the crystallization and optimizing the orientation of perovskite films via controlling nucleation dynamics", *Journal of Materials Chemistry A*, vol. 4, no. 1, pp. 223–232, 2016. DOI: 10.1039/C5TA08015K.

[180] P. Docampo, F. C. Hanusch, N. Giesbrecht, P. Angloher, A. Ivanova, and T. Bein, "Influence of the orientation of methylammonium lead iodide perovskite crystals on solar cell performance", *APL Materials*, vol. 2, no. 8, p. 081 508, 2014. DOI: 10.1063/1.4890244.

[181] N. Cho, F. Li, B. Turedi, L. Sinatra, S. P. Sarmah, M. R. Parida, M. I. Saidaminov, B. Murali, V. M. Burlakov, A. Goriely, O. F. Mohammed, T. Wu, and O. M. Bakr, "Pure crystal orientation and anisotropic charge transport in large-area hybrid perovskite films", *Nature communications*, vol. 7, p. 13 407, 2016. DOI: 10.1038/ncomms13407.

[182] G. Niu, H. Yu, J. Li, D. Wang, and L. Wang, "Controlled orientation of perovskite films through mixed cations toward high performance perovskite solar cells", *Nano Energy*, vol. 27, pp. 87–94, 2016, ISSN: 22112855. DOI: 10.1016/j.nanoen.2016.06.053.

[183] N. Giesbrecht, J. Schlipf, L. Oesinghaus, A. Binek, T. Bein, P. Müller-Buschbaum, and P. Docampo, "Synthesis of Perfectly Oriented and Micrometer-Sized MAPbBr3 Perovskite Crystals for Thin-Film Photovoltaic Applications", *ACS energy letters*, vol. 1, no. 1, pp. 150–154, 2016, ISSN: 2380-8195. DOI: 10.1021/acsenergylett.6b00050.

[184] J. Xiu, Y. Shao, L. Chen, Y. Feng, J. Dai, X. Zhang, Y. Lin, Y. Zhu, Z. Wu, Y. Zheng, H. Pan, C. Liu, X. Shi, X. Cheng, and Z. He, "Defining the composition and electronic structure of large-scale and single-crystalline like Cs2AgBiBr6 films fabricated by capillary-assisted dip-coating method", *Materials Today Energy*,

vol. 12, pp. 186–197, 2019, ISSN: 24686069. DOI: 10.1016/j.mtener.2019.01.010.

[185] M. Pantaler, K. T. Cho, V. I. E. Queloz, I. García Benito, C. Fettkenhauer, I. Anusca, M. K. Nazeeruddin, D. C. Lupascu, and G. Grancini, "Hysteresis-Free Lead-Free Double-Perovskite Solar Cells by Interface Engineering", *ACS energy letters*, vol. 3, no. 8, pp. 1781–1786, 2018, ISSN: 2380-8195. DOI: 10.1021/acsenergylett.8b00871.

[186] M. Jiang, Y. Wu, Y. Zhou, and Z. Wang, "Observation of lower defect density brought by excess PbI2 in CH3NH3PbI3 solar cells", *AIP Advances*, vol. 9, no. 8, p. 085 301, 2019. DOI: 10.1063/1.5099280.

[187] Y. Cheng, H.-W. Li, J. Qing, Q.-D. Yang, Z. Guan, C. Liu, S. H. Cheung, S. K. So, C.-S. Lee, and S.-W. Tsang, "The detrimental effect of excess mobile ions in planar CH3 NH3PbI3 perovskite solar cells", *Journal of Materials Chemistry A*, vol. 4, no. 33, pp. 12 748–12 755, 2016. DOI: 10.1039/C6TA05053K.

[188] T. Du, C. H. Burgess, J. Kim, J. Zhang, J. R. Durrant, and M. A. McLachlan, "Formation, location and beneficial role of PbI2 in lead halide perovskite solar cells", *Sustainable Energy & Fuels*, vol. 1, no. 1, pp. 119–126, 2017. DOI: 10.1039/C6SE00029K.

[189] H. Lei, D. Hardy, and F. Gao, "Lead–Free Double Perovskite Cs2AgBiBr6 : Fundamentals, Applications, and Perspectives", *Advanced Functional Materials*, vol. 31, no. 49, p. 2 105 898, 2021. DOI: 10.1002/adfm.202105898.

[190] T. Li, X. Zhao, D. Yang, M.-H. Du, and L. Zhang, "Intrinsic Defect Properties in Halide Double Perovskites for Optoelectronic Applications", *Physical Review Applied*, vol. 10, no. 4, 2018. DOI: 10.1103/PhysRevApplied.10.041001.

[191] T. J. Savenije, A. J. Ferguson, N. Kopidakis, and G. Rumbles, "Revealing the Dynamics of Charge Carriers in Polymer:Fullerene Blends Using Photoinduced Time-Resolved Microwave Conductivity", *The Journal of Physical Chemistry C*, vol. 117, no. 46, pp. 24 085–24 103, 2013. DOI: 10.1021/jp406706u.

[192] H.-J. Feng, W. Deng, K. Yang, J. Huang, and X. C. Zeng, "Double Perovskite Cs2BBiX6 (B = Ag, Cu; X = Br, Cl)/TiO2 Heterojunction: An Efficient Pb-Free Perovskite Interface for Charge Extraction", *The Journal of Physical Chemistry C*, vol. 121, no. 8, pp. 4471–4480, 2017. DOI: 10.1021/acs.jpcc.7b00138.

[193] L. R. V. Buizza, H. C. Sansom, A. D. Wright, A. M. Ulatowski, M. B. Johnston, H. J. Snaith, and L. M. Herz, "Interplay of Structure, Charge–Carrier Localization and Dynamics in Copper–Silver–Bismuth–Halide Semiconductors", *Advanced Functional Materials*, vol. 32, no. 6, p. 2 108 392, 2022. DOI: 10.1002/adfm.202108392.

[194] T. Zuo, F. Qi, C.-Y. Yam, and L. Meng, "Lead-Free All Inorganic Halide Double Perovskite Materials for Optoelectronic Applications: Progress, Performance and Design", *Physical chemistry chemical physics : PCCP*, 2022. DOI: 10.1039/D2CP03463H.

[195] H. C. Sansom, G. Longo, A. D. Wright, L. R. V. Buizza, S. Mahesh, B. Wenger, M. Zanella, M. Abdi-Jalebi, M. J. Pitcher, M. S. Dyer, T. D. Manning, R. H. Friend, L. M. Herz, H. J. Snaith, J. B. Claridge, and M. J. Rosseinsky, "Highly Absorbing Lead-Free Semiconductor Cu2AgBiI6 for Photovoltaic Applications from the Quaternary CuI-AgI-BiI3 Phase Space", *Journal of the American Chemical Society*, 2021. DOI: 10.1021/jacs.1c00495.

[196] M. T. Sirtl, R. Hooijer, M. Armer, F. G. Ebadi, M. Mohammadi, C. Maheu, A. Weis, B. T. van Gorkom, S. Häringer, R. A. J. Janssen, T. Mayer, V. Dyakonov, W. Tress, and T. Bein, "2D/3D Hybrid Cs2AgBiBr6 Double Perovskite Solar Cells: Improved Energy Level Alignment for Higher Contact–Selectivity and Large Open Circuit Voltage", *Advanced Energy Materials*, p. 2 103 215, 2022, ISSN: 1614-6832. DOI: 10.1002/aenm.202103215.

[197] A. H. Slavney, R. W. Smaha, I. C. Smith, A. Jaffe, D. Umeyama, and H. I. Karunadasa, "Chemical Approaches to Addressing the Instability and Toxicity of Lead-Halide Perovskite Absorbers", *Inorganic chemistry*, vol. 56, no. 1, pp. 46–55, 2017. DOI: 10.1021/acs.inorgchem.6b01336.

[198] S. Li, Z. Shi, F. Zhang, L. Wang, Z. Ma, Di Wu, D. Yang, X. Chen, Y. Tian, Y. Zhang, C. Shan, and X. Li, "Ultrastable Lead-Free Double Perovskite Warm-White Light-Emitting Devices with a Lifetime above 1000 Hours", *ACS applied materials & interfaces*, vol. 12, no. 41, pp. 46 330–46 339, 2020. DOI: 10.1021/acsami.0c14557.

[199] M. T. Sirtl, F. Ebadi, B. T. Gorkom, P. Ganswindt, R. A. J. Janssen, T. Bein, and W. Tress, "The Bottlenecks of Cs2AgBiBr6 Solar Cells: How Contacts and Slow Transients Limit the Performance", *Advanced Optical Materials*, vol. 9, no. 14, p. 2 100 202, 2021, ISSN: 2195-1071. DOI: 10.1002/adom.202100202.

[200] A. A. Yaroshevsky, "Abundances of chemical elements in the Earth's crust", *Geochemistry International*, vol. 44, no. 1, pp. 48–55, 2006. DOI: 10.1134/S001670290601006X.

[201] W. Li, N. U. Rahman, Y. Xian, H. Yin, Y. Bao, Y. Long, S. Yuan, Y. Zhang, Y. Yuan, and J. Fan, "Regulation of the order-disorder phase transition in a Cs2NaFeCl6 double perovskite towards reversible thermochromic application", *Journal of Semiconductors*, vol. 41, 2021. DOI: 10.1088/1674-4926/41/5/052201.

[202] P. Han, C. Luo, W. Zhou, J. Hou, C. Li, D. Zheng, and K. Han, "Band-Gap Engineering of Lead-Free Iron-Based Halide Double-Perovskite Single Crystals and Nanocrystals by an Alloying or Doping Strategy", *The Journal of Physical Chemistry C*, 2021. DOI: 10.1021/acs.jpcc.1c02636.

[203] J. Höcker, M. Ozcan, S. Hammer, M. Fischer, B. Bichler, M. Armer, P. Rieder, V. Drach, J. Pflaum, B. Nickel, and V. Dyakonov, "Seed crystal free growth of high-quality double cation – double halide perovskite single crystals for optoelectronic applications", *Journal of Materials Chemistry C*, vol. 8, no. 24, pp. 8275–8283, 2020. DOI: 10.1039/D0TC01617A.

[204] P. Giannozzi, S. Baroni, N. Bonini, M. Calandra, R. Car, C. Cavazzoni, D. Ceresoli, G. L. Chiarotti, M. Cococcioni, I. Dabo, A. Dal Corso, S. de Gironcoli, S. Fabris, G. Fratesi, R. Gebauer, U. Gerstmann, C. Gougoussis, A. Kokalj, M. Lazzeri, L. Martin-Samos, N. Marzari, F. Mauri, R. Mazzarello, S. Paolini, A. Pasquarello, L. Paulatto, C. Sbraccia, S. Scandolo, G. Sclauzero, A. P. Seitsonen, A. Smogunov, P. Umari, and R. M. Wentzcovitch, "QUANTUM ESPRESSO: a modular and open-source software project for quantum simulations of materials", *Journal of physics. Condensed matter : an Institute of Physics journal*, vol. 21, no. 39, p. 395 502, 2009. DOI: 10.1088/0953-8984/21/39/395502.

[205] P. Giannozzi, O. Andreussi, T. Brumme, O. Bunau, M. Buongiorno Nardelli, M. Calandra, R. Car, C. Cavazzoni, D. Ceresoli, M. Cococcioni, N. Colonna, I. Carnimeo, A. Dal Corso, S. de Gironcoli, P. Delugas, R. A. DiStasio, A. Ferretti, A. Floris, G. Fratesi, G. Fugallo, R. Gebauer, U. Gerstmann, F. Giustino, T. Gorni, J. Jia, M. Kawamura, H.-Y. Ko, A. Kokalj, E. Küçükbenli, M. Lazzeri, M. Marsili, N. Marzari, F. Mauri, N. L. Nguyen, H.-V. Nguyen, A. Otero-de-la Roza, L. Paulatto, S. Poncé, D. Rocca, R. Sabatini, B. Santra, M. Schlipf, A. P. Seitsonen, A. Smogunov, I. Timrov, T. Thonhauser, P. Umari, N. Vast, X. Wu, and S. Baroni, "Advanced capabilities for materials modelling with Quantum ESPRESSO", *Journal of physics. Condensed matter : an Institute of Physics journal*, vol. 29, no. 46, p. 465 901, 2017. DOI: 10.1088/1361-648X/aa8f79.

[206] K. F. Garrity, J. W. Bennett, K. M. Rabe, and D. Vanderbilt, "Pseudopotentials for high-throughput DFT calculations", *Computational Materials Science*, vol. 81, pp. 446–452, 2014, ISSN: 09270256. DOI: 10.1016/j.commatsci.2013.08.053.

[207] M. Cococcioni and S. de Gironcoli, "Linear response approach to the calculation of the effective interaction parameters in the LDA+U method", *Physical Review B*, vol. 71, no. 3, 2005. DOI: 10.1103/PhysRevB.71.035105.

[208] J. Hubbard, "The magnetism of iron", *Physical Review B*, vol. 19, no. 5, pp. 2626–2636, 1979. DOI: 10.1103/PhysRevB.19.2626.

[209] J. Hubbard, "Magnetism of iron. II", *Physical Review B*, vol. 20, no. 11, pp. 4584–4595, 1979. DOI: 10.1103/PhysRevB.20.4584.

[210] M. Armer, P. Dörflinger, A. Weis, C. Büchner, A. Gottscholl, J. Höcker, K. Frank, L. Nusser, M. T. Sirtl, B. Nickel, T. Bein, and V. Dyakonov, "Low Temperature Optical Properties of Novel Lead–Free Cs 2 NaFeCl 6 Perovskite Single Crystals", *Advanced Photonics Research*, vol. 4, no. 5, 2023, ISSN: 2699-9293. DOI: 10.1002/adpr.202300017.

[211] A. C. Thompson, *X-Ray Data Booklet: Center for X-Ray Optics and Advanced Light Source*. 2001.

[212] F. Wei, F. Brivio, Y. Wu, S. Sun, P. D. Bristowe, and A. K. Cheetham, "Synthesis, crystal structure, magnetic and electronic properties of the caesium-based transition metal halide Cs3Fe2Br9", *Journal of Materials Chemistry C*, vol. 6, no. 14, pp. 3573–3577, 2018. DOI: 10.1039/C7TC04798C.

[213] Y. Puttisong, F. Moro, S. L. Chen, P. Höjer, W. Ning, F. Gao, I. A. Buyanova, and W. M. Chen, "Effect of Crystal Symmetry on the Spin States of Fe3+ and Vibration Modes in Lead-free Double-Perovskite Cs2AgBi(Fe)Br6", *The journal of physical chemistry letters*, vol. 11, no. 12, pp. 4873–4878, 2020. DOI: 10.1021/acs.jpclett.0c01543.

[214] F. Ji, J. Klarbring, F. Wang, W. Ning, L. Wang, C. Yin, J. S. M. Figueroa, C. K. Christensen, M. Etter, T. Ederth, L. Sun, S. Simak, I. Abrikosov, and F. Gao, "Lead-Free Halide Double Perovskite Cs2AgBiBr6 with Decreased Bandgap", *Angewandte Chemie (International ed. in English)*, 2020. DOI: 10.1002/anie.202005568.

[215] M. M. Saad H.-E. and A. Elhag, "DFT study on the crystal, electronic and magnetic structures of tantalum based double perovskite oxides Ba2MTaO6 (M = Cr, Mn, Fe) via GGA and GGA + U", *Results in Physics*, vol. 9, pp. 793–805, 2018, ISSN: 22113797. DOI: 10.1016/j.rinp.2018.03.055.

[216] A. D. Wright, C. Verdi, R. L. Milot, G. E. Eperon, M. A. Pérez-Osorio, H. J. Snaith, F. Giustino, M. B. Johnston, and L. M. Herz, "Electron-phonon coupling in hybrid lead halide perovskites", *Nature communications*, vol. 7, 2016. DOI: 10.1038/ncomms11755.

[217] C. L. Davies, M. R. Filip, J. B. Patel, T. W. Crothers, C. Verdi, A. D. Wright, R. L. Milot, F. Giustino, M. B. Johnston, and L. M. Herz, "Bimolecular recombination in methylammonium lead triiodide perovskite is an inverse absorption process", *Nature communications*, vol. 9, no. 1, p. 293, 2018. DOI: 10.1038/s41467-017-02670-2.

[218] R. L. Milot, G. E. Eperon, H. J. Snaith, M. B. Johnston, and L. M. Herz, "Temperature–Dependent Charge–Carrier Dynamics in CH3NH3PbI3 Perovskite Thin Films", *Advanced Functional Materials*, vol. 25, no. 39, pp. 6218–6227, 2015. DOI: 10.1002/adfm.201502340.

[219] R. J. Elliot, "Intensity of Optical Absorption by Excitons", *Physical Review*, vol. 108, no. 6, pp. 1384–1389, 1957.

[220] Y. P. Varshni, "Temperature dependence of the energy gap in semiconductors", *Physica*, vol. 34, no. 1, pp. 149–154, 1967, ISSN: 00318914. DOI: 10.1016/0031-8914(67)90062-6.

[221] F. Ruf, M. F. Aygüler, N. Giesbrecht, B. Rendenbach, A. Magin, P. Docampo, H. Kalt, and M. Hetterich, "Temperature-dependent studies of exciton binding energy and phase-transition suppression in (Cs,FA,MA)Pb(I,Br)3 perovskites", *APL Materials*, vol. 7, no. 3, p. 031 113, 2019. DOI: 10.1063/1.5083792.

[222] B. J. Bohn, T. Simon, M. Gramlich, A. F. Richter, L. Polavarapu, A. S. Urban, and J. Feldmann, "Dephasing and Quantum Beating of Excitons in Methylammonium Lead Iodide Perovskite Nanoplatelets", *ACS Photonics*, vol. 5, no. 2, pp. 648–654, 2018, ISSN: 2330-4022. DOI: 10.1021/acsphotonics.7b01292.

[223] J. A. Steele, P. Puech, M. Keshavarz, R. Yang, S. Banerjee, E. Debroye, C. W. Kim, H. Yuan, N. H. Heo, J. Vanacken, A. Walsh, J. Hofkens, and M. B. J. Roeffaers, "Giant Electron-Phonon Coupling and Deep Conduction Band Resonance in Metal Halide Double Perovskite", *ACS nano*, vol. 12, no. 8, pp. 8081–8090, 2018. DOI: 10.1021/acsnano.8b02936.

[224] J. Leveillee, G. Volonakis, and F. Giustino, "Phonon-Limited Mobility and Electron-Phonon Coupling in Lead-Free Halide Double Perovskites", *The journal of physical chemistry letters*, vol. 12, no. 18, pp. 4474–4482, 2021. DOI: 10.1021/acs.jpclett.1c00841.

[225] J. Yang, Q. Bao, L. Shen, and L. Ding, "Potential applications for perovskite solar cells in space", *Nano Energy*, vol. 76, p. 105 019, 2020, ISSN: 22112855. DOI: 10.1016/j.nanoen.2020.105019.

[226] P. Wu, S. Wang, X. Li, and F. Zhang, "Beyond efficiency fever: Preventing lead leakage for perovskite solar cells", *Matter*, vol. 5, no. 4, pp. 1137–1161, 2022, ISSN: 25902385. DOI: 10.1016/j.matt.2022.02.012.

[227] V. K. Ravi, B. Mondal, V. V. Nawale, and A. Nag, "Don't Let the Lead Out: New Material Chemistry Approaches for Sustainable Lead Halide Perovskite Solar Cells", *ACS omega*, vol. 5, no. 46, pp. 29 631–29 641, 2020. DOI: 10.1021/acsomega.0c04599.

[228] X. Xiao, M. Wang, S. Chen, Y. Zhang, H. Gu, Y. Deng, G. Yang, C. Fei, B. Chen, Y. Lin, M. D. Dickey, and J. Huang, "Lead-adsorbing ionogel-based encapsulation for impact-resistant, stable, and lead-safe perovskite modules", *Science advances*, vol. 7, no. 44, eabi8249, 2021. DOI: 10.1126/sciadv.abi8249.

[229] S. Paschen and A. Prokofiev, Eds., *Crystal Growth and Stoichiometry of Strongly Correlated Intermetallic Cerium Compounds*. IntechOpen, 2012, ISBN: 978-953-307-610-2. DOI: 10.5772/1348.

[230] C. N. Savory, A. Walsh, and D. O. Scanlon, "Can Pb-Free Halide Double Perovskites Support High-Efficiency Solar Cells?", *ACS energy letters*, vol. 1, no. 5, pp. 949–955, 2016, ISSN: 2380-8195. DOI: 10.1021/acsenergylett.6b00471.

List of Publications

1. M. T. Sirtl, **M. Armer**, L. K. Reb, R. Hooijer, P. Dörflinger, M. A. Scheel, K. Tvingstedt, P. Rieder, N. Glück, P. Pandit, S. V. Roth, P. Müller-Buschbaum, V. Dyakonov, T. Bein. Optoelectronic Properties of $Cs_2AgBiBr_6$ Thin Films: The Influence of Precursor Stoichiometry. *ACS Appl. Energy Mater.*, 3, 12, 11597-11609, 2020, DOI: https://doi.org/10.1021/acsaem.0c01308

2. J. Höcker, M. Ozcan, S. Hammer, M. Fischer, B. Bichler, **M. Armer**, P. Rieder, V. Drach, J. Pflaum, B. Nickel, V. Dyakonov. Seed crystal free growth of high-quality double cation - double halide perovskite single crystals for optoelectronic applications. *Journal of Materials Chemistry C*, 8, 8275-8283, 2020, DOI: https://doi.org/10.1039/D0TC01617A

3. **M. Armer**, J. Höcker, C. Büchner, S. Häfele, P. Dörflinger, M. T. Sirtl, K. Tvingstedt, T. Bein, V. Dyakonov. Influence of crystallisation on the structural and optical properties of lead-free $Cs_2AgBiBr_6$ perovskite crystals. *CrystEngComm*, 23, 6848-6854, 2021, DOI: https://doi.org/10.1039/D1CE00844G

4. J. Höcker, F. Brust, **M. Armer**, V. Dyakonov. A temperature-reduced method for the rapid growth of hybrid perovskite single crystals with primary alcohols. *CrystEngComm*, 23, 2202-2207, 2021, DOI: https://doi.org/10.1039/D0CE01759K

5. M. T. Sirtl, R. Hooijer, **M. Armer**, F. G. Ebadi, M. Mohammadi, C. Maheu, A. Weis, B. T. van Gorkum, S. Häringer, R. A. Janssen, T. Mayer, V. Dyakonov, W. Tress, T. Bein. 2D/3D Hybrid $Cs_2AgBiBr_6$ Double Perovskite Solar Cells: Improved Energy Level Alignment for Higher Contact-Selectivity and Large Open Circuit Voltage. *Advanced Energy Materials*, 12, 7, 2103215-2103215, 2022, DOI: https://doi.org/10.1002/aenm.202103215

6. Y. Ding, B. Ding, H. Kanda, O. J. Usiobo, T. Gallet, Z. Yang, Y. Liu, H. Huang, J. Sheng, C. Liu, Y. Yang, V. I. E. Queloz, X. Zhang, J.-N. Audinot, A. Redinger, W. Dang, E. Mosconic, W. Luo, F. De Angelis, M.i Wang, P. Dörflinger, **M. Armer**, V. Schmid, R. Wang, K. G. Brooks, J. Wu, V. Dyakonov, G. Yang, S. Dai, P. J. Dyson, M. K. Nazeeruddin. Single-crystalline TiO_2 nanoparticles for stable efficient perovskite modules. *Nature Nanotechnology*, 17, 598-605, 2022, DOI: https://doi.org/10.1038/s41565-022-01108-1

7. A. Weis, P. Ganswindt, W. Kaiser, H. Illner, C. Maheu, N. Glück, P. Dörflinger, **M. Armer**, V. Dyakonov, J. P. Hofmann, E. Mosconi, F. de Angelis, T. Bein. Heterovalent Tin Alloying in Layered $MA_3Sb_2I_9$ Thin Films: Assessing the origin of enhanced absorption and self-stabilizing charge states. *The Journal of Physical Chemistry C*, 2022, DOI: https://doi.org/10.1021/acs.jpcc.2c06106

8. **M. Armer**, P. Dörflinger, A. Weis, C. Büchner, A. Gottscholl, J. Höcker, K. Frank, L. Nusser, M. T. Sirtl, B. Nickel, T. Bein, V. Dyakonov. Low temperature optical properties of novel lead-free $Cs_2NaFeCl_6$ perovskite single crystals. *Advanced Photonics Reasearch*, 4, 2300017, 2023, DOI: https://doi.org/10.1002/adpr.202300017

9. F. Wolf, M. T. Sirtl, S. Klenk, M. H. H. Wurzenberger, **M. Armer**, P. Dörflinger, P. Ganswindt, R. Guntermann, V. Dyakonov, T. Bein. Behind the scenes: insights into the structural properties of amide-based hole-transporting materials for lead-free perovskite solar cells. *CrystEngComm*, 25, 3142-3149, 2023, DOI: https://doi.org/10.1039/D2CE01512A

Acknowledgements

Finally, I want to thank everyone who supported me during the past year.

- First, I want to thank Prof. Vladimir Dyakonov for the warm welcome when I first joined the group during my Bachelor thesis. Further, I also want to thank Prof. Dyakonov for the continuing support throughout my Master and PhD. You gave me the chance to take on the challenge to work on lead-free double perovskites, which gave me the opportunity to grow, make new experiences and to learn to never give up.

- Dr. Luidmila Kudriashova and Dr. Kristofer Tvingstedt for all the support, tips, fruitful discussions about PL and the chance to learn from you.

- Dr. Sebastian Hammer and Prof. Jens Pflaum for their expertise in XRD and for the time you took to teach me how to measure single crystal XRD.

- Dr. Julian Höcker receives a special thanks for all the long hours of discussions in the lab. Thank you so much for the support when things did not go as planned and for all the talks we had while figuring out crystal growth.

- Stephan Braxmeier for all the SEM and EDX measurements as well as Philip Potsch and Andreas Stephan for the programmable hot plate. Thank you for all the time you invested in measuring SEM and fixing the bugs of the hotplate. Without you, crystal growth would not have been possible.

- My bachelorstudents Sophie Häfele and Carsten Büchner, who did excellent work in supporting crystal growth as well as the characterization of the materials.

- André Thiem-Riebe, Detlev Kranl, Valentin Baianov and Diep Phan who always help and fix the issues in the lab and help with the jungle of buerocracy.

- I also want to thank my project partners at LMU Munich. Max, Andi, Rik und Flo - it was so great to get to know you all! Having the opportunity to work with you was really great!

- Another very special thanks goes to Patrick Dörflinger. Thank you for the time together. Without you the PhD would have been significantly less fun! Also thank you for great chats, new memes glued to my computer screen after every vacation, always keeping chocolate ready and our occasional drinks.

- Philipp Rieder, Patrick Dörflinger, Jeannine Grüne and all past inhabitants of office E08. This office was not only a workplace but you guys also became friends and family for me!
- All people at EP VI! It was a great time working with you!
- Dr. Megha Joshi for being the greatest roommate I could ever have wished for when I came to Austin. Even though we haven't seen each other for the past 5 years, all the messages, pictures and discussions about upcoming papers, issues and reminders that PhD is a journey and that we can both make it, really helped to keep the motivation up when things didn't go as planned.
- Oscar Ebert, Henry, Siegfried, Gudrun and Henry jr. for making writing significantly more enjoyable. You have done the absolut greatest job in supporting me throughout the past years.
- Als letztes möchte ich mich noch bei Max und meinen Eltern bedanken. Ihr habt mich immer bedingungslos unterstützt und an mich geglaubt. Ohne euch wäre ich nicht da, wo ich heute bin! Danke Max, dass du dir jeden Konferenzvortrag mindestens 30 Mal angehört hast und selbst dann noch Kritik geäußert hast, mit dem Risiko dass es auch noch einen 31. Versuch geben wird.